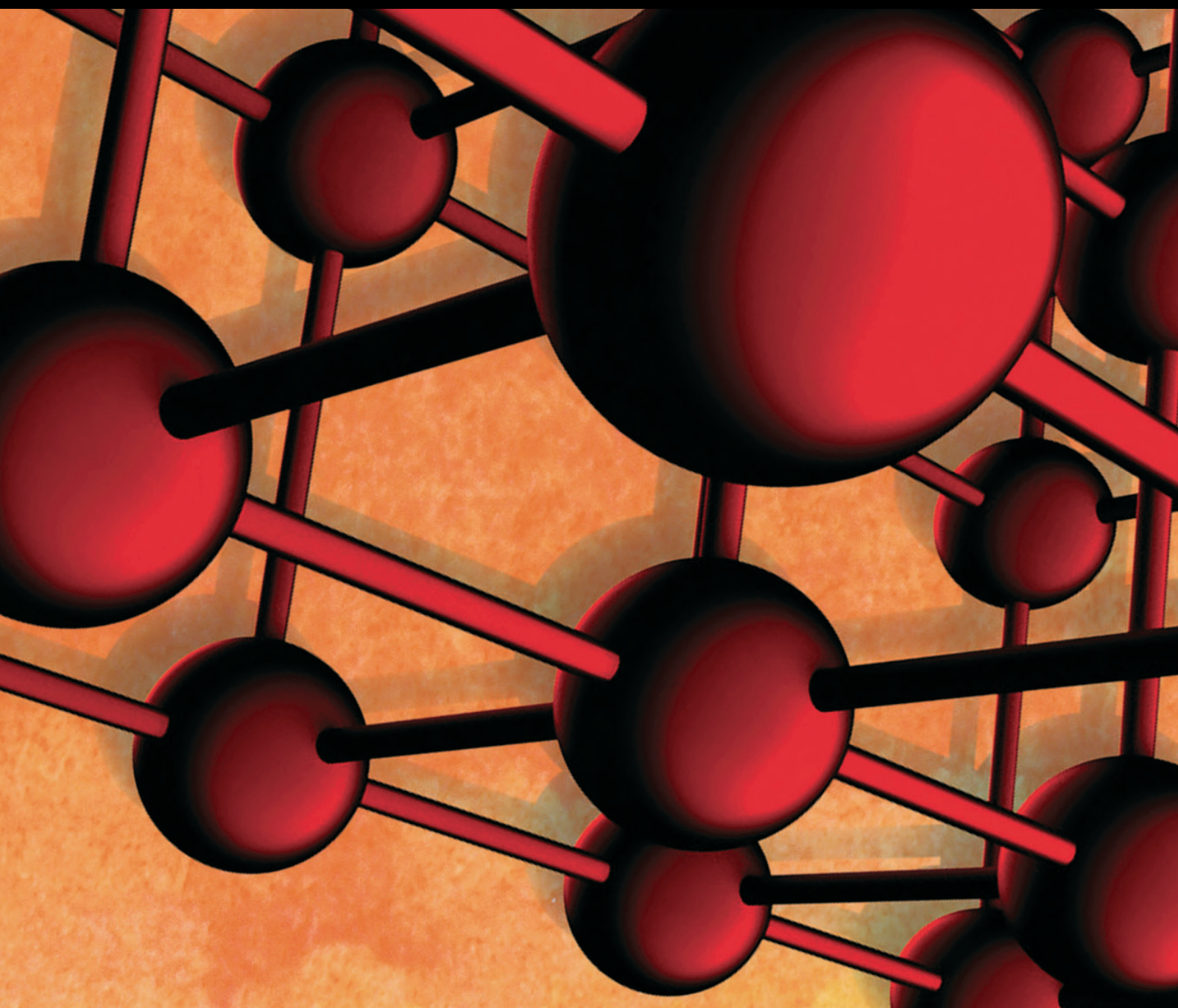


Advances in Materials Science and Engineering

# Corrosion of Nonferrous Metals and Their Alloys

Special Issue Editor in Chief: Alicia E. Ares

Guest Editors: Raúl Rebak, María V. Biezma, and Claudia M. Méndez





---

# **Corrosion of Nonferrous Metals and Their Alloys**

Advances in Materials Science and Engineering

---

## **Corrosion of Nonferrous Metals and Their Alloys**

Special Issue Editor in Chief: Alicia E. Ares  
Guest Editors: Raúl Rebak, María V. Biezma,  
and Claudia M. Méndez



---

Copyright © 2018 Hindawi. All rights reserved.

This is a special issue published in “Advances in Materials Science and Engineering.” All articles are open access articles distributed under the Creative Commons Attribution License, which permits unrestricted use, distribution, and reproduction in any medium, provided the original work is properly cited.

## Editorial Board

- Antonio Abate, Germany  
Michael Aizenshtein, Israel  
Jarir Aktaa, Germany  
Amelia Almeida, Portugal  
K. G. Anthymidis, Greece  
Santiago Aparicio, Spain  
Alicia E. Ares, Argentina  
Farhad Aslani, Australia  
Renal Backov, France  
Markus Bambach, Germany  
Amit Bandyopadhyay, USA  
Massimiliano Barletta, Italy  
Mikhael Bechelany, France  
Avi Bendavid, Australia  
Brahim Benmokrane, Canada  
Jamal Berakdar, Germany  
Jean-Michel Bergheau, France  
G. Bernard-Granger, France  
Giovanni Berselli, Italy  
Patrice Berthod, France  
Michele Bianchi, Italy  
Hugo C. Biscaia, Portugal  
Antonio Boccaccio, Italy  
Federica Bondioli, Italy  
Susmita Bose, USA  
Heinz-Günter Brokmeier, Germany  
Steve Bull, UK  
Gianlorenzo Bussetti, Italy  
Jose M. Cabrera, Spain  
Antonio Caggiano, Germany  
Veronica Calado, Brazil  
Marco Cannas, Italy  
Paolo Andrea Carraro, Italy  
Michelina Catauro, Italy  
Jose Cesar de Sa, Portugal  
Peter Chang, Canada  
Daolun Chen, Canada  
Gianluca Cicala, Italy  
Francesco Colangelo, Italy  
Marco Consales, Italy  
José A. Correia, Portugal  
María Criado, UK  
Gabriel Cuello, France  
Lucas da Silva, Portugal
- Narendra B. Dahotre, USA  
João P. Davim, Portugal  
Angela De Bonis, Italy  
Abílio De Jesus, Portugal  
Luca De Stefano, Italy  
Francesco Delogu, Italy  
Luigi Di Benedetto, Italy  
Aldo Di Carlo, Italy  
Maria Laura Di Lorenzo, Italy  
Marisa Di Sabatino, Norway  
Luigi Di Sarno, Italy  
Ana María Díez-Pascual, Spain  
Guru P. Dinda, USA  
Nadka Tzankova Dintcheva, Italy  
Mingdong Dong, Denmark  
Frederic Dumur, France  
Stanislaw Dymek, Poland  
Kaveh Edalati, Japan  
Philip Eisenlohr, USA  
Claude Estournès, France  
Luís Evangelista, Norway  
Michele Fedel, Italy  
F. J. Fernández Fernández, Spain  
Isabel J. Ferrer, Spain  
Paolo Ferro, Italy  
Dora Foti, Italy  
Massimo Fresta, Italy  
Pasquale Gallo, Japan  
Germà Garcia-Belmonte, Spain  
Santiago Garcia-Granda, Spain  
Carlos Garcia-Mateo, Spain  
Georgios I. Giannopoulos, Greece  
Ivan Giorgio, Italy  
Antonio Gloria, Italy  
Vincenzo Guarino, Italy  
Daniel Guay, Canada  
Gianluca Gubbiotti, Italy  
Jenő Gubicza, Hungary  
Xuchun Gui, China  
Benoit Guiffard, France  
Ivan Gutierrez-Urrutia, Japan  
Hiroki Habazaki, Japan  
Simo-Pekka Hannula, Finland  
David Holec, Austria
- Satoshi Horikoshi, Japan  
David Houivet, France  
Rui Huang, USA  
Yi Huang, UK  
Michele Iafisco, Italy  
Saliha Ilican, Turkey  
Md Mainul Islam, Australia  
Ilia Ivanov, USA  
Alfredo Juan, Argentina  
kenji Kaneko, Japan  
Katsuyuki Kida, Japan  
Akihiko Kimura, Japan  
Soshu Kirihara, Japan  
Paweł Kłosowski, Poland  
Jan Koci, Czech Republic  
Fantao Kong, China  
Ling B. Kong, Singapore  
Pramod Koshy, Australia  
Hongchao Kou, China  
Alexander Kromka, Czech Republic  
Andrea Lamberti, Italy  
Luciano Lamberti, Italy  
Fulvio Lavecchia, Italy  
Marino Lavorgna, Italy  
Laurent Lebrun, France  
Joon-Hyung Lee, Republic of Korea  
Pavel Lejcek, Czech Republic  
Cristina Leonelli, Italy  
Ying Li, USA  
Yuanshi Li, Canada  
Guang-xing Liang, China  
Barbara Liguori, Italy  
Jun Liu, China  
Meilin Liu, Georgia  
Shaomin Liu, Australia  
Yunqi Liu, China  
Zhiping Luo, USA  
Fernando Lusquinos, Spain  
Peter Majewski, Australia  
Georgios Maliaris, Greece  
Muhamamd A. Malik, UK  
Dimitrios E. Manolakos, Greece  
Enzo Martinelli, Italy  
Alessandro Martucci, Italy

Yoshitake Masuda, Japan  
Bobby Kannan Mathan, Australia  
Roshan Mayadunne, Australia  
Shazim Ali Memon, Kazakhstan  
Philippe Miele, France  
A. E. Miroshnichenko, Australia  
Hossein Moayedi, Iran  
Jose M. Monzo, Spain  
Michele Muccini, Italy  
Alfonso Muñoz, Spain  
Rufino M. Navarro, Spain  
Miguel Navarro-Cia, UK  
Ali Nazari, Australia  
Luigi Nicolais, Italy  
Peter Niemz, Switzerland  
Hiroshi Noguchi, Japan  
Chérif Nouar, France  
Olanrewaju Ojo, Canada  
Dariusz Oleszak, Poland  
Laurent Orgéas, France  
Togay Ozbakkaloglu, Australia  
Nezih Pala, USA  
Marián Palcut, Slovakia  
Davide Palumbo, Italy  
Gianfranco Palumbo, Italy  
Anna Maria Paradowska, Australia  
Zbyšek Pavlík, Czech Republic  
Matthew Peel, UK  
Gianluca Percoco, Italy  
Claudio Pettinari, Italy  
Giorgio Pia, Italy  
Daniela Pilone, Italy  
Teresa M. Piqué, Argentina  
Candido Fabrizio Pirri, Italy  
Alain Portavoce, France

Simon C. Potter, Canada  
Ulrich Prael, Germany  
Viviana F. Rahhal, Argentina  
Carlos R. Rambo, Brazil  
Shahed Rasekh, Portugal  
Manijeh Razeghi, USA  
Paulo Reis, Portugal  
Yuri Ribakov, Israel  
Aniello Riccio, Italy  
Anna Richelli, Italy  
Antonio Riveiro, Spain  
Marco Rossi, Italy  
Sylvie Rossignol, France  
Pascal Roussel, France  
Fernando Rubio-Marcos, Spain  
Francesco Ruffino, Italy  
Mark H. Rummeli, China  
Pietro Russo, Italy  
Antti Salminen, Finland  
F.H. Samuel, Canada  
MariaGabriella Santonicola, Italy  
Hélder A. Santos, Finland  
Carlo Santulli, Italy  
Fabrizio Sarasini, Italy  
Michael J. Schütze, Germany  
Raffaele Sepe, Italy  
Kenichi Shimizu, USA  
Fridon Shubitidze, USA  
Mercedes Solla, Spain  
Donato Sorgente, Italy  
Charles C. Sorrell, Australia  
Andres Sotelo, Spain  
Costas M. Soukoulis, USA  
Damien Soulat, France  
Adolfo Speghini, Italy

Antonino Squillace, Italy  
Manfred Stamm, Germany  
Koichi Sugimoto, Japan  
Baozhong Sun, China  
Sam-Shajing Sun, USA  
Youhong Tang, Australia  
Kohji Tashiro, Japan  
Miguel Angel Torres, Spain  
Laszlo Toth, France  
Achim Trampert, Germany  
Luca Valentini, Italy  
Ashkan Vaziri, USA  
Lijing Wang, Australia  
Rui Wang, China  
Zhongchang Wang, Portugal  
Lu Wei, China  
Jörg M. K. Wiezorek, USA  
Guoqiang Xie, Japan  
Dongmin Yang, UK  
Zhonghua Yao, China  
Hemmige S. Yathirajan, India  
Yee-wen Yen, Taiwan  
Wenbin Yi, China  
Ling Yin, Australia  
Hiroshi Yoshihara, Japan  
Belal F. Yousif, Australia  
Michele Zappalorto, Italy  
Jinghuai Zhang, China  
Li Zhang, China  
Mikhail Zheludkevich, Germany  
Wei Zhou, China  
You Zhou, Japan  
Hongtao Zhu, Australia

### **Corrosion of Nonferrous Metals and Their Alloys**

Alicia E. Ares , Raúl B. Rebak, María V. Biezma , and Claudia M. Méndez   
Editorial (2 pages), Article ID 8929512, Volume 2018 (2018)

### **Effect of Molybdenum on the Corrosion Behavior of High-Entropy Alloys CoCrFeNi<sub>2</sub> and CoCrFeNi<sub>2</sub>Mo<sub>0.25</sub> under Sodium Chloride Aqueous Conditions**

Alvaro A. Rodriguez, Joseph H. Tylczak , Michael C. Gao, Paul D. Jablonski, Martin Detrois, Margaret Ziomek-Moroz, and Jeffrey A. Hawk  
Research Article (11 pages), Article ID 3016304, Volume 2018 (2018)

### **Synthesis of Copper Oxide Aided by Selective Corrosion in Cu Foils**

Roberto Baca Arroyo   
Research Article (7 pages), Article ID 4231571, Volume 2018 (2018)

### **Effects of Alloying Elements (Cr, Mn) on Corrosion Properties of the High-Strength Steel in 3.5% NaCl Solution**

Bomi Kim , Soojin Kim , and Heesan Kim   
Research Article (13 pages), Article ID 7638274, Volume 2018 (2018)

### **Transition of Dislocation Structures in Severe Plastic Deformation and Its Effect on Dissolution in Dislocation Etchant**

Muhammad Rifai , Ebad Bagherpour , Genki Yamamoto, Motohiro Yuasa, and Hiroyuki Miyamoto   
Research Article (6 pages), Article ID 4254156, Volume 2018 (2018)

### **Effect of Partial Cladding Pattern of Aluminum 7075 T651 on Corrosion and Mechanical Properties**

E. Rendell, A. Hsiao, and J. Shirokoff  
Research Article (7 pages), Article ID 5282659, Volume 2017 (2018)

## Editorial

# Corrosion of Nonferrous Metals and Their Alloys

**Alicia E. Ares** <sup>1</sup>, **Raúl B. Rebak**,<sup>2</sup> **María V. Biezma** <sup>3</sup>, and **Claudia M. Méndez** <sup>4</sup>

<sup>1</sup>*Instituto de Materiales de Misiones (IMAM), Consejo Nacional de Investigaciones Científicas y Técnicas (CONICET), Universidad Nacional de Misiones (UNaM), Posadas, Misiones, Argentina*

<sup>2</sup>*GE Global Research, Schenectady, NY, USA*

<sup>3</sup>*Universidad de Cantabria, Santander, Spain*

<sup>4</sup>*Universidad Nacional de Misiones, Posadas, Misiones, Argentina*

Correspondence should be addressed to Alicia E. Ares; [aares@fceqyn.unam.edu.ar](mailto:aares@fceqyn.unam.edu.ar)

Received 13 March 2018; Accepted 14 March 2018; Published 31 May 2018

Copyright © 2018 Alicia E. Ares et al. This is an open access article distributed under the Creative Commons Attribution License, which permits unrestricted use, distribution, and reproduction in any medium, provided the original work is properly cited.

Corrosion is the result of the interaction of a material (metal) with its environment.

The corrosion process depends on the properties of both metal (and alloy) and surrounding environment. Usually, the more important factors causing corrosion are concentration of aggressive species (e.g., chloride), acidity (pH), fluid velocity, temperature, and potential (oxidizing power).

Steel and other ferrous alloys are consumed in exceedingly large quantities because they have such a wide range of mechanical properties, may be fabricated with relative ease, and are economical to produce. However, steels have some distinct limitations, chiefly a relatively high density, a comparatively low electrical conductivity, and an inherent susceptibility to corrosion in some common environments.

Thus, for many applications, it is advantageous or even necessary to use other alloys that have more suitable property combinations. Alloy systems are classified either according to the base metal or according to some specific characteristic that a group of alloys shares. Authors were invited to submit original research articles and reviews for this special issue that included all aspects of the corrosion process of the following metal and alloy systems: aluminum, copper, magnesium, and titanium alloys; the refractory metals; the superalloys; the noble metals; and miscellaneous alloys, including those that have nickel, lead, tin, zirconium, and zinc as base metals.

The papers published in this special issue are as follows:

(i) “Synthesis of Copper Oxide Aided by Selective Corrosion in Cu Foils,” by Roberto Baca Arroyo.

The authors present the synthesis of Cu oxide films aided by selective corrosion of Cu foils with a subsequent heating process in air atmosphere at low temperatures.

- (ii) “Effects of Alloying Elements (Cr, Mn) on Corrosion Properties of the High-Strength Steel in 3.5% NaCl Solution,” by BomiKim, Soojin Kim, and Heesan Kim. The authors study the effects of manganese and chromium on corrosion resistance of high manganese steels by examining the rust properties with X-ray diffraction (XRD), Raman spectroscopy, energy dispersive spectroscopy (EDS), and electron energy loss spectroscopy (EELS) adjunct to transmission electron microscopy (TEM).
- (iii) “Transition of Dislocation Structures in Severe Plastic Deformation and Its Effect on Dissolution in Dislocation Etchant,” by Muhammad Rifai, EbadBagherpour, Genki Yamamoto, Motohiro Yuasa, and Hiroyuki Miyamoto. The authors analyze the effect of SSE passes on the dissolution employing the modified Livingston etchant, which is very sensitive to dislocations.
- (iv) “Effect of Partial Cladding Pattern of Aluminum 7075 T651 on Corrosion and Mechanical Properties,” by Rendell, Hsiao, and Shirokoff. The authors estimate the clad spot to determine dimensions for a two-dimensional aluminum alloy array.
- (v) “Effect of Molybdenum on the Corrosion Behavior of High-Entropy Alloys (HEAs) CoCrFeNi<sub>2</sub> and

CoCrFeNi<sub>2</sub>Mo<sub>0.25</sub> under Sodium Chloride Aqueous Conditions,” by Alvaro Rodriguez, Joseph Tylczak, Michael Gao, Paul D. Jablonski, Martin Detroy, Margaret Ziomek-Moroz, and Jeffrey Hawk. The authors investigate the corrosion behavior of high-entropy alloys (HEAs) CoCrFeNi<sub>2</sub> and CoCrFeNi<sub>2</sub>Mo<sub>0.25</sub> in 3.5 wt. percent sodium chloride (NaCl) at 25°C by electrochemical methods.

*Alicia E. Ares*  
*Raúl B. Rebak*  
*María V. Biezma*  
*Claudia M. Méndez*

## Research Article

# Effect of Molybdenum on the Corrosion Behavior of High-Entropy Alloys CoCrFeNi<sub>2</sub> and CoCrFeNi<sub>2</sub>Mo<sub>0.25</sub> under Sodium Chloride Aqueous Conditions

Alvaro A. Rodriguez,<sup>1,2</sup> Joseph H. Tylczak<sup>1,3</sup>,<sup>ORCID</sup> Michael C. Gao,<sup>1,4</sup> Paul D. Jablonski,<sup>1,3</sup> Martin Detrois,<sup>1,4</sup> Margaret Ziomek-Moroz,<sup>1,3</sup> and Jeffrey A. Hawk<sup>1,3</sup>

<sup>1</sup>National Energy Technology Laboratory, 1450 Queen Ave. SW, Albany, OR 97321, USA

<sup>2</sup>ORISE, Oak Ridge, TN, USA

<sup>3</sup>U.S. Department of Energy, Washington, DC, USA

<sup>4</sup>AECOM, Los Angeles, CA, USA

Correspondence should be addressed to Joseph H. Tylczak; [joseph.tylczak@netl.doe.gov](mailto:joseph.tylczak@netl.doe.gov)

Received 30 September 2017; Revised 14 December 2017; Accepted 21 January 2018; Published 20 March 2018

Academic Editor: Alicia E. Ares

Copyright © 2018 Alvaro A. Rodriguez et al. This is an open access article distributed under the Creative Commons Attribution License, which permits unrestricted use, distribution, and reproduction in any medium, provided the original work is properly cited.

The corrosion behavior of high-entropy alloys (HEAs) CoCrFeNi<sub>2</sub> and CoCrFeNi<sub>2</sub>Mo<sub>0.25</sub> was investigated in 3.5 wt. percent sodium chloride (NaCl) at 25°C by electrochemical methods. Their corrosion parameters were compared to those of HASTELLOY® C-276 (UNS N10276) and stainless steel 316L (UNS 31600) to assess the suitability of HEAs for potential industrial applications in NaCl simulating seawater type environments. The corrosion rates were calculated using corrosion current determined from electrochemical experiments for each of the alloys. In addition, potentiodynamic polarization measurements can indicate active, passive, and transpassive behavior of the metal as well as potential susceptibility to pitting corrosion. Cyclic voltammetry (CV) can confirm the alloy susceptibility to pitting corrosion. Electrochemical impedance spectroscopy (EIS) elucidates the corrosion mechanism under studied conditions. The results of the electrochemical experiments and scanning electron microscopy (SEM) analyses of the corroded surfaces revealed general corrosion on alloy CoCrFeNi<sub>2</sub>Mo<sub>0.25</sub> and HASTELLOY C-276 and pitting corrosion on alloy CoCrFeNi<sub>2</sub> and stainless steel 316L.

## 1. Introduction

Studies and investigations of multicomponent solid solutions in near-equal molar ratio lead to the development of high-entropy alloys (HEAs), a new group of alloys containing at least five alloying elements with an atomic composition of 5–35% each. Even though 4 component alloys are more properly referred to as medium entropy, for this paper, both experimental alloys will be classified as HEAs. HEAs are also characterized by their configurational entropy of mixing ( $\Delta S_{\text{conf}}$ ) of at least  $1.5R$ , where  $R = 8.314 \text{ J}\cdot\text{mol}^{-1}\cdot\text{K}^{-1}$  is the gas constant.  $\Delta S_{\text{conf}}$  plays the most dominant role on the total mixing entropy [1], and ideal  $\Delta S_{\text{conf}}$  is calculated using (1). This equation is a good approximation for liquid alloys and many

solid alloys close to their solidus temperatures [1].  $X_i$  represents the mole fraction of element  $i$  [2–6].

$$\Delta S_{\text{conf}} = -R \sum_i (X_i \ln X_i). \quad (1)$$

High values of mixing entropy for an alloy favor the formation of single-phase solid solutions, over that of intermetallic compounds [2, 4]. High concentrations of multiple components offer unique physical and metallurgical properties with potential for superior mechanical, electrochemical, and magnetic characteristics suitable for applications under high-strength and high-corrosive environments such as the chemical industry, natural gas distribution systems, and marine infrastructure [7].

Studies evaluating the mechanical, chemical, and corrosion behavior of high-entropy alloys were first published in 2004, increasing to more than 500 related articles since. The electrochemical kinetics and microstructure analysis of the HEA alloy  $\text{Cu}_{0.5}\text{NiAlCoCrFeSi}$  were evaluated by Chen et al. in NaCl and  $\text{H}_2\text{SO}_4$  solutions [7, 8]. This HEA had a higher resistance to general corrosion compared to stainless steel 304S at 25°C. However, susceptibility to pitting corrosion was observed under the presence of chlorides. General corrosion resistance for the HEA and 304S decreased as temperature increased from 30°C to 70°C, with little impact on 304S due to a passive film formation. Microstructure analysis of this HEA revealed a quasicrystalline material with a matrix of a non-crystalline phase, nanoscale deposits, and body-centered cubic (BCC) elements.

The influence of copper content on the corrosion behavior of  $\text{FeCoNiCrCu}_x$  HEAs in 3.5% NaCl solution was evaluated by Hsu et al. Localized corrosion increased with copper concentration due to galvanic action between interdendrites and dendrites [9]. Comparatively, Lee et al. studied the effect of boron content on the corrosion performance of  $\text{Al}_{0.5}\text{CoCrCuFeNiB}_x$  HEAs. Electrochemical tests showed higher resistance of these HEAs to general corrosion compared to stainless steel 304, while corrosion current densities increased with higher boron content in aqueous solutions of  $\text{H}_2\text{SO}_4$  [10]. Hsu et al. found an enhancement of hardness, wear resistance, and high-temperature strength of these alloys due to the formation of boride precipitates as concentration of boron increased [11].

In 2008, Lee et al. studied the corrosion performance of  $\text{Al}_x\text{CrFe}_{1.5}\text{MnNi}_{0.5}$  HEAs in NaCl and  $\text{H}_2\text{SO}_4$  solutions by measuring their corrosion current density. The aluminum-free alloy from this system had a higher corrosion resistance in  $\text{H}_2\text{SO}_4$  solutions. However, addition of NaCl promotes the susceptibility of the HEA to pitting corrosion due to a breakdown of the existing passive layer [12].

Numerous HEA systems have been developed and evaluated by other researchers to understand the corrosion behavior of these multicomponent alloys under aqueous conditions. These studies include the influence of aluminum on the pitting corrosion of  $\text{Al}_x\text{CrFe}_{1.5}\text{MnNi}_{0.5}$  alloys in HCl solutions [13]; pitting corrosion evaluation of  $\text{Co}_{0.15}\text{CrFeNi}_{1.5}\text{Ti}_{0.5}\text{Mo}_{0.1}$  in sulfate solutions with chloride content [14], inhibition impact of inorganic/organic inhibitors in chloride solutions [15], and impact of molybdenum on  $\text{Co}_{0.15}\text{CrFeNi}_{1.5}\text{Ti}_{0.5}\text{Mo}_{0.1}$  HEAs [16].

Furthermore, an extended list of other investigations involves the corrosion behavior and pitting corrosion susceptibility of (a)  $\text{Al}_x\text{CoCrFeNi}$  alloys in NaCl environments [17] and in sulfuric acids [18]; (b) corrosion resistance of  $\text{CoCrCuFeNiAl}_{0.5}\text{B}_x$  alloys in simulated syngas at high temperatures [19]; (c) influence of alloying and heat treatments on the corrosion of Al and Cu-containing HEA systems [20]; and (d) corrosion evaluation of  $\text{TiZr}_{0.5}\text{NbCr}_{0.5}\text{V}_x\text{Mo}_y$  alloys [21] and reviews on current research and development of HEAs [4, 6, 20, 22–27].

The investigated HEA systems were  $\text{CoCrFeNi}_2$  and  $\text{CoCrFeNi}_2\text{Mo}_{0.25}$  (referred as A35 and A36 resp. throughout this paper), as well as two commercial alloys, HASTELLOY

C-276 (UNS N10276) and stainless steel 316L (UNS 31600). The purpose of this study is to assess the potential industrial applications of HEAs by comparing their cost benefit and corrosion resistance to a Ni-Mo-Cr superalloy with excellent corrosion resistance such as HASTELLOY C-276 and an austenitic stainless-steel alloy primarily formed by Fe-Cr-Ni with high corrosion resistance characteristics such as 316L.

The cost associated with fabrication can be divided into fixed and variable costs. Fixed costs remain the same unlike the production output. In contrast, variable costs are dependent of unit production. The cost of raw materials is classified as a variable cost, and it was calculated in this work based on composition of alloys, assuming that the influence of other variables such as labor, utilities, and sales commissions are similar. The raw material costs were calculated from current commodity market prices [28]. The cost of producing 1 lb. (454 g) of alloy is approximately \$1.07 for SS316, \$6.09 for C-276, \$8.39 for A35, and \$8.65 for A36. The expected high value of alloys A35 and A36 is influenced by the market price of Co; therefore, the price could drop to \$2.00–\$3.00.

The selected HEAs have a face-centered cubic (FCC) crystal structure based on 3d transition metals [29, 30]. The passive elements such as Cr and Mo add high mixing entropy and low free energy, aspects that benefit the corrosion resistance of alloys. The corrosion behavior of these alloys was evaluated via electrochemical methods by carrying out experiments in 3.5 wt.% NaCl solution, simulating artificial seawater at room temperature (25°C). Table 1 shows the alloy composition, ASTM grain size, and configurational entropy as calculated from (1).

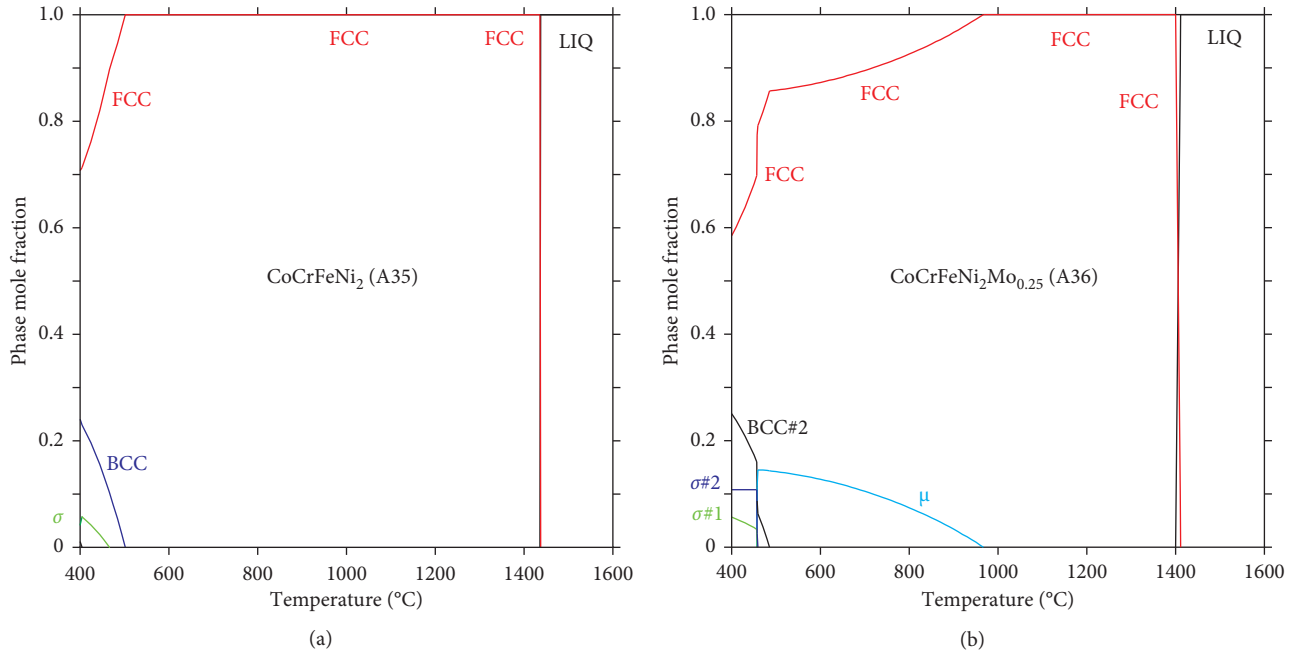
## 2. Materials and Methods

**2.1. Alloy Design and Manufacture.** The alloys were designed using the Thermo-Calc Software utilizing the TCNI8 database [31]. The idea was to keep the FCC solid solution as the main phase in the microstructure as seen in Figure 1. The base alloy  $\text{CoCrFeNi}_2$  (A35) was predicted to form a single FCC structure in the as-cast state since the FCC phase is stable over an extremely wide temperature range (i.e., 502–1435°C). Addition of Mo to the base alloy was to enhance the pitting corrosion resistance, but it promoted formation of  $\mu$  phase in small mole fractions of A36 (Figure 1(b)), starting at 967°C. The  $\mu$  phase originates from the Co-Mo and Fe-Mo binaries, and it has a hexagonal crystal structure (prototype  $\text{WFe}_7$ , Pearson symbol hR39, and space group  $R\bar{3}m$ ).

A combination of commercial purity starting materials and in-house refined Ni-Co-Cr master alloys [32, 33] were used to formulate alloys A35 and A36 with the nominal chemistries shown in Table 1 using a starting weight of approximately 8000 g. Each alloy was induction-melted under inert gas and poured with a 50°C superheat into a 75 mm cylindrical graphite mold having a nonreactive ceramic wash coat. After casting, the hot-tops of each ingot were removed with a band saw, and a 2 mm thick slice was taken for chemical analysis. The metal chemistries were determined by X-ray fluorescence (XRF) with the Rigaku ZSX Primus II utilizing National Institute of Standards and Technology

TABLE 1: Alloy compositions, grain size, and configurational entropy.

Alloy	wt.%							ppm				ASTM grain size	$\Delta S_{\text{conf}}$
	Fe	Ni	Co	Mo	Cr	Others	Others	O	N	C	S		
A35	19.98	40.84	20.67	—	18.4			11	11	165	10	6	1.3R
A36	18.46	37.81	18.99	7.64	16.95			4	9	160	10	4	1.5R
C-276	5.5	57	2.5	16	15.5	4.00 W	800 Si			100		5	1.4R
SS316	68.59	10.47	0.21	2	16.61	0.35 Cu	310 P	536	178	200		7	1.0R
						1.39 Mn	2500 Si						

FIGURE 1: Calculated equilibrium phase mole fraction versus temperature for (a)  $\text{CoCrFeNi}_2$  (A35) and (b)  $\text{CoCrFeNi}_2\text{Mo}_{0.25}$  (A36) alloys using the bulk composition provided in Table 1 (only the elements Co, Cr, Fe, Ni, and Mo were included).

(NIST) traceable standards (reported values are accurate to 0.01 wt.%); carbon and sulfur chemistries were determined with a LECO CS444LS using NIST-certified standards (reported values are accurate to 2 ppm). Oxygen and nitrogen chemistries were determined with a LECO TC436AR using NIST certified standards (reported values are accurate to 1 ppm). Each ingot was given a computationally optimized homogenization heat treatment to reduce the inhomogeneity to  $\pm 1\%$  of nominal or better utilizing the method described in [34]. The sidewalls of the ingots were conditioned on a lathe, and the ingots were bagged in protective stainless-steel foil pouches and preheated for 3 hours prior to fabrication. Alloy A35 was hot worked at  $900^\circ\text{C}$  while alloy A36 was hot worked at  $1100^\circ\text{C}$  due to the more refractory nature of the alloy. Hot working consisted of forging and rolling to reduce the round ingots into slab shapes, which were ultimately formed into strip product with a thickness of approximately 3.7 mm.

**2.2. Microstructure Characterization.** Metal specimens ( $10\text{ mm} \times 10\text{ mm} \times 3\text{ mm}$ ) of HEAs A35 and A36 were cut from prepared corrosion specimens (machining is described

below and seen in Figure 2) by mounting the top face of the rolled plates on a conductive epoxy using a hot compression method. Therefore, the broad, rolled face is considered for observation of micrographs for convenience due to the thin nature of the plates. Preparation of the untested specimens for observation of the starting microstructures included mechanical wet grinding employing SiC paper through to 1200 grit followed by final polishing using alumina suspension on fine polishing cloths through a  $0.05\ \mu$  size. The metal surface of the samples was etched using an electrolytic method at 1.5 V for 60 sec in a bath of acetic acid, nitric acid, and water at room temperature (described as etchant 50 in standard ASTM E407-07) [35]. The general grain structure was observed using optical microscopy while the corrosion tested samples were observed under an FEI Inspect F scanning electron microscope (SEM).

**2.3. Electrochemical Testing.** Experiments were conducted at  $25^\circ\text{C}$  in a nondeaerated test solution of 3.5 wt.% NaCl. A three-electrode electrochemical glass cell was used with the metal specimen as the working electrode, a standard calomel

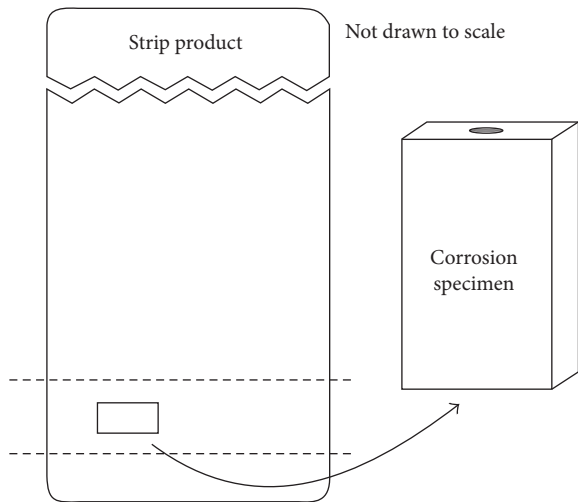


FIGURE 2: Preparation of corrosion specimens from the hot rolled strip.

electrode (SCE) as the reference electrode, and a platinum sheet as the counter electrode. A Luggin capillary tube was employed to reduce uncompensated IR drop. Electrochemical experiments were carried out using a Gamry Reference 600+ potentiostat/galvanostat/ZRA and data processed with Gamry Echem Analyst software.

Corrosion specimens (15 mm × 10 mm × 3 mm) were machined from the strip product of the round ingots. The strip plate had approximate dimensions of 33 cm by 15 cm with thickness of 3.77 mm. Specimens were cut from the delineated area (Figure 2) by first rough cutting the plate on a band saw, then squaring the material on a milling machine. Metal samples were further squared using carbide end mills and face mills to achieve a better finish. A 3–48 threaded hole was then tap drilled on one of the 10 by 3 mm ends. For the last step, an abrasive slurry of silicon carbide and a lapping machine were used to remove tool marks from the sides and faces of the samples.

Prior to electrochemical testing, bare corrosion specimens were wet ground through a 600-grit finish using SiC grinding paper, degreased with acetone, and air dried. Specimens were screwed tightly at the end of a threaded rod sample holder before immersion in the electrolyte solution.

Before each electrochemical test, metal specimens are kept at a potential of 800 mV more negative than the free potential for 2 minutes, and the open circuit potential ( $E_{oc}$ ) was measured for 30 minutes.

Potentiodynamic polarization measurements were carried out to evaluate the anodic electrochemical behavior and determine susceptibility to general and pitting corrosion of the alloys by applying a fixed voltage scan rate of 1 mV/s from an initial potential of  $-0.25$  V versus  $E_{oc}$  to a final potential of 1.6 V versus  $E_{oc}$ .

Cyclic potentiodynamic polarization measurements were performed to determine relative susceptibility to localized corrosion. These tests were performed at a fixed voltage scanning rate of 1 mV/s. The initial potential scan started at  $-0.25$  V versus  $E_{oc}$  to an anodic potential of 1.5 V versus  $E_{oc}$ , where the potential value was reversed to the initial value.

Electrochemical impedance spectroscopy (EIS) is a nondestructive technique to evaluate the performance of passive film formation on an alloy. Measurements were carried out in the potentiostatic mode using a frequency range between 100 kHz and 10 mHz while applying an amplitude of the AC signal of 10 mV-rms.

### 3. Results and Discussion

**3.1. Microstructure Characterization.** The average grain size for the microstructure of HEAs A35 and A36 is 40  $\mu\text{m}$  (std. dev.: 4.8) and 86  $\mu\text{m}$  (std. dev.: 7.5), respectively. This was determined using the linear intersect technique on images presented in Figures 3(a) and 3(b). The size difference of the grain is attributed to the hot working process of A35 (900°C) versus A36 (1100°C). The optical micrographs reveal an equiaxed grain structure indicating full recrystallization during the forging and rolling processes. Furthermore, SEM observation at higher magnifications (not shown) revealed a single-phase microstructure being in agreement with the predictions presented in Figure 1 with only small inclusions from casting. No  $\mu$  phase was observed. The electrochemical behavior of the alloys is affected by changes in grain refinement by introducing more grain boundaries, modifying grain orientation, and hindering dislocation motion [36]. Finer grain size leads to greater grain boundaries, acting as weak spots for preferential corrosion initiation sites. SEM images of the cross section of samples A35 and A36 can be seen in Figures 4(a) and 4(b), respectively, where the formation of a protective passive layer along the grain boundaries of alloy A36 (also seen in Figures 5(d) and 5(e)) confirms the effect of grain size on the corrosion resistance of this alloy after electrochemical polarization experiments. On the other hand, alloy A35 presents further attack of a less effective passive layer at initiation sites leading to localized corrosion.

**3.2. Electrochemical Testing.** Potentiodynamic polarization curves of all specimens are shown in Figure 6. The corrosion resistance of alloys C-276 and SS316 under aqueous conditions has been extensively studied in the literature [37–39], and their corrosion mechanisms are not discussed here. HEAs A35 and A36 and commercial alloys C-276 and SS316 do not exhibit an anodic active region represented by a straight potential-current line in 3.5 wt.% NaCl. However, the cathodic reaction seen as a straight line indicates electron-transfer control. All the alloys present passive regions making them less susceptible to general corrosion. HEA A35 presents a pseudopassive curve with a breakdown potential of 0.32 V versus SCE where metastable pitting starts occurring. HEA A36 displays the highest breakdown potential at 0.91 V versus SCE, making it less susceptible to localized corrosion. Alloy C-276 exhibits three regions, a passive region with a breakdown potential of 0.74 V versus SCE, a transpassive region, and a secondary passive region with a potential of 1.12 V versus SCE. Finally, alloy SS316 has the lowest breakdown potential (0.27 V versus SCE) of all evaluated materials.

In this study, the NaCl solution has an initial pH of 8.4 before potentiodynamic polarization experiments were

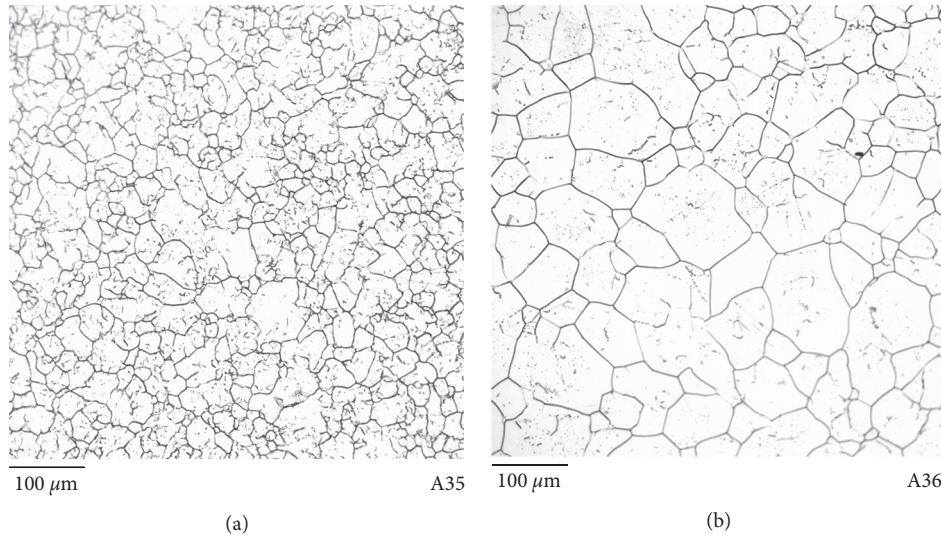


FIGURE 3: Micrograph of the as-cast HEAs A35 (a) and A36 (b).

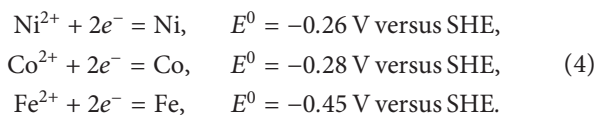
carried out. The final pH of the solution was measured as 10.9 for alloy A35 and 10.1 for A36.

Alloy A35 underwent pseudopassive behavior between its corrosion potential ( $E_{\text{corr}}$ ) of  $-0.29$  V versus SCE ( $-0.05$  versus SHE) and its breakdown potential ( $E_{\text{bre}}$ ) of  $0.32$  V versus SCE ( $0.56$  V versus SHE). At these potentials and according to Pourbaix diagrams [40], Co, Fe, and Ni are active species while Cr is passive. The passivation of the alloy is caused by the formation of a stable chromium oxide layer on the surface in the form of  $2\text{Cr} + 3\text{H}_2\text{O} = 2\text{Cr}_2\text{O}_3 + 6\text{H}^+ + 6e^-$ . The breakdown of this oxide layer is the first step in the localized damage of this protective layer by the chemical attack of aggressive species such as chlorides. The oxide film is locally attacked  $\text{Cr}_2\text{O}_3 + 5\text{H}_2\text{O} = 2\text{CrO}_4^{2-} + 10\text{H}^+ + 6e^-$  at weak spots, where inclusions or mechanical flaws permit the transport of ions (accelerated by chloride ions) at these sites forming anodic active behavior [41].

At the  $E_{\text{bre}}$ , nucleation, growth, and repassivation of metastable pits occur where the passive film has broken down possibly initiated by sulfur inclusions. The standard cell potential ( $E_{\text{cell}}^0$ ) of the galvanic couple Ni-Co and Ni-Fe was determined by (2), and its Gibbs free energy ( $\Delta G^0$ ) is given by (3), where  $n$  is the number of electrons passed per atom of Ni reacted and  $F$  is the charge on a mole of electrons ( $96485.33$  C/mol) [42, 43]. In both cases, Ni is the cathode, and the half reactions are shown below [44]:

$$E_{\text{cell}}^0 = E_{\text{cathode}}^0 - E_{\text{anode}}^0 \quad (2)$$

$$\Delta G^0 = -nFE_{\text{cell}}^0 \quad (3)$$



Predominant nickel dissolution species according to Pourbaix diagrams and later studied by Beverskog and Puigdomenech [45] appear as  $\text{Ni} = \text{Ni}^{2+} + 2e^-$  in the first

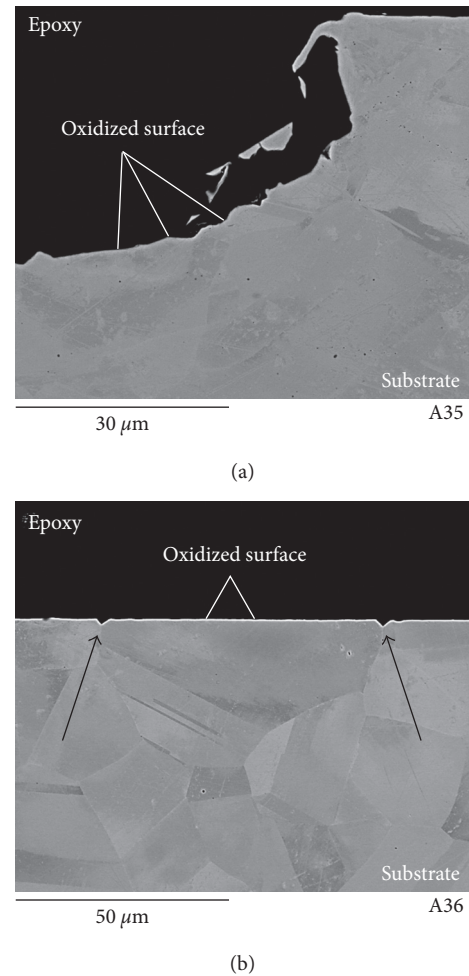


FIGURE 4: SEM micrographs of alloys A35 (a) and A36 (b) after potentiodynamic polarization experiments (cross sections).

stage, then transition as pH increases to ionic species precipitating in solution by hydrolysis  $\text{Ni}^{2+} + \text{OH}^- = \text{NiOH}^+$ , and further react to  $\text{Ni}^{2+} + 3\text{OH}^- = \text{Ni}(\text{OH})_3^-$ . The ratio of

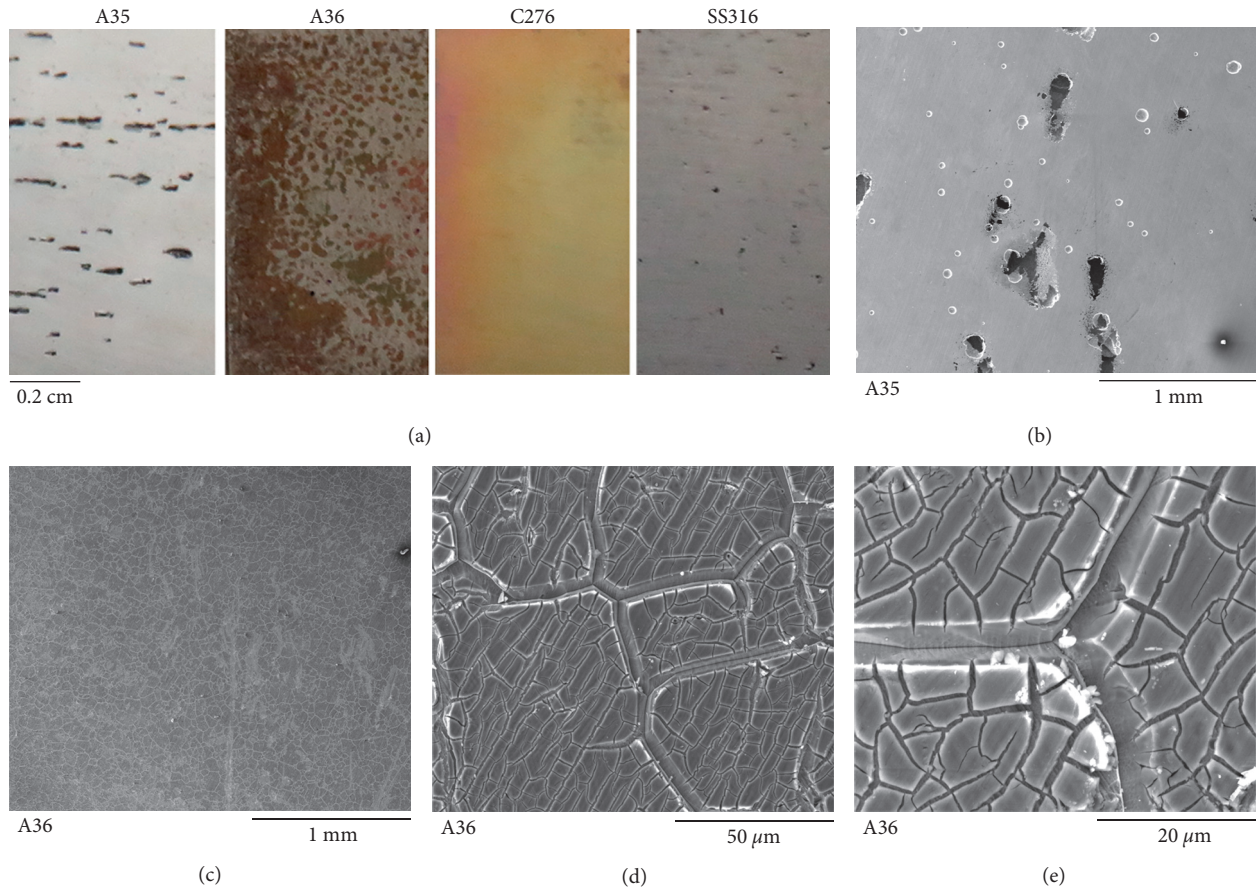


FIGURE 5: Photographs (a), SEM images of HEA A35 (b), and HEA A36 at different magnifications (c, d, e) after anodic polarization exposure of samples in 3.5 wt.% NaCl solution at 25°C.

Ni:Co and Ni:Fe in the alloy is 2:1, resulting on higher current density on the anode, favoring corrosion of Fe and Co. Results of  $E_{\text{cell}}^0$  for the Ni-Co galvanic couple is 0.02 V versus SHE, while for Ni-Fe is 0.19 V versus SHE. Both reactions occur spontaneously as  $\Delta G^0$  was calculated as  $-4.44$  KJ/mol for Ni-Co and  $-36.66$  KJ/mol for Ni-Fe.

Thermodynamically stable species of Fe and Co are formed from anodic oxidation processes, and Pourbaix diagrams indicate the following path for Fe and Co, respectively:  $\text{Fe} = \text{Fe}^{2+} + 2e^-$  and  $2\text{Fe} + 3\text{H}_2\text{O} = \text{Fe}_2\text{O}_3 + 6\text{H}^+ + 6e^-$ ;  $\text{Co} = \text{Co}^{2+} + 2e^-$ ; and  $\text{Co} + 2\text{H}_2\text{O} = \text{Co}(\text{OH})_2 + 2\text{H}^+ + 2e^-$ .

The pseudopassive area of alloy A36 lies between its  $E_{\text{corr}}$  of  $-0.26$  V versus SCE ( $-0.02$  versus SHE) and  $E_{\text{bre}}$  of  $0.91$  V versus SCE ( $1.15$  V versus SHE). Co, Fe, and Ni are active species at these potentials while Cr and Mo are passive. In addition to the formation of a layer of chromium oxide ( $\text{Cr}_2\text{O}_3$ ), responsible for the passive behavior, Mo increases the stability of the protective layer and enhances  $E_{\text{bre}}$  by precipitation of Mo species on the surface at pH values higher than 8.0 [16, 46, 47]  $\text{Mo} + 2\text{H}_2\text{O} = \text{MoO}_2 + 4\text{H}^+ + 4e^-$ . Studies have shown that not only Mo interacts with S by removing it from the surface, but it contributes to localized repair of local weak spots [47]. Transpassivity of Mo occurs by further oxidation at higher potentials  $\text{MoO}_2 + 2\text{H}_2\text{O} = \text{MoO}_4^{2-} + 4\text{H}^+ + 2e^-$  [41, 48].

As it was discussed for alloy A35, Ni, Fe, and Co species preferentially dissolve in solution. This corrosion mechanism further contributes to Mo enrichment on alloy A36 surface leading to greater corrosion resistance properties.

Electrochemical parameters ( $E_{\text{corr}}$ ), corrosion current density ( $i_{\text{corr}}$ ), and breakdown potential ( $E_{\text{bre}}$ ) are shown in Table 2 where the corrosion rate (CR) is determined by

$$\text{CR} = \frac{I_{\text{corr}} \cdot K \cdot \text{EW}}{d \cdot A}, \quad (5)$$

where  $I_{\text{corr}}$  is the corrosion current in amperes and calculated using the Tafel extrapolation method where the cathodic reaction is diffusion controlled;  $K$  is a constant equal to  $3.27 \times 10^3$  with units of mm/y; the equivalent weight (EW) is a dimensionless unit that represents the mass of the metal species that will react with one Faraday of charge;  $d$  is the density of the metal in  $\text{g}/\text{cm}^3$ ; and  $A$  is the area exposed to corrosion [49].

Calculated corrosion rate values are similar with very small variations from each other. Accordingly, results of  $E_{\text{corr}}$  and  $i_{\text{corr}}$  fall within comparable ranges in the transition process of cathodic and anodic half reactions in the polarization curves.

Localized attack in the form of pitting corrosion was seen in metal alloys A35 and SS316 after potentiodynamic polarization tests (Figure 5(a)). The average pit size and

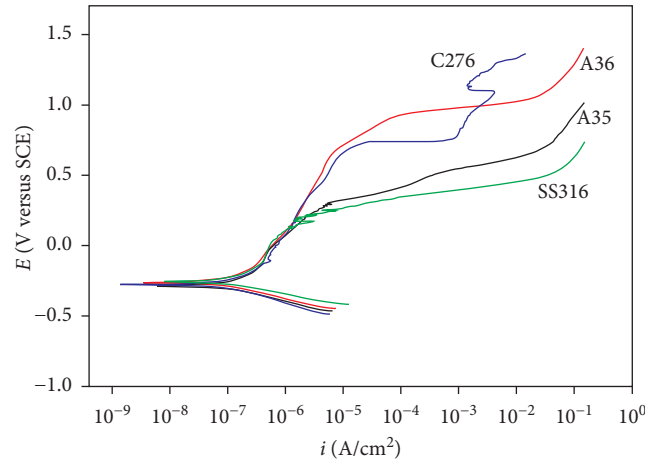


FIGURE 6: Potentiodynamic polarization curves of HEAs A35 and A36 and commercial alloys C-276 and SS316 in 3.5 wt.% NaCl solution saturated at 25°C.

TABLE 2: Electrochemical parameters for HEAs A35 and A36 and commercial alloys C-276 and SS316 in 3.5 wt.% NaCl solution at 25°C.

Alloy	$E_{corr}$ (V versus SCE)	$E_{bre}$ (V versus SCE)	$i_{corr}$ (A/cm <sup>2</sup> )	CR (mpy)
A35	-0.29	0.32	$1.29 \times 10^{-7}$	0.052
A36	-0.26	0.91	$1.25 \times 10^{-7}$	0.048
C-276	-0.28	0.74	$1.28 \times 10^{-7}$	0.056
SS316	-0.25	0.27	$1.11 \times 10^{-7}$	0.049

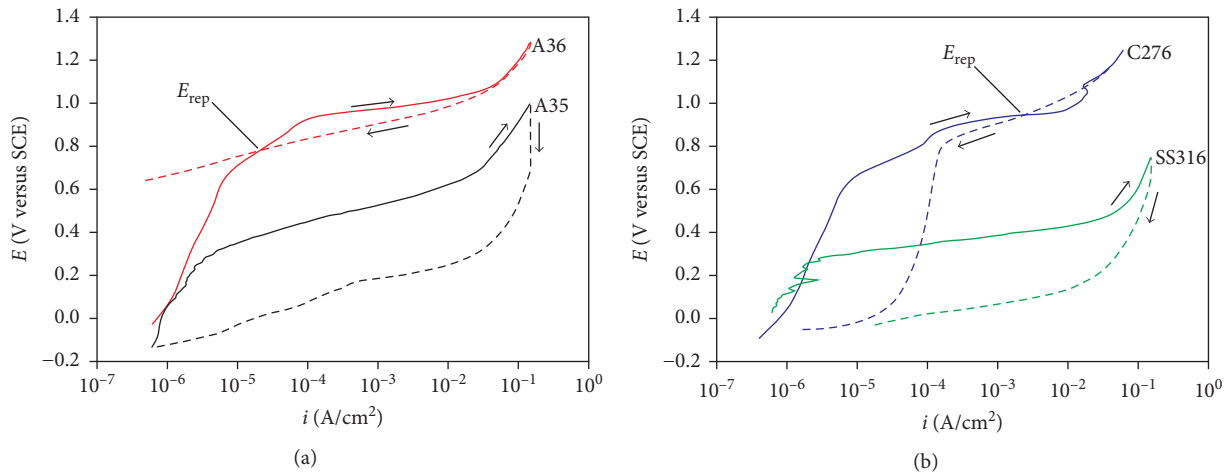


FIGURE 7: Cyclic anodic polarization curves of A35, A36, C-276, and SS316 alloys in 3.5 wt.% NaCl solution at 25°C.

pitting density area for A35 and SS316 are  $0.19 \mu\text{m}$  (6.2%) and  $0.03 \mu\text{m}$  (7.7%), respectively. In contrast, A36 and C-276 developed the formation of a passive film due to a high breakdown potential, increasing resistance to pitting or crevice corrosion. Even though chromium content promotes the formation of this passive film in aqueous solutions under potentiodynamic polarization, film stability increases with content of molybdenum [38].

SEM images revealed large pitting corrosion evolution in sample A35 (Figure 5(b)) and the formation of an

inner amorphous corrosion layer in sample A36 (Figure 5 (c)). Similar to other studies [50], the fine scale channels in Figures 5(d) and 5(e) (cracking of the inner amorphous corrosion layer) are attributed to the dehydration effect during sample storage. However, the larger channels most likely follow the grain boundaries (arrows in Figure 4(b)).

Cyclic anodic polarization curves of A35, A36, C-276, and SS316 alloys are shown in Figure 7. The behavior of the potential at which the hysteresis loop is completed upon

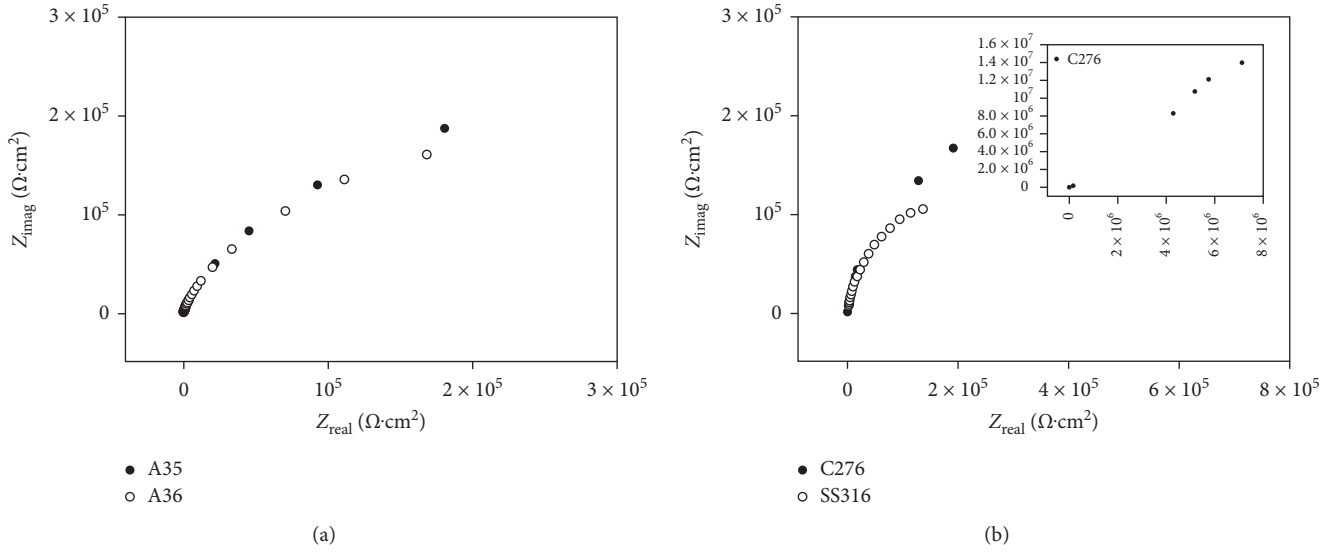


FIGURE 8: Nyquist plots of A35, A36, C-276, and SS316 alloys in 3.5 wt.% NaCl solution at 25°C.

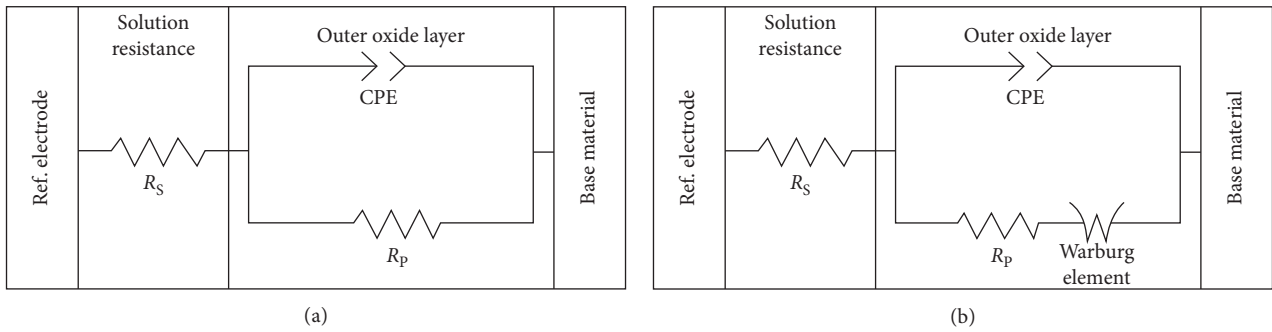


FIGURE 9: Equivalent electrical circuit (a) used for fitting experimental data of alloy SS316, while circuit (b) was used for A35, A36, and C-276 alloys.  $R_s$  is the resistance of the electrolyte solution,  $R_p$  is the oxide layer resistance, and CPE accounts for a nonideal capacitor.

TABLE 3: Electrochemical parameters for A35, A36, C-276, and SS316 alloys in 3.5 wt.% NaCl solution at 25°C.

Alloy	$R_p$ ( $\Omega\cdot\text{cm}^2$ )	$R_u$ ( $\Omega\cdot\text{cm}^2$ )	$C_{\text{CPE}}$ ( $\text{F}/\text{cm}^2$ )	$\alpha$	$W_d$ ( $\text{S}/\text{s}^{0.5}$ )
A35	$3.49 \times 10^5$	1.51	$2.00 \times 10^{-4}$	0.88	$1.79 \times 10^{-4}$
A36	$3.45 \times 10^5$	2.36	$2.17 \times 10^{-4}$	0.89	$1.06 \times 10^0$
C-276	$3.71 \times 10^5$	8.23	$7.29 \times 10^{-4}$	0.89	$9.83 \times 10^{-1}$
SS316	$2.61 \times 10^5$	2.68	$4.37 \times 10^{-4}$	0.85	—

reverse polarization scan determines the susceptibility to the initiation of localized corrosion.

Although all alloys display hysteresis under this high anodic polarization, A36 and C-276 have significantly higher  $E_{\text{bre}}$  and repassivation potentials ( $E_{\text{rep}}$ ) than the A35 and SS316 alloys. Consequently, A36 and C-276 are relatively more resistant to pitting corrosion than A35 and SS316 in this environment, due mainly to a small potential difference between  $E_{\text{rep}}$  and  $E_{\text{bre}}$ .

A theoretical indication can also be confirmed by evaluating the pitting resistant equivalent (PRE) value of C-276 and SS316. These values are based on the chemical composition of an alloy, with values of 45 and 21 for C-276 and SS316, respectively [51].

Higher values provide higher corrosion resistance, but may lead to the potential formation of sigma and alpha prime phase. Values in the range of 40–45 will minimize formation of these phases and are desired in the industry [52].

Electrochemical impedance spectroscopy measurements of all alloys studied in this work are represented as Nyquist plots in Figure 8. Experimental data were fit using the equivalent electrical circuits in Figure 9, while electrochemical parameters for each alloy are shown in Table 3.

The circuit model  $R_s$  (CPE// $R_p$ ) in Figure 8(a) was used for fitting the experimental impedance data for alloy SS316. This circuit includes the resistance of the electrolyte solution  $R_s$  in series with a parallel combination of a constant phase

element (CPE)—accounting for a nonideal capacitor—and the oxide layer resistance ( $R_p$ ). Experimental data for alloys A35, A36, and C-276 were fitted using the circuit model in Figure 8(b) where Warburg impedance element ( $W_d$ ) represents diffusive processes (mass transfer) on the surface.

The charge transfer at the metal/electrolyte interface is directly related to the passive film properties of the surface. Higher corrosion resistance was observed for the C-276 alloy due to its passivation ability.

#### 4. Conclusions

The corrosion behavior of HEAs from the CoCrFeNi<sub>2</sub> and CoCrFeNi<sub>2</sub>Mo<sub>0.25</sub> systems was evaluated in a nondeaerated solution of 3.5 wt.% NaCl at 25°C, and their performance was compared to commercial alloys C-276 and SS316 via electrochemical testing.

The electrochemical behavior of the alloys is affected by changes in grain refinement. Finer grain size of alloy A35 presented an increase of weak spots for pitting initiation at preferential sites. On the other hand, alloy A36 formed a protective passive layer along the grain boundaries contributing to higher corrosion resistance.

Potentiodynamic polarization results indicated that chloride ions adsorb on the metal surface of alloys A35 and SS316 breaking down passivity. The attack of this passivity is localized and favors the formation of pits, seen during microscopic imaging analysis. The pit size observed on A35 and SS316 was 0.19  $\mu\text{m}$  and 0.03  $\mu\text{m}$ , respectively. A higher content of molybdenum in SS316 may result in a better stability of the passive layer compared to A35.

In the case of alloys A36 and C-276, potentiodynamic polarization results indicated that both passivate in NaCl forming a protective layer against pitting corrosion. Microscopic investigations revealed no formation of pits and a cracked film on the surface of alloy A36, due to a possible film dehydration effect after electrochemical experiments.

Alloy A35 underwent pseudopassive behavior between its  $E_{\text{corr}}$  of  $-0.29$  V versus SCE ( $-0.05$  versus SHE) and its  $E_{\text{bre}}$  of  $0.32$  V versus SCE ( $0.56$  V versus SHE). Passivation of the alloy is caused by the formation of Cr<sub>2</sub>O<sub>3</sub>, yet chemical attack of chlorides initiates breakdown of this oxide layer and initiation of pitting corrosion. Ni acts as the cathode on the galvanic couple Ni-Co and Ni-Fe, where Ni species dissolve and precipitate in solution by hydrolysis. Higher concentration of Ni favors corrosion of Fe and Co species.

The pseudopassive area of alloy A36 lies between its  $E_{\text{corr}}$  of  $-0.26$  V versus SCE ( $-0.02$  versus SHE) and  $E_{\text{bre}}$  of  $0.91$  V versus SCE ( $1.15$  V versus SHE). In addition to the formation of a layer of Cr<sub>2</sub>O<sub>3</sub>, responsible for the passive behavior, Mo increases the stability of the protective layer and enhances  $E_{\text{bre}}$  by precipitation of MoO<sub>2</sub> on the surface at pH values higher than 8.0. Transpassivity of Mo occurs by further oxidation at higher potentials:  $\text{MoO}_2 + 2\text{H}_2\text{O} = \text{MoO}_4^{2-} + 4\text{H}^+ + 2e^-$ . As it was discussed for alloy A35, Ni, Fe, and Co species preferentially dissolve in solution to further contribute to Mo enrichment on alloy A36 surface leading to greater corrosion resistance properties.

The results obtained from cyclic polarization experiments revealed large hysteresis and less electropositive potentials for alloys A35 and SS316, indicating the susceptibility of pitting corrosion. Alloys A36 and C-276 developed a passive layer after potentiodynamic polarization and exhibited a small potential difference between  $E_{\text{rep}}$  and  $E_{\text{bre}}$ , making them more resistant to pitting corrosion in NaCl.

Electrochemical impedance spectroscopy results indicate that alloy C-276 had the highest charge transfer value at the metal/electrolyte interface. This parameter represents favorable characteristics of the passive film and consequently higher corrosion resistance due to its passivation ability in NaCl.

The role of molybdenum on the corrosion performance of HEAs A35 and A36 demonstrated its influence on the passivation ability of A36 by (1) providing a corrosion protective layer and (2) avoiding the evolution of pitting corrosion. The formation and stability of this passive layer was highly influenced by Mo content in C-276 (16 wt.% versus 7.64 wt% in A36).

#### Disclosure

This report was prepared as an account of work sponsored by the Department of Energy, National Energy Technology Laboratory, an agency of the United States government, through a support contract with AECOM. Neither the United States government nor any agency thereof, nor any of their employees, makes any warranty, expressed or implied, or assumes any legal liability or responsibility for the accuracy, completeness, or usefulness of any information, apparatus, product, or process disclosed or represents that its use would not infringe privately owned rights. Reference herein to any specific commercial product, process, or service by trade or name, trademark, manufacturer, or others does not necessarily constitute or imply its endorsement, recommendation, or favoring by the United States government or any agency thereof. The views and opinions of authors expressed herein do not necessarily state or reflect those of the United States government or any agency thereof.

#### Conflicts of Interest

The authors declare that they have no conflicts of interest.

#### Acknowledgments

The authors would like to thank Mr. Edward Argetsinger and Mr. Joseph Mendenhall for assistance in melting, Mr. Trevor Godell in machining the corrosion samples, and Mr. Matt Fortner and Christopher McKaig in sample preparation. This research was supported in part by an appointment to the U.S. Department of Energy (DOE) Postgraduate Research Program at the National Energy Technology Laboratory (NETL) administered by the Oak Ridge Institute for Science and Education. Research performed by AECOM Staff was conducted under the RES Contract DE-FE-0004000.

## References

- [1] M. C. Gao, C. Zhang, P. Gao et al., "Thermodynamics of concentrated solid solution alloys," *Current Opinion in Solid State and Materials Science*, vol. 21, no. 5, pp. 238–251, 2017, in press.
- [2] G. R. Holcomb, J. Tylczak, and C. Carney, "Oxidation of CoCrFeMnNi high entropy alloys," *Journal of the Minerals, Metals & Materials Society (JOM)*, vol. 67, no. 10, pp. 2326–2339, 2015.
- [3] P. D. Jablonski, J. J. Licavoli, M. C. Gao, and J. A. Hawk, "Manufacturing of high entropy alloys," *Journal of The Minerals, Metals & Materials Society (JOM)*, vol. 67, no. 10, pp. 2278–2287, 2015.
- [4] M. C. Gao, J.-W. Yeh, P. K. Liaw, and Y. Zhang, *High-Entropy Alloys: Fundamentals and Applications*, Springer, Cham, Switzerland, 2016.
- [5] D. Miracle, J. Miller, O. Senkov, C. Woodward, M. Uchic, and J. Tiley, "Exploration and development of high entropy alloys for structural applications," *Entropy*, vol. 16, no. 1, pp. 494–525, 2014.
- [6] M.-H. Tsai and J.-W. Yeh, "High-entropy alloys: a critical review," *Materials Research Letters*, vol. 2, no. 3, pp. 107–123, 2014.
- [7] Y. Y. Chen, U. T. Hong, H. C. Shih, J. W. Yeh, and T. Duval, "Electrochemical kinetics of the high entropy alloys in aqueous environments—a comparison with type 304 stainless steel," *Corrosion Science*, vol. 47, no. 11, pp. 2679–2699, 2005.
- [8] Y. Y. Chen, T. Duval, U. D. Hung, J. W. Yeh, and H. C. Shih, "Microstructure and electrochemical properties of high entropy alloys—a comparison with type-304 stainless steel," *Corrosion Science*, vol. 47, no. 9, pp. 2257–2279, 2005.
- [9] Y.-J. Hsu, W.-C. Chiang, and J.-K. Wu, "Corrosion behavior of FeCoNiCrCux high-entropy alloys in 3.5% sodium chloride solution," *Materials Chemistry and Physics*, vol. 92, no. 1, pp. 112–117, 2005.
- [10] H. C. Shih, C. P. Lee, Y. Y. Chen, C. H. Wu, C. Y. Hsu, and J. W. Yeh, "Effect of boron on the corrosion properties of Al<sub>0.5</sub>CoCrCuFeNi<sub>Bx</sub> high entropy alloys in 1N sulfuric acid," *ECS Transactions*, vol. 2, no. 26, pp. 15–33, 2007.
- [11] C.-Y. Hsu, J.-W. Yeh, S.-K. Chen, and T.-T. Shun, "Wear resistance and high-temperature compression strength of Fcc CuCoNiCrAl<sub>0.5</sub>Fe alloy with boron addition," *Metallurgical and Materials Transactions A*, vol. 35, no. 5, pp. 1465–1469, 2004.
- [12] C. P. Lee, C. C. Chang, Y. Y. Chen, J. W. Yeh, and H. C. Shih, "Effect of the aluminium content of Al<sub>x</sub>CrFe<sub>1.5</sub>MnNi<sub>0.5</sub> high-entropy alloys on the corrosion behaviour in aqueous environments," *Corrosion Science*, vol. 50, no. 7, pp. 2053–2060, 2008.
- [13] C. P. Lee, Y. Y. Chen, C. Y. Hsu, J. W. Yeh, and H. C. Shih, "Enhancing pitting corrosion resistance of Al<sub>x</sub>CrFe<sub>1.5</sub>MnNi<sub>0.5</sub> high-entropy alloys by anodic treatment in sulfuric acid," *Thin Solid Films*, vol. 517, no. 3, pp. 1301–1305, 2008.
- [14] Y. L. Chou, Y. C. Wang, J. W. Yeh, and H. C. Shih, "Pitting corrosion of the high-entropy alloy Co<sub>1.5</sub>CrFeNi<sub>1.5</sub>Ti<sub>0.5</sub>Mo<sub>0.1</sub> in chloride-containing sulphate solutions," *Corrosion Science*, vol. 52, no. 10, pp. 3481–3491, 2010.
- [15] Y. L. Chou, J. W. Yeh, and H. C. Shih, "Effect of inhibitors on the critical pitting temperature of the high-entropy alloy Co<sub>1.5</sub>CrFeNi<sub>1.5</sub>Ti<sub>0.5</sub>Mo<sub>0.1</sub>," *Journal of the Electrochemical Society*, vol. 158, no. 8, pp. C246–C251, 2011.
- [16] Y. L. Chou, J. W. Yeh, and H. C. Shih, "The effect of molybdenum on the corrosion behaviour of the high-entropy alloys Co<sub>1.5</sub>CrFeNi<sub>1.5</sub>Ti<sub>0.5</sub>Mo<sub>x</sub> in aqueous environments," *Corrosion Science*, vol. 52, no. 8, pp. 2571–2581, 2010.
- [17] C.-M. Lin and H.-L. Tsai, "Evolution of microstructure, hardness, and corrosion properties of high-entropy Al<sub>0.5</sub>CoCrFeNi alloy," *Intermetallics*, vol. 19, no. 3, pp. 288–294, 2011.
- [18] Y.-F. Kao, T.-D. Lee, S.-K. Chen, and Y.-S. Chang, "Electrochemical passive properties of Al<sub>x</sub>CoCrFeNi (x = 0, 0.25, 0.50, 1.00) alloys in sulfuric acids," *Corrosion Science*, vol. 52, no. 3, pp. 1026–1034, 2010.
- [19] Ö. N. Doğan, B. C. Nielsen, and J. A. Hawk, "Elevated-temperature corrosion of CoCrCuFeNiAl<sub>0.5</sub>B<sub>x</sub> high-entropy alloys in simulated syngas containing H<sub>2</sub>S," *Oxidation of Metals*, vol. 80, no. 1, pp. 177–190, 2013.
- [20] Z. Tang, L. Huang, W. He, and K. P. Liaw, "Alloying and processing effects on the aqueous corrosion behavior of high-entropy alloys," *Entropy*, vol. 16, no. 12, pp. 895–911, 2014.
- [21] J. Li, X. Yang, R. Zhu, and Y. Zhang, "Corrosion and serration behaviors of TiZr<sub>0.5</sub>NbCr<sub>0.5</sub>V<sub>x</sub>Mo<sub>y</sub> high entropy alloys in aqueous environments," *Metals*, vol. 4, no. 4, pp. 597–608, 2014.
- [22] E. J. Pickering and N. G. Jones, "High-entropy alloys: a critical assessment of their founding principles and future prospects," *International Materials Reviews*, vol. 61, no. 3, pp. 183–202, 2016.
- [23] Y. Shi, B. Yang, and K. P. Liaw, "Corrosion-resistant high-entropy alloys: a review," *Metals*, vol. 7, no. 2, p. 43, 2017.
- [24] Y. F. Ye, Q. Wang, J. Lu, C. T. Liu, and Y. Yang, "High-entropy alloy: challenges and prospects," *Materials Today*, vol. 19, no. 6, pp. 349–362, 2016.
- [25] J.-W. Yeh, "Alloy design strategies and future trends in high-entropy alloys," *Journal of The Minerals, Metals & Materials Society (Jom)*, vol. 65, no. 12, pp. 1759–1771, 2013.
- [26] Y. Zhang, T. T. Zuo, Z. Tang et al., "Microstructures and properties of high-entropy alloys," *Progress in Materials Science*, vol. 61, pp. 1–93, 2014.
- [27] D. B. Miracle and O. N. Senkov, "A critical review of high entropy alloys and related concepts," *Acta Materialia*, vol. 122, pp. 448–511, 2017.
- [28] InfoMine, "Mining markets and investment," 2017, <http://www.infomine.com/investment/>.
- [29] M. Gao and D. Alman, "Searching for next single-phase high-entropy alloy compositions," *Entropy*, vol. 15, no. 10, pp. 4504–4519, 2013.
- [30] B.-R. Chen, A.-C. Yeh, and J.-W. Yeh, "Effect of one-step recrystallization on the grain boundary evolution of CoCrFeMnNi high entropy alloy and its subsystems," *Scientific Reports*, vol. 6, no. 1, p. 22306, 2016.
- [31] Thermo-Calc Software.
- [32] M. Detrois and P. D. Jablonski, "Trace element control in binary Ni-25cr and ternary Ni-30co-30cr master alloy castings," 2017.
- [33] P. D. Jablonski, M. Cretu, and J. Nauman, "Considerations for the operation of a small scale ESR furnace," in *Proceedings of the Liquid Metal Processing & Casting Conference*, pp. 157–162, Philadelphia, PA, USA, 2017.
- [34] P. D. Jablonski and J. A. Hawk, "Homogenizing advanced alloys: thermodynamic and kinetic simulations followed by experimental results," *Journal of Materials Engineering and Performance*, vol. 26, no. 1, pp. 4–13, 2017.
- [35] ASTM, *Standard Practice for Microetching Metals and Alloys*, ASTM International, West Conshohocken, PA, USA, 2015.

- [36] K. D. Ralston and N. Birbilis, "Effect of grain size on corrosion: a review," *Corrosion*, vol. 66, no. 7, pp. 075005–075005-13, 2010.
- [37] P. Crook, *Corrosion of Nickel and Nickel-Base Alloys*, vol. 13 of ASM Handbook, *Corrosion: Materials*, S. Cramer and B. Covino, Eds., ASM International, Materials Park, OH, USA.
- [38] J. R. Davis, *ASM Specialty Handbook: Stainless Steels*, ASM International, Materials Park, OH, USA, 1994.
- [39] J. Sedriks, *Corrosion of Stainless Steels*, John Wiley & Sons, Inc., Hoboken, NJ, USA, 2nd edition, 1996.
- [40] M. Pourbaix, *Atlas of Electrochemical Equilibria in Aqueous Solutions*, NACE International, Houston, TX, USA, 1974.
- [41] A. K. Mishra and D. W. Shoesmith, "The activation/depasivation of nickel–chromium–molybdenum alloys: an oxyanion or a pH effect—Part II," *Electrochimica Acta*, vol. 102, pp. 328–335, 2013.
- [42] A. Bard and L. Faulkner, *Electrochemical Methods-Fundamentals and Applications*, John Wiley & Sons, Inc., Hoboken, NJ, USA, 2nd edition, 2001.
- [43] NIST, "CODATA Value: Faraday constant," 2017, <https://physics.nist.gov/cgi-bin/cuu/Value?f>.
- [44] P. Vanýsek, *Electrochemical Series*, in *CRC Handbook of Chemistry and Physics*, J. Rumble, Ed., CRC Press, Boca Raton, FL, USA.
- [45] B. Beverskog and I. Puigdomenech, "Revised Pourbaix diagrams for nickel at 25–300°C," *Corrosion Science*, vol. 39, no. 5, pp. 969–980, 1997.
- [46] C. R. Clayton and Y. C. Lu, "A bipolar model of the passivity of stainless steels—III. The mechanism of MoO<sub>4</sub><sup>2-</sup> formation and incorporation," *Corrosion Science*, vol. 29, no. 7, pp. 881–898, 1989.
- [47] J. R. Hayes, J. J. Gray, A. W. Szmodis, and C. A. Orme, "Influence of chromium and molybdenum on the corrosion of nickel-based alloys," *Corrosion*, vol. 62, no. 6, pp. 491–500, 2006.
- [48] П. Никола́йчук and A. Tyurin, *The Revised Pourbaix Diagram for Molybdenum*, 2014.
- [49] ASTM, *Standard Practice for Calculation of Corrosion Rates and Related Information from Electrochemical Measurements*, ASTM International, West Conshohocken, PA, USA, 2015.
- [50] Y. Hua, R. Barker, and A. Neville, "Comparison of corrosion behaviour for X-65 carbon steel in supercritical CO<sub>2</sub>-saturated water and water-saturated/unsaturated supercritical CO<sub>2</sub>," *Journal of Supercritical Fluids*, vol. 97, pp. 224–237, 2015.
- [51] S. A. McCoy, B. C. Puckett, and E. L. Hibner, "High Performance Age-Hardenable Nickel Alloys Solve Problems in Sour Oil and Gas Service," *Stainless Steel World*, vol. 4, pp. 48–52, 2002.
- [52] NACE International, *Petroleum and Natural Gas Industries—Materials for Use in H<sub>2</sub>S-Containing Environments in Oil and Gas Production*, NACE International, Houston, TX, USA, 2015.

## Research Article

# Synthesis of Copper Oxide Aided by Selective Corrosion in Cu Foils

**Roberto Baca Arroyo** 

*Department of Electronics, National Polytechnic Institute, 07738 Mexico City, Mexico*

Correspondence should be addressed to Roberto Baca Arroyo; [rbaca02006@yahoo.com.mx](mailto:rbaca02006@yahoo.com.mx)

Received 14 August 2017; Revised 5 December 2017; Accepted 31 December 2017; Published 19 February 2018

Academic Editor: Alicia E. Ares

Copyright © 2018 Roberto Baca Arroyo. This is an open access article distributed under the Creative Commons Attribution License, which permits unrestricted use, distribution, and reproduction in any medium, provided the original work is properly cited.

Copper oxide films aided by selective corrosion have been synthesized. Using copper (Cu) foils of commercial printed circuit boards (PCBs), chemical attack in small areas on Cu surfaces and their oxidation with heating process in air atmosphere at low temperature have allowed to produce Cu oxide layers. Phase formation of Cu oxide samples was validated by X-ray diffraction studies, and their conduction properties were registered and evaluated by current-voltage curves. Stability analysis of the Cu oxide samples was conducted by a correlation profile between average strain and Cu oxide percentage grown, which confirms that the structure defects dependent on plastic deformation define the existence of both CuO and Cu<sub>2</sub>O phases beneficial to mitigate corrosion and advance in Cu oxide-based devices to build electronic circuits as components on PCBs.

## 1. Introduction

It is well known that copper (Cu) is a nature-abundant material and is the third metal more employed in the world, after iron and aluminum. It has an important biological role in photosynthesis, and it is essential for human life. Despite the standard negative electrode potential with  $-0.345$  V, its corrosion can occur at a significant rate under strenuous conditions [1]. Both cupric oxide (CuO) and cuprous oxide (Cu<sub>2</sub>O) are the two chemical compounds formed by oxygen and copper in the nature only. Such oxides are semiconductors, where Cu<sub>2</sub>O has a direct bandgap of 2.1 eV and reddish appearance, while CuO with a bandgap of 1.3 eV is black in color [2].

Due to the miniaturization in the integrated circuits (ICs), Cu has been widely used for microelectronic device industry, including wiring technology, electromagnetic interference shielding, and electrostatic dissipation technology [3]. However, the reduced spacing between IC components on a printed circuit board (PCB) can produce various types of corruptions, although the underlying mechanism in all cases has been electrochemical migration (EM) as one of the most severe problems, where events such as temperature

cycles during soldering at temperature above 150°C, degradation of the thermal interface in contacts, existence of dust particles between contacts, and application of high voltage for operation of the electronic devices have made it easy for corrosive environments [4, 5]. The high-temperature corrosion occurs when gradual EM by Cu ions along an interconnection under high current density (current crowding) increases the resistance of the Cu lines with reduction in their cross-sectional area [6]. High-temperature corrosion can be able to assist the oxidation in the Cu lines where their surface will remain safe, and small fluctuations will degrade the oxide in few critical points due to the pit formation under humidity conditions. The interior of a pit is naturally poorer in oxygen, and pH locally decreases to very low values, thus pitting corrosion increase due to the catalytic process where dendrite growth from cathode to anode produces an electric short and premature failure. Figure 1 shows pitting corrosion and dendrite growth on a PCB when high electric field was applied [7].

Previously, studies have shown that for maximizing reliability in IC design and PCB fabrication, width scaling of Cu lines must be investigated by EM phenomena where to reduce failures by corrosion environments, two scenarios

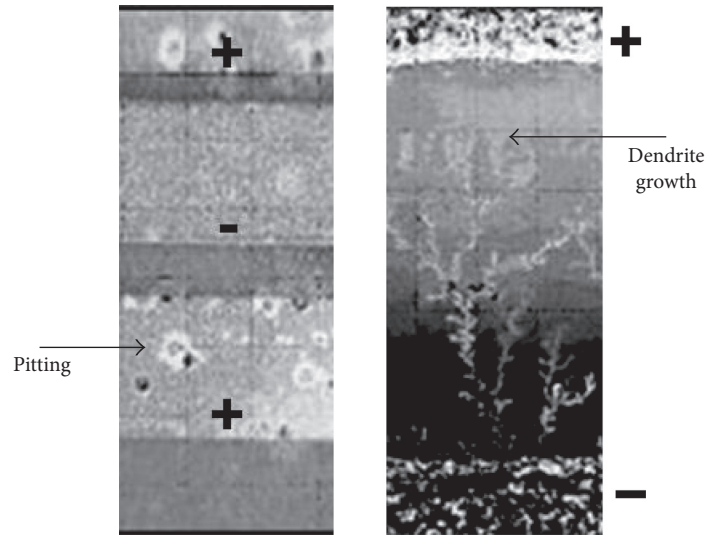


FIGURE 1: Corrosion phenomena on a PCB based on EM under high electric field conditions.

have been recommended with respect to the mechanisms governing the Cu ion migration with the suggested spacing between IC components satisfying a width  $<1\ \mu\text{m}$ , whereas a width  $>1\ \mu\text{m}$  is for components on PCBs [6, 8].

Nowadays, researchers have synthesized p-channel  $\text{Cu}_2\text{O}$  thin-film transistors on flexible polyethylene terephthalate (PET) substrates by using magnetron sputtering and vacuum annealing techniques [9, 10]. Such novel electronic devices provide modest transport properties with hole mobility ( $\mu_h$ ) in the range of 1 to  $10\ \text{cm}^2/\text{Vs}$  and hole concentration ( $n_h$ ) from  $10^{16}$  to  $10^{17}\ \text{cm}^{-3}$ . Its conduction mechanism is attributed to the electronic structure of intrinsic defects such as Cu vacancies [ $V_{\text{Cu}}$ ], which create trap states [11]. Conversely, the operation characteristics of the  $\text{Cu}_2\text{O}$  thin-film transistors are of no use today to engineering applications, and the market for  $\text{Cu}_2\text{O}$ -based devices has been delayed by setback in its scalability, degradation of their electronic properties at high-temperature conditions, and requirements for high quality of  $\text{Cu}_2\text{O}$  with a minimum in structure defects. Consequently, to achieve useful engineering applications using Cu oxide-based devices compatible with silicon technology and controllable operation characteristics, the formation and growth of CuO on the Cu surface can increase the chemical bonding and path of the specific thermal resistance in  $\text{Cu}_2\text{O}$ -based devices for electronic circuits designed as components on PCBs [5]. The layer CuO is accompanied by defects such as dislocations and grain boundaries where reactivity of these is dependent on intrinsic structure disorder (elastic strain effects) [12]. Thus, transformation in the microstructure of the Cu surface (process known as plastic deformation) can be a strategy to adjust defect density and mitigate corrosion issues [3].

In the past, oxidation procedures at high temperature around  $1000^\circ\text{C}$  in air atmosphere have been developed to oxidize Cu foils in order to obtain polycrystalline  $\text{Cu}_2\text{O}$  crystals [11], where Cu oxidation has taken place by diffusion

process of the Cu ions which migrate because there is an opposite diffusion of [ $V_{\text{Cu}}$ ] from oxide layer to the Cu foil [1]. Nevertheless, as CuO is less stable than  $\text{Cu}_2\text{O}$  and its formation energy is lower, the presence of CuO appearing together with  $\text{Cu}_2\text{O}$  can be attained by plastic deformation on the Cu surface at low temperatures [2, 4]. Thereby, the work presents the synthesis of Cu oxide films aided by selective corrosion of Cu foils with the subsequent heating process in air atmosphere at low temperatures. Such experimental procedure will be discussed in Section 2. Phase formation and conduction properties in Cu oxide films and stability analysis as a function of average elastic strain originated by selective corrosion will be covered in Section 3. Conclusions about this research are presented in Section 4.

## 2. Experimental Procedure

Cu foils with an average thickness of  $15\ \mu\text{m}$  were obtained from commercial PCBs with copper joined in a fiberglass epoxy polymer. Before, Cu foils were cut in a cross-sectional area of  $1\ \text{cm}^2$ ; after, cleaning process to remove nonpolar substances was developed with acetone; finally, washing process was completed in deionized water and successively dried with nitrogen. In the synthesis of Cu oxide aided by selective corrosion, the following four stages are involved: (a) choosing the area for chemical attack, (b) immersing Cu foils in  $\text{FeCl}_3/\text{H}_2\text{O}$  solution, (c) removing residual  $\text{FeCl}_3/\text{H}_2\text{O}$  by soaking the chemically attacked Cu foils, and (d) heating the Cu foils in air atmosphere inside of quartz tube furnace. Figure 2 shows the stages in the synthesis to obtain Cu oxide films.

A nontoxic permanent marker typically engaged in the design of PCBs was used to synthesize Cu oxide samples. An area of  $4\ \text{mm} \times 4\ \text{mm}$  was defined on each Cu foil under study. A permanent marker is resistant at  $\text{FeCl}_3/\text{H}_2\text{O}$  solution; therefore, during corrosion, the outside area was protected as shown in Figure 2. Iron chloride ( $\text{FeCl}_3$ ) solution activated with  $\text{H}_2\text{O}$  was employed as the electrolyte.

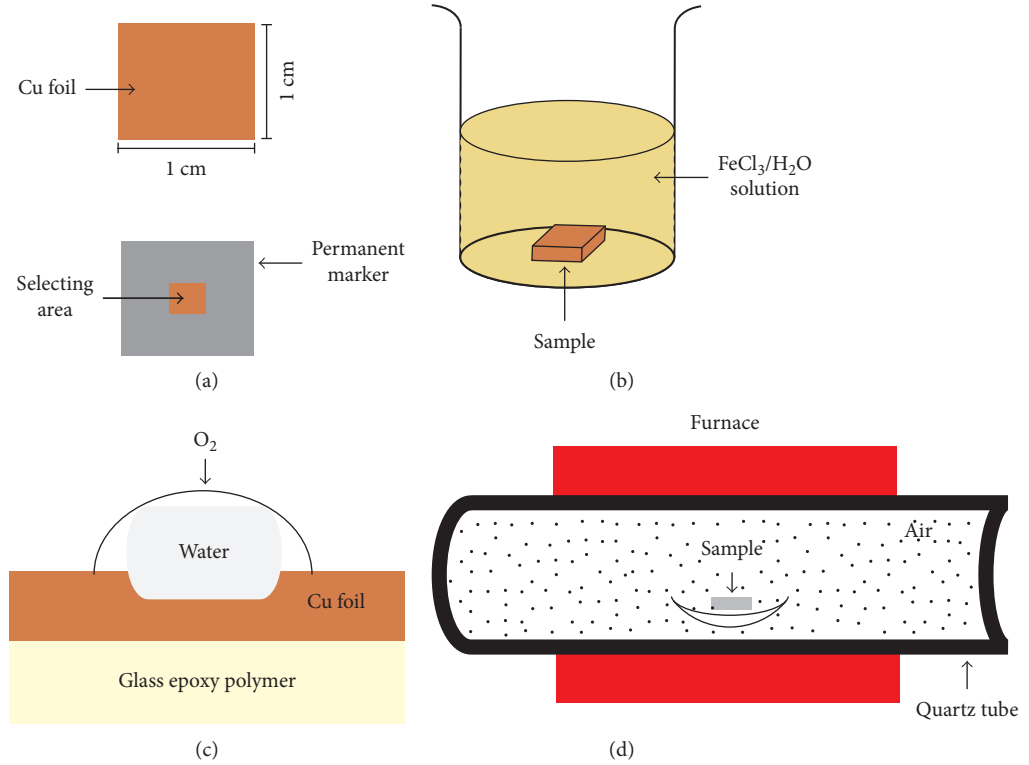
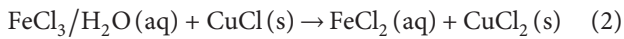
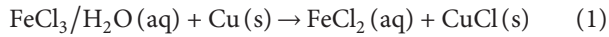


FIGURE 2: Stages employed in the synthesis of Cu oxide films.

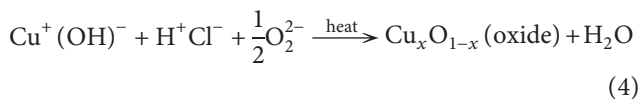
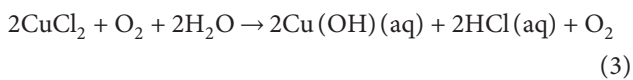
The corrosion behavior by chemical attack was studied at different  $\text{FeCl}_3 : \text{H}_2\text{O}$  rates and immersion times as indicated in Table 1.

The reaction mechanism for Cu corrosion can be written in two stages as



The species dissolved in  $\text{FeCl}_3$  activated with  $\text{H}_2\text{O}$  are  $\text{Fe}^{2+}\text{Cl}_2^-$ ,  $\text{Fe}^+(\text{OH})^-$ , and  $\text{H}^+\text{Cl}^-$  which indicate that corrosion in Cu foils occur because initially  $\text{Cu}^+$  ion in the presence of  $\text{H}^+$  ion produces cupric chloride ( $\text{CuCl}$ ), and later cuprous chloride ( $\text{CuCl}_2$ ) is fully formed by the reaction of  $\text{CuCl}$  with  $\text{Cu}^{2+}$  ion [1, 13, 14].

Once Cu foils were immersed in the  $\text{FeCl}_3/\text{H}_2\text{O}$  solution to obtain  $\text{CuCl}_2$  and soaked with water, heating process at  $35^\circ\text{C}$  with a duration of 2 min at atmospheric pressure was completed. In accordance with the following reaction mechanism, the formation of Cu oxide films took place in two stages:



where  $x$  is the chemical composition in Cu oxide samples.

TABLE 1: Parameters for selective corrosion in Cu foils.

Sample	Volume (mL)		Immersion time (min)
	$\text{FeCl}_3$	$\text{H}_2\text{O}$	
CS-1	5	2.5	2
CS-2	2.5	2.5	4
CS-3	2.5	5	6

The heating temperature for the Cu samples was chosen as a function of the boiling point for HCl of  $48^\circ\text{C}$ , where  $\text{Cl}^-$  ions and residual water are fully evaporated. The surface of Cu oxide samples resulted with opaque gray color after thermal process. The presence of ionic species such as copper hydroxide ( $\text{CuOH}$ ) and acidic chloride ( $\text{HCl}$ ) determines the oxidation degree of the  $\text{CuCl}_2$  surfaces because displacement interactions between  $\text{OH}^-$  and  $\text{H}^+$  ions initially synthesize  $\text{CuO}$  by surface migration of such ionic species and after  $\text{Cu}_2\text{O}$  by diffusion of  $\text{Cu}^+$  ions and reaction with atmospheric oxygen [3, 14]. Nevertheless, as the activity of these species is poorer under heating process within humidity, the Cu oxide films were nonstoichiometric.

Using X-ray diffraction with PANalytical diffractometer of  $\text{CuK}\alpha$  radiation ( $\lambda = 0.1541 \text{ nm}$ ), phase formation of Cu oxide films was validated. Conduction behavior in the samples was registered and evaluated by current-voltage curves at room temperature. The electrical parameters of the samples were collected by employing a digital storage oscilloscope (Tektronix, TDS1012C). To know the performance of the Cu oxide samples as a function of structure

defects involved, a stability analysis was done by a correlation profile between elastic strain and Cu oxide percentage.

### 3. Results and Discussion

This section discusses phase formation and conduction properties in the Cu oxide samples. Here are the revised XRD patterns and electrical characterization to demonstrate the potential of the selective corrosion technique with emphasis in the oxidation degree of the Cu foils dependent on their plastic deformation.

**3.1. X-Ray Diffraction in Cu Oxide Samples.** Figure 3 shows XRD patterns of Cu oxide films synthesized with the heating process. The samples labeled as CS-1, CS-2, and CS-3 exhibit monoclinic phase (CuO) with peaks located at  $33.9^\circ$  and plane (110),  $58.1^\circ$  and plane (202), and  $65.2^\circ$  and plane (022) according to PANalytical Card number 00-041-0254. Also, peak positioned at  $69.7^\circ$  and plane (310) corresponds to cubic phase (Cu<sub>2</sub>O) according to PANalytical Card number 00-005-0667. As a reference, the XRD pattern of Cu foil also is shown. The larger peak-position displacement between XRD patterns of the Cu oxide films and XRD pattern of the Cu foil was observed which ensures presence of the elastic strain in Cu oxide surface induced by high density of the defects in chemically attacked Cu foils.

**3.2. Conduction Properties in Cu Oxide Samples.** The performance of Cu oxide samples has been confirmed with the schematic diagram of Figure 4(a). To ensure linear response, a function generator (Matrix, MFG-8250A) was used to produce a linear ramp signal at low frequency ( $f=100$  Hz) with voltage ranging from  $-2$  V to  $2$  V to conserve low-voltage operation across the aluminum (Al) contacts. Also, a resistor of  $R=1$  k $\Omega$  was chosen to monitor the current signal. The log current-voltage plots for samples labeled as CS-1, CS-2, and CS-3 are shown in Figure 4(b), where such current-voltage curves have shown ohmic behavior.

To investigate conduction parameters, a model based on the point form of Ohm's law [15] has been proposed by

$$\frac{\Delta V}{\Delta I} = \frac{l_c}{\sigma_o \exp(-E_a/k_B T)} \cdot S \quad (5)$$

where  $\sigma_o = 5.8 \times 10^5 \Omega^{-1} \text{cm}^{-1}$  is the Cu conductivity at room temperature,  $E_a$  is the activation energy of Cu oxide,  $k_B$  is the Boltzmann constant,  $T$  is the temperature in samples under test,  $l_c = 0.77$  nm is the interatomic distance into CuO crystalline lattice associated with minimal free path of charge carriers [16], and  $S$  is the cross-sectional area ( $S = t \cdot d$ ), where  $d = 0.5$  mm is the diameter of aluminum (Al) contact and  $t$  the thickness of the samples.

The  $\Delta V/\Delta I$  rate was extracted from Figure 4(b), with  $\Delta V$  as the differential voltage and  $\Delta I$  as the differential current, respectively, while  $E_a$  was estimated with the slope of the dotted line in Figure 4(b) which crosses at the voltage axis. Using MATLAB program, the cross-sectional area  $S = t \cdot d$  is computed by solving (5) and by the Arrhenius conductivity dependent on temperature [17].  $[V_{Cu}]$  was estimated by

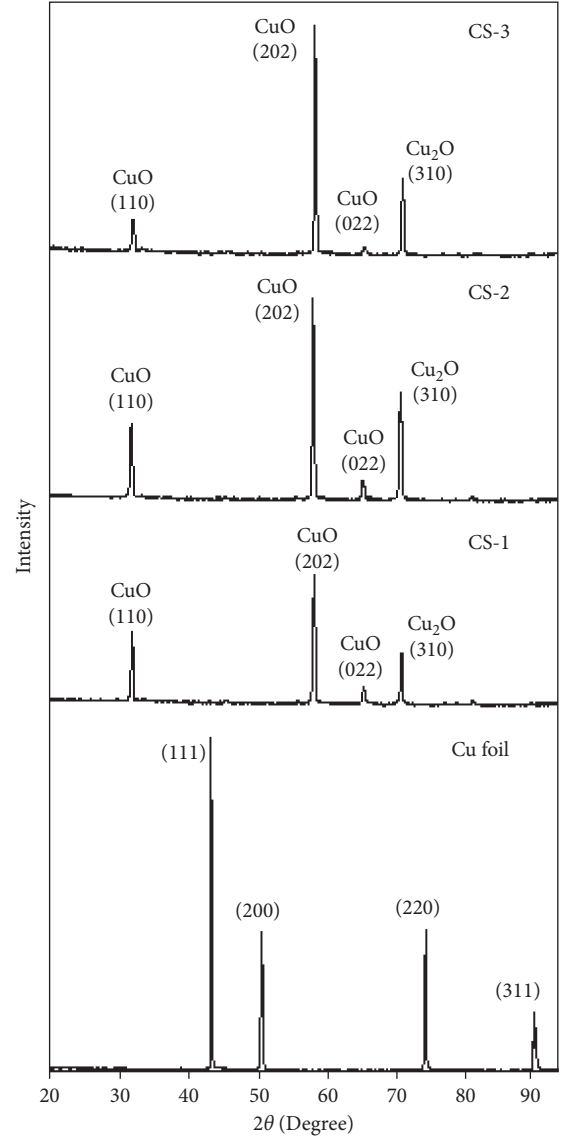


FIGURE 3: XRD patterns in Cu oxide films grown on Cu foils.

$$[V_{Cu}] \cdot e \cdot \mu_{Cu} = \sigma_o \exp\left(-\frac{E_a}{k_B T}\right), \quad (6)$$

where  $\sigma_s(E_a) = [V_{Cu}] \cdot e \cdot \mu_{Cu}$  is the conductivity for the Cu oxide layer, while  $\mu_{Cu}$  corresponds to the mobility of Cu vacancies. The quantity  $[V_{Cu}]\mu_{Cu}$  from (6) was computed, confirming that  $[V_{Cu}]$  is attained in the range of  $10^{14}$  to  $10^{15} \text{cm}^{-3}$  and mobility from 1 to 40  $\text{cm}^2/\text{Vs}$ , which confirms that the operation characteristics in Cu oxide samples would be useful in engineering applications because their specific thermal resistance chemically controlled by CuO and electronic properties driven by Cu<sub>2</sub>O allow advances in design of Cu oxide-based devices whose principle of operation similarly to previous studies by other authors is dependent on strain effects [18, 19]. Table 2 summarizes the conduction parameters found.

**3.3. Stability in Cu Oxide Samples.** To evaluate the performance of the Cu oxide samples as a function of the plastic

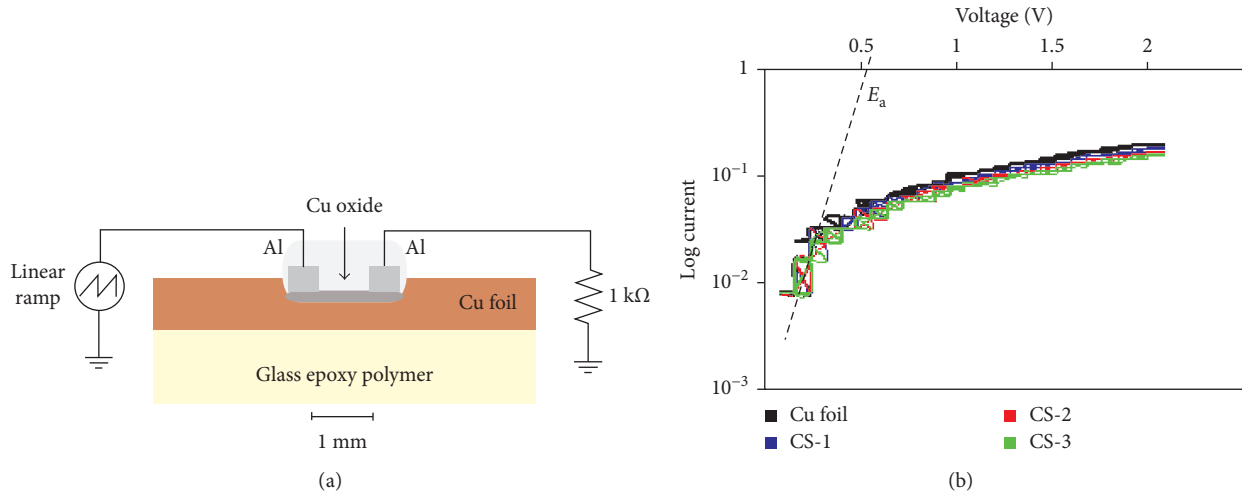


FIGURE 4: (a) Schematic diagram of practical circuit implemented to measure the current-voltage curves in Cu oxide samples. (b) Log current-voltage plots of each sample.

TABLE 2: Conduction parameters in Cu oxide samples.

Sample	$E_a$ (eV)	$\Delta V/\Delta I$ ( $\Omega$ )	$\sigma_s(E_a) \cdot (\Omega^{-1} \cdot \text{cm}^{-1})$	$t$ (nm)	$\mu \cdot [V_{\text{Cu}}] \cdot (\text{cm}^{-1} \cdot \text{V}^{-1} \cdot \text{s}^{-1})$
CS-1	0.54	130.43	$5.55 \times 10^{-4}$	212.1	$3.5 \times 10^{15}$
CS-2	0.56	190.47	$2.57 \times 10^{-4}$	314.6	$1.6 \times 10^{15}$
CS-3	0.56	315.78	$2.57 \times 10^{-4}$	189.7	$1.6 \times 10^{15}$

deformation in Cu foils, average strain along each crystallographic plane on the oxidized Cu surface with respect to the Cu foil as substrate is approximately estimated by  $(\Delta d/d) = \Delta\theta / \tan\phi$  [12], where  $\Delta\theta$  is the difference between measured incident angle  $\theta_m$  and reference angle  $\theta_r$ , while the angle of each Cu foil plane corresponds to  $\phi$ . The parameter ( $x \approx \Delta d/d$ ) can be linked with the chemical composition in  $\text{Cu}_x\text{O}_{1-x}$  which defines its nonstoichiometry [20].

The elastic strain must be analyzed as a function of Cu oxide grown, being it proportional to the intensity in percentage of each peak [12, 20]. Figure 3 allows evaluating  $\Delta\theta$  at each crystallographic plane of both oxides ( $\text{Cu}_2\text{O}$  and  $\text{CuO}$ ), as well as  $\tan\phi$  at each crystallographic plane in the Cu foil; thus, a correlation profile between  $x$  and Cu oxide percentage is built in Figure 5.

The structure defects can be validated by stability analysis, which determines the ability of the Cu oxide layers to remain structurally stable during electrical conduction. The stability in the Cu oxide samples is a function of both tensile and compressive stress into a limit where Cu oxide ( $\text{Cu}_x\text{O}_{1-x}$ ) is fully grown into two phases. In Figure 5, both oxides ( $\text{Cu}_2\text{O}$  and  $\text{CuO}$ ) give a slight deviation from their nonstoichiometry into the range of  $-1 < x < 1$ , which corresponds to the limit where the Cu oxide percentage from 30 to 100% is stable. In contrast, anomalous Cu oxide is lower than 30%, because its severe nonstoichiometry is associated with intergranular local attack influenced by poor quality of the initial Cu surface.

Selective corrosion followed with the heating process at 35°C had allowed obtaining both  $\text{Cu}_2\text{O}$  and  $\text{CuO}$  phases in

accordance with the experimental procedure detailed in Section 2, where oxidation in Cu foils occurs beginning with a first layer of  $\text{CuO}$  grown on Cu, and subsequently a layer of  $\text{Cu}_2\text{O}$  grows between Cu and  $\text{CuO}$ . These two layers increase with time because the  $\text{Cu}_2\text{O}$  has a very small expansion coefficient at lower temperatures of 300°C where the lattice constant changes to less than 0.5% and the dissociation pressure of  $\text{CuO}$  is lower than the atmospheric pressure [11, 13]. As Cu vacancies agglomeration or trapped oxygen happen into grain boundaries, intrinsic concentration of defects corresponding with  $[V_{\text{Cu}}]$  and the opaque gray color in Cu oxide samples explicate the stability of the  $\text{CuO}$  phase.

## 4. Conclusions

Cu oxide samples synthesized by corrosion and heating processes at low temperature have been studied. Selective corrosion was achieved by chemical attack in smaller areas from Cu foils of commercial PCBs. Both  $\text{CuO}$  and  $\text{Cu}_2\text{O}$  phases were formed under air atmosphere. The study conducted by X-ray diffraction and electrical characterization found that phase formation and conduction properties are linked with structure defects into Cu foils. Stability analysis has confirmed that the structure behavior in Cu oxide samples is strongly dependent on its intrinsic disorder. Thus, the selective corrosion technique has significant benefits as physical and mechanical properties are influenced by plastic deformation, which has resulted in stable Cu oxide samples with next electronic engineering applications for Cu oxide-based devices.

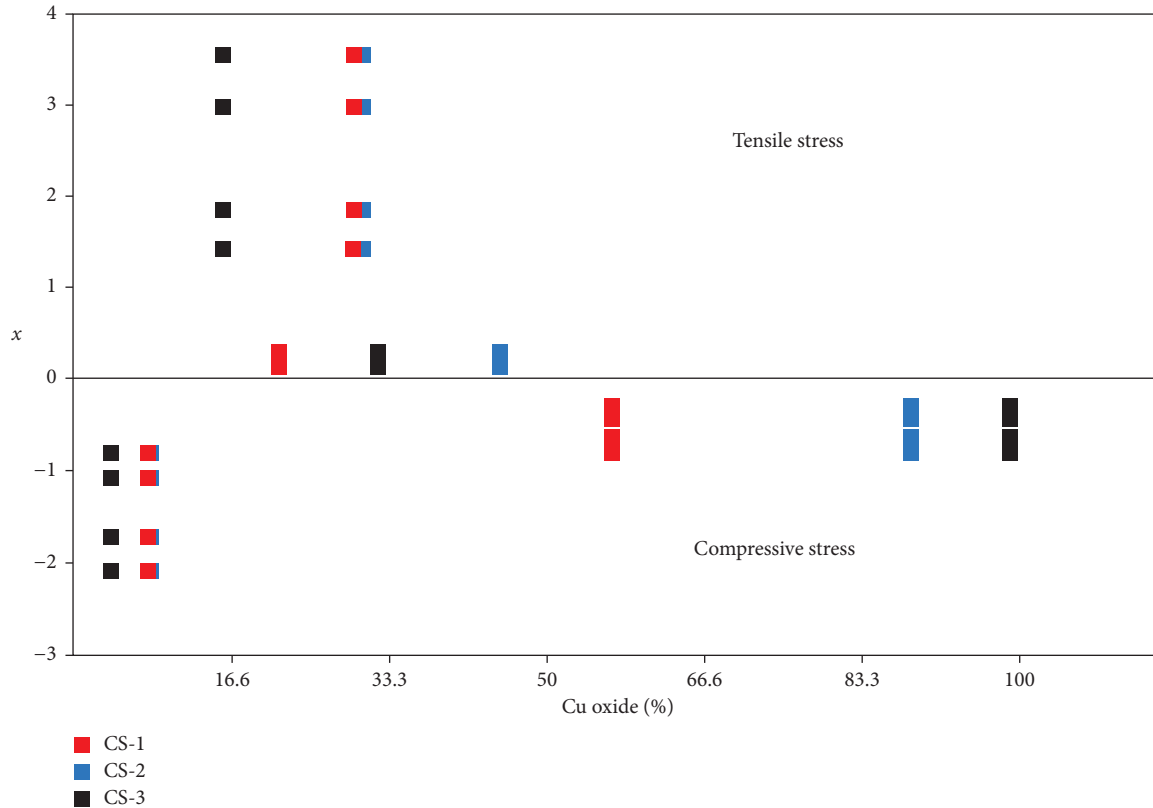


FIGURE 5: Correlation profile for different Cu oxide samples.

## Conflicts of Interest

The author declares that there are no conflicts of interest, but there is an interest regarding the publication of this manuscript to share knowledge about green material processing and their applications.

## Acknowledgments

The structural data collected from XRD studies have been supported thanks to Dr. José Alberto Andraca Adame from CNMN belonging at the National Polytechnic Institute, Mexico City, Mexico.

## References

- [1] A. C. Keyser, *Materials Science in Engineering*, Prentice Hall, Inc., México City, Mexico, 6th edition, 1990.
- [2] L. Y. Isseroff and E. A. Carter, "Electronic structure of pure and doped cuprous oxide with copper vacancies: suppression of trap states," *Chemistry of Materials*, vol. 25, no. 3, pp. 253–265, 2013.
- [3] W. Deng, P. Lin, Q. Li, and G. Mo, "Ultrafine-grained copper produced by machining and its unusual electrochemical corrosion resistance in acidic chloride pickling solutions," *Corrosion Science*, vol. 74, pp. 44–49, 2013.
- [4] J.-M. Song, D.-S. Wang, C.-H. Yeh, W.-C. Lu, Y.-S. Tsou, and S.-C. Lin, "Texture and temperature dependence on the mechanical characteristics of copper electrodeposits," *Materials Science and Engineering A*, vol. 559, pp. 625–644, 2013.
- [5] R. Skuriat, J. F. Li, P. A. Agyakwa, N. Matthey, P. Evans, and C. M. Johnson, "Degradation of thermal interface materials for high-temperature power electronics applications," *Microelectronics Reliability*, vol. 53, no. 12, pp. 1933–1942, 2013.
- [6] Md. K. Rahman, A. M. M. Musa, B. Neher, K. A. Patwary, M. A. Rahman, and Md. S. Islam, "A review of the study on the electromigration and power electronics," *Journal of Electronics Cooling and Thermal Control*, vol. 6, no. 1, pp. 19–31, 2016.
- [7] G. S. Frankel, *Corrosion Mechanisms in Theory and Practice*, Marcel Dekker, New York, NY, USA, 1995.
- [8] M. H. Lin, K. P. Chang, K. C. Su, and T. Wang, "Effects of width scaling and layout variation on dual damascene copper interconnect electromigration," *Microelectronics Reliability*, vol. 47, no. 12, pp. 2100–2108, 2007.
- [9] Z. Q. Yao, S. L. Liu, L. Zhang et al., "Room temperature fabrication of p-channel  $\text{Cu}_2\text{O}$  thin-film transistors on flexible polyethylene terephthalate substrates," *Applied Physics Letters*, vol. 101, no. 4, p. 042114, 2012.
- [10] J. Yu, G. Liu, A. Liu, Y. Meng, B. Shin, and F. Shan, "Solution-processed p-type copper oxide thin-film transistors fabricated by using a one-step vacuum annealing technique," *Journal of Materials Chemistry C*, vol. 3, no. 37, pp. 9509–9513, 2015.
- [11] N. Cabrera and N. F. Mott, "Theory of the oxidation of metals," *Reports on Progress in Physics*, vol. 12, no. 1, pp. 163–184, 1949.
- [12] P. F. Fewster, *X-Ray Scattering from Semiconductors*, Imperial College Press, Singapore, 2nd edition, 2003.
- [13] A. Cotton and G. Wilkinson, *Advanced Inorganic Chemistry*, John Wiley & Sons, New York, NY, USA, 4th edition, 2008.
- [14] M. Ottosson, M. Boman, P. Berastegui et al., "Copper in ultrapure water, a scientific issue under debate," *Corrosion Science*, vol. 122, pp. 53–60, 2017.

- [15] A. S. Grove, *Physics and Technology of Semiconductor Devices*, John Wiley & Sons, New York, NY, USA, 1st edition, 1967.
- [16] M. Lundstrom, *Fundamentals of Carrier Transport*, Cambridge University Press, New York, NY, USA, 2nd edition, 2000.
- [17] J. J. O'Dwyer, *The Theory of Electrical Conduction and Breakdown in Solid Dielectrics*, Clarendon Press, Oxford, UK, 1st edition, 1973.
- [18] R. K. Zheng, C. Chao, H. L. W. Chan, C. L. Choy, and H. S. Luo, "Converse piezoelectric control of the lattice strain and resistance in  $\text{Pr}_{0.5}\text{Ca}_{0.5}\text{MnO}_3/\text{PMN-PT}$  structures," *Physical Review B*, vol. 75, no. 2, p. 024110, 2007.
- [19] V. P. Malinenko, L. A. Aleshina, A. L. Pergament, and G. V. Germak, "Switching Effects and Metal-Insulator Transition in Manganese Oxide," *Journal on Selected Topics in Nano Electronics and Computing*, vol. 1, no. 1, pp. 44–50, 2013.
- [20] R. Baca-Arroyo, "Structural characterization of the chromium-iron alloy formed by thermal diffusion processes," *Advanced Materials Research*, vol. 651, pp. 284–288, 2013.

## Research Article

# Effects of Alloying Elements (Cr, Mn) on Corrosion Properties of the High-Strength Steel in 3.5% NaCl Solution

Bomi Kim <sup>1</sup>, Soojin Kim <sup>2</sup>, and Heesan Kim <sup>1</sup>

<sup>1</sup>Department of Materials Science and Engineering, Hongik University, 2639 Sejong-ro, Jochiwon-eup, Sejong 339-701, Republic of Korea

<sup>2</sup>University of Alabama School of Medicine, 510 20th St. S., Birmingham, AL 35210, USA

Correspondence should be addressed to Heesan Kim; [heesan1118@gmail.com](mailto:heesan1118@gmail.com)

Received 30 August 2017; Revised 23 October 2017; Accepted 31 October 2017; Published 15 February 2018

Academic Editor: María V. Biezma

Copyright © 2018 Bomi Kim et al. This is an open access article distributed under the Creative Commons Attribution License, which permits unrestricted use, distribution, and reproduction in any medium, provided the original work is properly cited.

Effects of chromium and manganese as alloying elements on corrosion resistance of carbon steel were examined using evaluation of corrosion resistance in 60°C NaCl solution with a weight loss test, polarization test, analysis of rust with X-ray diffractometer, Raman spectroscopy, transmission electron microscopy, energy dispersive spectroscopy, and electron energy loss spectroscopy. The weight loss behavior conformed to a typical parabolic law, and the oxidation state of iron in rust was higher along the fast pathway but was disproportionate to the distance from the alloy/AR interface. It suggests that the corrosion process of the alloys was controlled by transport of oxygen to the rust layer. The improvements in corrosion resistance of 18Mn and 18Mn5Cr resulted from both the refinement of grain in adherent rust (AR) and the increase of the amounts of goethite in nonadherent rust (NAR) by chromium and manganese. Especially, the effectiveness of chromium on corrosion resistance was also related to the refinements of grain in AR and the amounts of goethite in NAR. The Tafel extrapolation method was inadequate to measure the instantaneous corrosion rate of steels with various alloying elements and immersion periods because of the difference in electrochemical reduction rates of rust, depending on its constituent.

## 1. Introduction

High manganese steels with high strength and toughness were developed to satiate the need for a material with superb physical properties in response to energy crisis and carbon dioxide release restriction [1]. However, even recently, relevant studies on the effects of manganese on corrosion resistance of steel have been comparatively minimal [2–5]. Particularly, the effects of manganese on corrosion resistance of steel during the exposure to chloride-containing environments have been reported inconsistently [4, 6–12].

In a previous study, Melchers [13, 14] proposed a model on the corrosion process of carbon steel. Before microbiological-induced corrosion (MIC) or pitting corrosion does not occur, the model consists of two stages depending on the rate-determining step: reactions on its metal surface for the first stage and diffusion of oxygen through rust for the second stage. Because the model remains in the second stage for the most of the total exposure period,

we believe that corrosion resistance of carbon steels during a long-term exposure greatly depends on the rust as it serves as a medium for oxygen penetration. The long-term exposure test has shown that the corrosion rates for the rust components are less than 0.01 mm/yr, as shown in (1) [15, 16]:

$$\frac{\alpha}{\gamma^*} > 1, \quad (1)$$
$$\text{or } \frac{s + \beta}{\gamma^*} < 0.5,$$

where  $\alpha$ ,  $s$ ,  $\gamma$ , and  $\beta$  are the mass concentrations of goethite, spinel oxide, lepidocrocite, and akaganeite, respectively, and  $\gamma^*$  is the total of  $s$ ,  $\gamma$ , and  $\beta$ . The first equation demonstrates the effect of the amount of ultrafine-grained goethite on the rust protectiveness. The second equation illustrates the penetration of corrosive species through the defects in akaganeite and spinel oxide [15, 17, 18].

TABLE 1: Chemical composition of the experimental alloys.

Name	Phase(s)	Chemical composition (% wt.)				
		C	Mn	Cr	Ni	Fe
REF(API60)	$\alpha$ + bainite	0.067	1.6	0.02	0.2	Balance
18Mn	$\gamma$	0.6	18.4	<0.005	<0.005	Balance
18Mn5Cr	$\gamma$	0.6	18.5	5.1	<0.005	Balance

In general, the transport of oxygen through rust depends on its grain size, crystal structure, chemical stability, and porosity [19–24], which explains the dependency of corrosion resistance on iron oxide or oxyhydroxide. According to the Melchers model, during the initial state of the first stage, steels are oxidized to produce various forms of dissolved ferrous ion or precipitated ferrous hydroxide. The various forms of ferrous ion are chemically or electrochemically oxidized by oxygen to produce different types of ferric oxyhydroxide, maghemite, or hematite. With the elapsed time, the thickened rust layer impedes the transport of oxygen to the steel surface. During this period, various forms of ferric oxyhydroxide may reduce to magnetite [25, 26]: incorporation of ferrous ion into ferric oxyhydroxide [27], slow oxidation of ferrous hydroxide via green rust (GR) [28], or reaction of the dissolved ferric oxyhydroxide with dissolved ferrous hydroxide [29, 30]. The first process occurs in rust, and the other processes occur at the rust/solution interface or at rust near the solution. As an alloying element, manganese not only impedes the formation of magnetite [31, 32] but also encourages the formation of refined goethite. Chromium hinders magnetite’s nucleation [33] and growth [34], while it promotes the nucleation [33] and growth [35] of goethite and refinement of grain [36]. Both manganese and chromium improve corrosion resistance of steel; however, chromium has a greater effect than manganese [36].

The effects of manganese and chromium on corrosion resistance [37] of high manganese steels were studied by examining rust properties with X-ray diffraction (XRD), Raman spectroscopy, energy dispersive spectroscopy (EDS) [4, 5], and electron energy loss spectroscopy (EELS) adjunct to transmission electron microscopy (TEM).

## 2. Experimental Procedure

**2.1. Preparation of Specimen.** The ingots (API60, 18Mn, and 18Mn5Cr) with chemical compositions listed in Table 1 were cast to examine the effects of corrosion resistance of carbon steel on manganese and chromium. API60 was used as a reference material and hereafter named “REF”. 25 kg ingots were heat treated at 1150°C for 1.5 hours under an argon atmosphere and hot rolled to 4.5 mm. Both surfaces of the plate were mill-machined to 3 mm thickness in order to remove the scale formed during the heat treatment. Then, the 3 mm thick plates were cut into 2 cm × 1 cm × 0.4 cm coupons for an immersion test and 1 cm × 1 cm × 0.4 cm coupons for a polarization test, respectively. All the surfaces were wet grounded with successive grade silicon carbide papers, from 200 to 600 grit, degreased with acetone, rinsed with ethanol, blow-dried, and finally kept in a desiccator.

**2.2. Evaluation of Corrosion Resistance.** The weight loss test and polarization test were conducted to evaluate corrosion resistance of the experimental alloys. The tests were carried in 3.5% NaCl aqueous solution at a constant temperature of 60°C. During the immersion test, the coupons were supported on cradles—a glass cradle with protrusions—to minimize the cradle-couple contact area. In each capped vessel, each coupon was immersed in 200 mL of 3.5% NaCl solution. Immersion periods were 1, 7, 14, 28, and 56 days for REF, 18Mn, and 18Mn5Cr, respectively. On every 7th day, the solution was replaced with a fresh solution to maintain the pH of the solution within 0.2. For the weight loss measurements, the rust formed on the coupon was removed, and the exposed coupon was immersed in a hydrochloric acid inhibited with hexamethylenetetramine (0.025 M C<sub>6</sub>H<sub>12</sub>N<sub>4</sub> + 5.43 M HCl) at room temperature in an ultrasonic bath for 5–10 minutes, according to ASTM G1 [38]. The weight measurement results were used to calculate the weight at an immersion time and mean weight loss rate as shown in

$$\text{Mean weight loss rate } (t_i) = \frac{\Delta W(t_i) - \Delta W(t_{i-1})}{t_i - t_{i-1}}, \quad (2)$$

where  $\Delta W(t_i)$  is the weight loss per surficial area at immersion time  $t_i$ .

The immersion test was repeated twice under the same condition for reproducibility. If the results showed high deviations, the immersion test was repeated until credible/reliable data were obtained.

The cathodic polarization test was conducted to measure instantaneous corrosion rates ( $i_{\text{corr}}$ ) [39], and the anodic polarization test was performed to observe corrosion behaviors. To prepare a working electrode, the square coupons were embedded in epoxy resin [37] with an exposure area of 1 cm<sup>2</sup>, wet grounded with 600 grit silicon carbide papers, rinsed with ethanol, dried, and stored in a desiccator. A saturated calomel electrode (SCE) and a platinum mesh were used as a reference electrode and a counter electrode, respectively. The mounted coupons, from 1-day and 56-day immersion in the chloride solution, were anodically or cathodically polarized by a corrosion potential at the scan rate of 20 mV/min. By linearly fitting the polarization curves around the potentials by 100 mV lower than corrosion potentials, cathodic Tafel slopes ( $\beta_c$ ) were obtained as well as instantaneous corrosion rates.

**2.3. Analysis of Rust.** At the end of 56-day immersion, the coupons with their vessels were placed in the ultrasonic bath for 15–20 seconds to remove nonadherent rusts (NARs), and then, the coupons were extracted. The NARs were filtrated,

TABLE 2: Summaries on the commercial companies and synthetic methods of iron oxides used for the standard Raman spectra.

Iron oxide	Source	Remarks
Magnetite	High Purity Chemicals	Powder, <1 $\mu\text{m}$ , >99%
Maghemite ( $\gamma\text{-Fe}_2\text{O}_3$ )	[22]	Powder
Hematite ( $\alpha\text{-Fe}_2\text{O}_3$ )	High Purity Chemicals	Powder, <1 $\mu\text{m}$ , >99%
Goethite ( $\alpha\text{-FeOOH}$ )	Rare Metallic Co. Ltd.	Powder, >99%
Akaganeite ( $\beta\text{-FeOOH}$ )	[22]	Powder
Lepidocrocite ( $\gamma\text{-FeOOH}$ )	High Purity Chemicals	Powder, >99%

TABLE 3: Summary on the peaks observed from the Raman spectra of standard samples of iron rust.

Standard sample	Peak positions/cm <sup>-1</sup> (relative intensity)					Remarks
	1st	2nd	3rd	4th	5th	
Magnetite	286 (100)	396 (54)	222 (50)	640 (41)*	475 (22)	*Wide
Maghemite ( $\gamma\text{-Fe}_2\text{O}_3$ )	286 (100)	396 (54)	222 (50)	640 (41)*	475 (22)	*Wide; peak at 710
Hematite ( $\alpha\text{-Fe}_2\text{O}_3$ )	292 (100)	224 (54)	410 (44)	612 (24)	494 (11)	—
Goethite ( $\alpha\text{-FeOOH}$ )	386 (100)	301 (29)	548 (17)	482 (16)	245 (13)	—
Akaganeite ( $\beta\text{-FeOOH}$ )	390 (100)*	310 (87)*	495 (26)	540 (22)	—	*Wide
Lepidocrocite ( $\gamma\text{-FeOOH}$ )	250 (100)	378 (57)	530 (55)	347 (43)	308 (23)	—

washed with distilled water to remove chloride, and dried at 50°C in an oven for 1 hour. Later, all the rusts were grounded into a homogeneous powder mixture. The extracted coupons were also washed and dried with the same procedure as the NARs in order to analyze all the adherent rusts (ARs) which were still intact with the coupons after the ultrasonic bath. X-ray diffraction and Raman spectroscopy were performed to analyze NARs, while XRD, TEM-EDS, and EELS were conducted to analyze ARs.

The XRD measurements of the NARs were performed on a diffractometer (Digaku D/max-3A model) equipped with Cu ( $K\alpha$ ) for both qualitative and quantitative analyses. The scans were done in the range of  $2\theta$  between 10° and 90° at a rate of 2 degrees/min. For the qualitative analysis, 85% of the entire NARs and the reference oxides listed in Table 2 were mixed with 15% of zinc oxide. Among the reference samples in Table 2, magnetite, hematite, goethite, and lepidocrocite were purchased and the others were synthesized [22]. For quantitative analysis, zinc oxide was mixed to serve as a reference intensity. Then, to quantitatively analyze the NARs, 85% of several mixtures of the known amounts of oxides listed in Table 2 were mixed with 15% of zinc oxide, following the internal standard method [40]. From the XRD measurements, the intensities of iron oxides were expressed as a function of concentration. In terms of the qualitative analysis of the ARs, XRD measurement was performed under the same conditions as mentioned above. Two modes were used to show phase distributions along the depth direction, where one is a normal mode and the other is a thin film mode. In the thin film mode, the glance angle was fixed to 1°. The coupons on which ARs were formed were used without an additional preparation for XRD measurements.

The Raman spectra of pellets made from the powder were measured in a Raman II-Senterra (Bruker). It was

configured with a microscope of 50x magnification. The Raman spectroscopy was excited using a laser (785.0 nm) with a nominal maximum output power of 1 mW for 20 seconds to avoid any internal structure modification of the samples. The Raman spectra of the iron oxides listed in Table 2 were measured and summarized in Table 3 to qualitatively analyze the NARs.

The ARs were analyzed by scanning transmission electron microscopy (STEM, JEM-ARM200F), and their compositions, grain sizes, crystal structures, and oxidation states within 1  $\mu\text{m}$  far away from an interface between the alloy and the AR were examined. With the thinned sample prepared by a focused ion beam (FIB), AR chemical composition was analyzed by energy X-ray dispersive spectroscopy (EDS); the crystal structure and grain size were analyzed by selected area electron diffraction (SAED); and the oxidation state of iron was analyzed by electron energy loss spectroscopy (EELS) according to (3) [41]:

$$\text{Oxidation state of iron} \propto \frac{I. \text{ of Fe } L_3}{I. \text{ of Fe } L_2}, \quad (3)$$

where  $I. \text{ of Fe } L_i$  is the integral intensity of the Fe  $L_i$  edge peak.

### 3. Results

**3.1. Effect of Alloying Elements on Corrosion Resistance.** Figure 1 provides both weight loss and mean weight loss rate with immersion time of all the experimental alloys in 3.5% NaCl solution at 60°C. In all the alloys, weight loss increased with immersion time but the mean weight loss rate decreased, which is referred as a typical parabolic behavior hereafter. In addition, chromium and manganese, as alloying elements, showed reduced mean weight loss rates

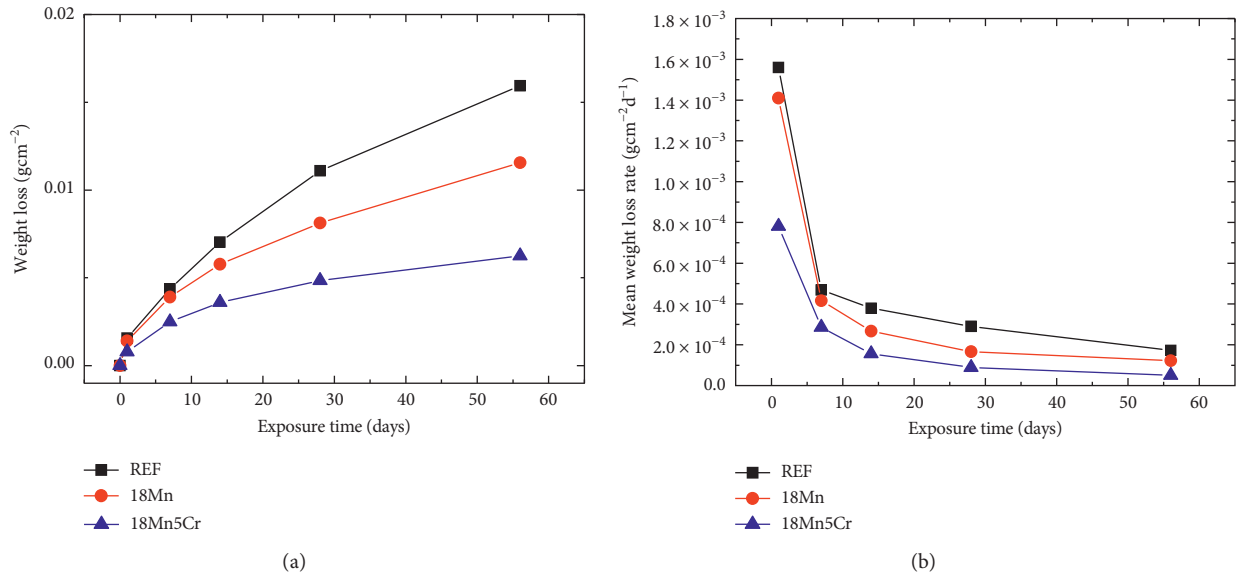


FIGURE 1: Weight loss versus time curves (a) and average weight loss rate versus time curves (b) of experimental alloys immersed in 3.5% NaCl solution at 60°C.

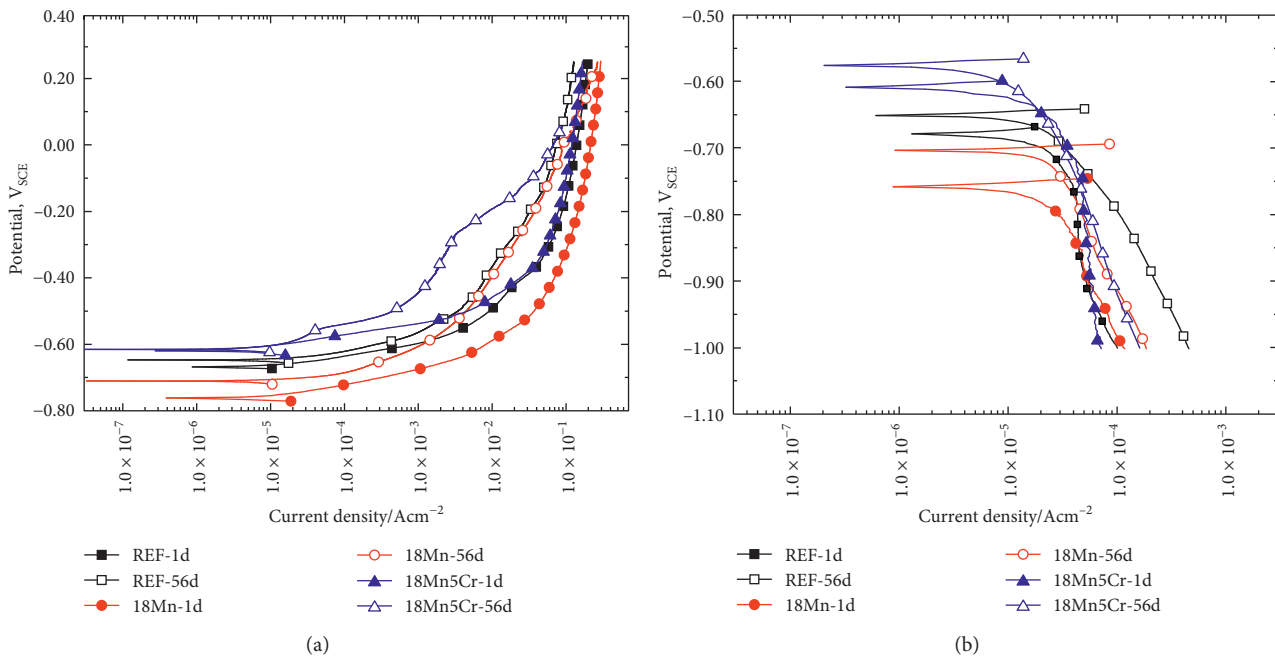


FIGURE 2: Anodic (a) and cathodic (b) polarization curves of experimental alloys in 3.5% NaCl solution at 60°C.

during the immersion period, while chromium improved corrosion resistance.

The anodic polarization curves in Figure 2(a) and corrosion potentials in Table 4 show that corrosion potentials were ennobled with immersion, and anodic current densities at the range of potential between corrosion potentials and  $-0.1 V_{\text{SCE}}$  were reduced with immersion time. These results indicate that the decreased corrosion rate with immersion period in Table 4 is caused by the formation of rust, resulting in the change of anodic current density. In addition, the ratio of anodic currents at two different immersion periods

(1 day and 56 days) was reduced in the following order:  $18\text{Mn5Cr} > 18\text{Mn} > \text{REF}$ , which corresponds with the change of the mean weight loss rate shown in Figure 1(b). Hence, the results on the immersion test and polarization test suggest that both chromium and manganese aid to form more protective rust and retard the penetration of corrosive species such as oxygen [36] into the rust layer—a controlling step for corrosion. Furthermore, the result corresponds to the corrosion mechanism proposed by Melchers [13] that, during the second stage, the corrosion rate of carbon steel is controlled by the migration rate of corrosive species through

TABLE 4: Summaries on corrosion potentials, Tafel slopes, and corrosion rates of the experimental alloys from analysis of cathodic polarization curves in Figure 2(b).

Alloys	Immersion time					
	1 day			56 days		
	Corros. pot. ( $V_{SCE}$ )	Tafel slope ( $\beta_c$ )	$i_{corr}$ ( $\mu A/cm^2$ )	Corros. pot. ( $V_{SCE}$ )	Tafel slope ( $\beta_c$ )	$i_{corr}$ ( $\mu A/cm^2$ )
REF	-0.679	-0.557	27.8	-0.652	-0.209	25.1
18Mn	-0.758	-0.557	29.5	-0.704	-0.511	31.6
18Mn5Cr	-0.608	-0.288	16.2	-0.577	-0.345	13.4

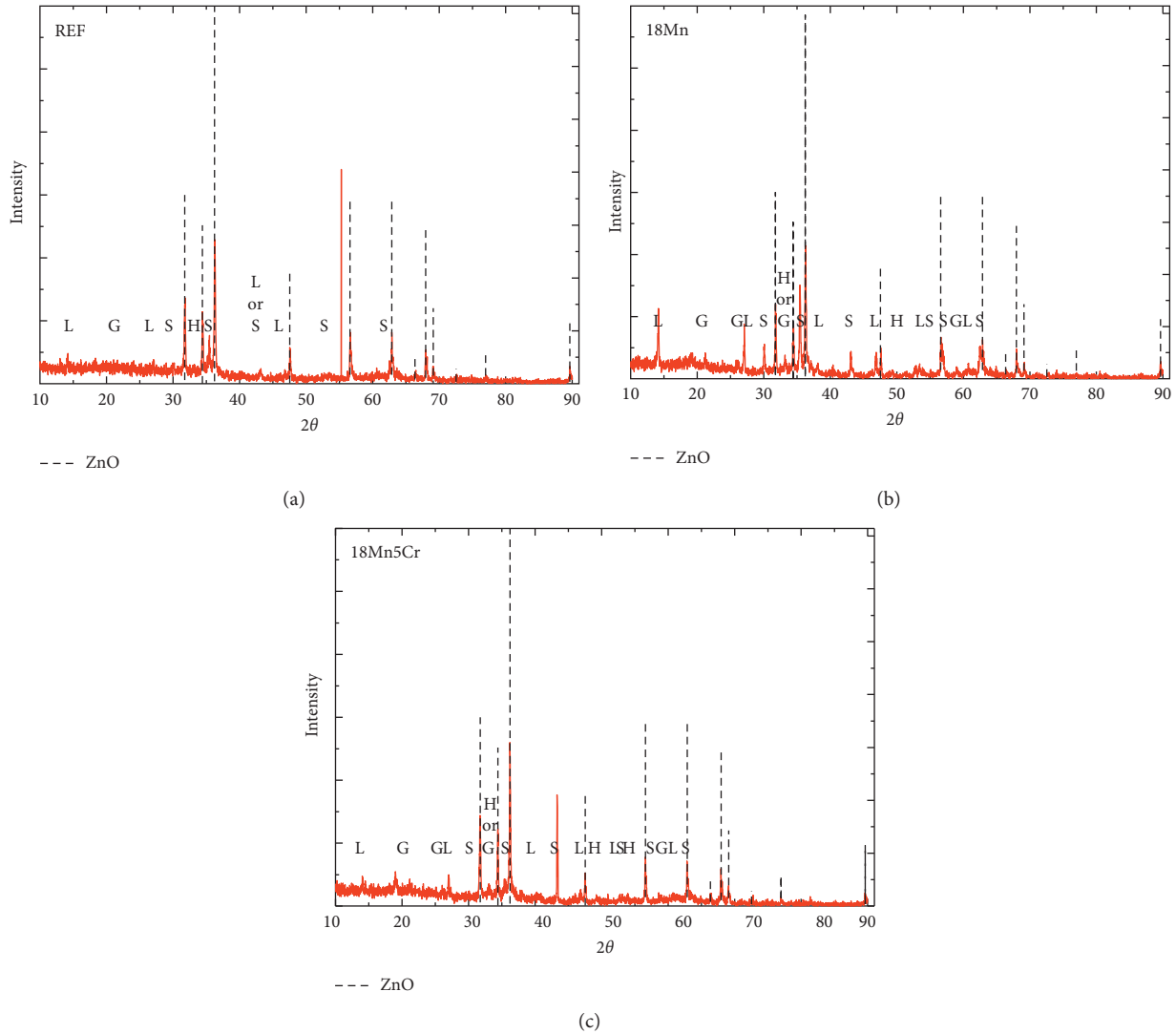


FIGURE 3: XRD patterns of the nonadherent rust (NAR) formed on (a) REF, (b) 18Mn, and (c) 18Mn5Cr for 56 days in 3.5% NaCl solution at 60°C, where G, L, S, and H represent goethite, lepidocrocite, magnetite (or maghemite), and hematite, respectively.

rust. Therefore, the relationship between the alloying element and rust will be discussed based on the results of the rust analysis in Sections 3.3 and 3.4.

**3.2. Effect of Alloying Elements on Cathodic Polarization Curve.** Cathodic polarization tests were also conducted in order to confirm the effectiveness of the Tafel extrapolation

method in evaluating the corrosion rate. Figure 2(b) shows that cathodic current densities for all the alloys increased with immersion unexpectedly. The increase of the cathodic current density resulted from the involvement of electrochemical reaction of rust [4, 42, 43]. However, the effects of electrochemical reduction of rust on both the Tafel slope and the corrosion rate induced from Tafel extrapolation were different among both alloys and immersion periods. On the

TABLE 5: Results on XRD qualitative analysis of nonadherent rusts (NARs) formed for 56-day exposure in 3.5% NaCl solution according to the internal standard method.

Alloys	Phase fraction (wt.%)					Total
	Goethite	Akaganeite	Lepidocrocite	Spinel oxide*	Hematite	
REF	0.2	0.0	10.8	4.7	7.4	21.1
18Mn	1.0	0.0	9.9	5.3	4.0	20.2
18Mn5Cr	4.2	0.0	10.3	0.3	4.6	19.4

\* Magnetite or maghemite.

other hand, the electrochemical reduction of rust formed on 18Mn5Cr for 56-day period was not involved in the potential range between the corrosion potential and the potential by 100 mV lower than the corrosion potential. It decreased both the corrosion rate and the Tafel slope in Table 4 as a typical cathodic behavior of steel with a protective rust layer. Meanwhile, the electrochemical reduction of rust formed on 18Mn for 56-day period was involved in the entire range of potential between the corrosion potential and the potential by 100 mV lower than the corrosion potential. It increased the cathodic current in Figure 2(b) pretending to increase the corrosion rate in Table 4 unlike in Figure 1. The electrochemical reduction of rust formed on REF for 56-day period was involved near a potential by 100 mV lower than the corrosion potential, increasing the Tafel slope with the decreased corrosion rate in Table 4 though the cathodic current increased in Figure 2(b). Hence, the extrapolation method could not provide reliable data for the instantaneous corrosion rate of steels with various alloying elements and immersion periods.

**3.3. Analysis of Nonadherent Rust by XRD and Raman Spectroscopy.** Figure 3 shows the XRD spectra of the NARs from the alloys immersed for 56 days. The NARs consisted of goethite (JCPDS no. 29-0713), lepidocrocite (JCPDS no. 44-1415), spinel oxide (magnetite (JCPDS no. 39-1346) or maghemite (JCPDS 19-0629)), and hematite (JCPDS no. 33-0664). The NAR constituents were independent of alloying elements. Table 5 shows the quantitative analysis summaries of the NARs. The concentration of each iron oxide in the NARs depended on the alloying element. Compared with no alloying element, the addition of chromium as an alloying element increased the concentration of goethite, which is beneficial to the corrosion resistance of steels [15–18], but decreased the concentrations of hematite as well as spinel oxide which negatively affects the corrosion resistance of steels [15–18]. The addition of manganese as an alloying element also slightly increased the concentrations of goethite but not as much as that by chromium. These results are consistent with the effects of alloying elements on corrosion resistance described in Section 3.1 and 3.2. Additionally, the total concentration of iron oxides in Table 5 was far from 100%. This difference was caused by either the large amounts of amorphous rust presented during the initial period [28, 44–46] or detection limits of XRD and Raman spectroscopy on fine grains [44–46].

Figure 4 shows the Raman spectra of the NARs formed on the alloys. The Raman spectra of the NARs sampled from REF demonstrate the presence of goethite, lepidocrocite,

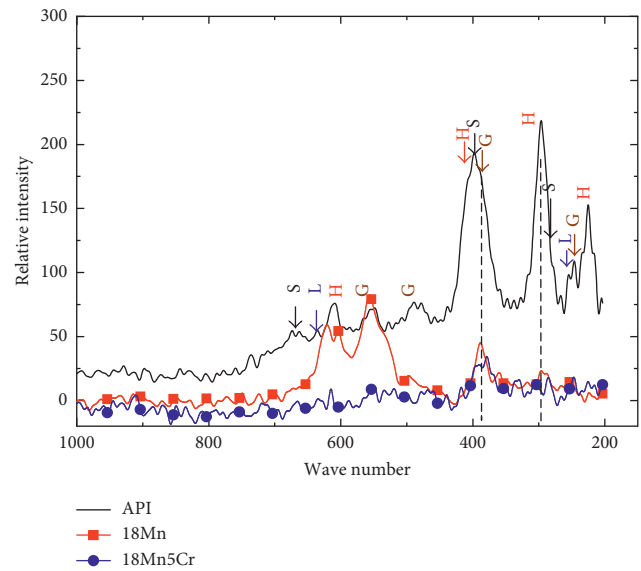


FIGURE 4: Raman spectra of the nonadherent rust (NAR) formed on REF, 18Mn, and 18Mn5Cr for 56 days in 3.5% NaCl solution at 60°C, where G, L, S, and H represent goethite, lepidocrocite, magnetite (or maghemite), and hematite, respectively. S: spinel oxide, H:  $\alpha$ -Fe<sub>2</sub>O<sub>3</sub>, G:  $\alpha$ -FeOOH, L:  $\gamma$ -FeOOH.

hematite, and magnetite which was confirmed by the absence of the broadband at 710 cm<sup>-1</sup> [47]. The Raman spectra of the NAR formed on the 18Mn mainly presented bands at 554, 390, 621, 598, and 500 cm<sup>-1</sup>, where the first two bands correspond to goethite and the last three bands possibly correspond to Mn-rich bixbyite ((Mn,Fe)<sub>2</sub>O<sub>3</sub>) [48]. In addition to major bands, bands for magnetite and hematite were detected with low intensity in the Raman spectra. The low density of hematite is due to the fact that manganese promotes the formation of Mn-rich iron bixbyite instead of the formation of hematite in NARs. In addition, no detection of lepidocrocite in the Raman spectrum from the 18Mn is possible due to low sensitivity of lepidocrocite in Raman spectroscopy, which was also observed in the NARs sampled from REF in Figure 4, corresponding to 10.8% of lepidocrocite as listed in Table 5. The Raman spectrum of the NARs formed on the 18Mn5Cr was also similar to that from the NARs of the 18Mn, with an exception of the absence of bands from Mn-rich bixbyite. The absence of Mn-rich iron oxide in the NARs from the 18Mn5Cr is due to the stabilization of oxyhydroxides by chromium as listed in Table 5.

XRD and Raman spectrum analysis did not find maghemite and akaganeite in the NARs in comparison to past experiments

and previous studies that were performed at room temperature [18, 49]. The formation of hematite or Mn-rich iron oxide from dihydroxylation of oxyhydroxide via maghemite [22] may have resulted from conducting the experiment at a higher temperature than at room temperature, increasing the rate of the reaction for formation of hematite. The higher testing temperature may also have caused transformation of akaganeite to stable oxyhydroxide or hematite [29].

Therefore, the NARs from all the alloys, independent of alloying elements, consisted of goethite, lepidocrocite, magnetite, and hematite. However, the concentration of constituents in the NARs depended on alloying elements, affecting corrosion resistance of the alloys.

**3.4. Analysis of Adherent Rust by XRD and TEM.** Figure 5 shows the spectra of rusts sampled from the alloys immersed for 56 days. Two measurement methods for the XRD spectrum both demonstrate the presence of spinel oxide in the ARs despite the difference in their intensities. Afterwards, the spinel oxide was identified with magnetite from the results of EELS analysis as shown in Table 6 and (3).

For more detailed examination, the ARs were used for TEM analysis with EDS, SAED, and EELS. Their results are shown in Figures 6–8. Figure 6(a) shows that the ARs sampled from the REF consisted of white and gray regions. Both regions contained iron and oxygen, but the white region had lower concentration of iron than the gray region as shown in Figure 6(b). In addition, the EELS analysis as shown in Table 6 and Figure 9 demonstrated higher concentration of ferric iron in the white region which formed along the alloy/rust interface and across the AR in a line form such as a grain boundary. To satisfy the EDS and EELS analysis results, the oxidation state of iron is higher and the atomic ratio of iron to oxygen is lower in the white region. The Pt peak observed from EDS analysis came from platinum coated on the sample surface before FIB cutting. The Pt peak was no more mentioned hereafter. The SAED analysis further supports the findings, where the white region near the metal/rust interface mainly consists of ferroxhyte (JCPDS no. 18-0087) and magnetite as shown in Figure 6(c), while the gray region is identified with magnetite as shown in Figure 6(d). Hence, the distribution of the oxidation state of iron in the ARs from the REF indicates that the penetration of oxygen through a fast transport pathway controls the corrosion process of the REF.

Figures 7(a) and 7(b) provide TEM images of the ARs on the 18Mn and the EDS analyses, respectively. Contrast in the rust as shown in Figure 7(a) is relatively constant compared to that in Figure 6(a), and the concentration of iron, manganese, and oxygen remained constant as in the REF except for the presence of metallic components shown as point 2 in Figure 7(a). The latter is near the AR/NAR interface. In addition, the ratio shown in Table 6 and Figure 9 is almost constant, regardless of the area, and was lower than the ratio detected from the ARs from the REF. This outcome indicates that the oxidation state of iron in the ARs from the 18Mn is lower than that in the ARs from the REF [41]. The lower oxidation state of iron in the ARs was confirmed by the

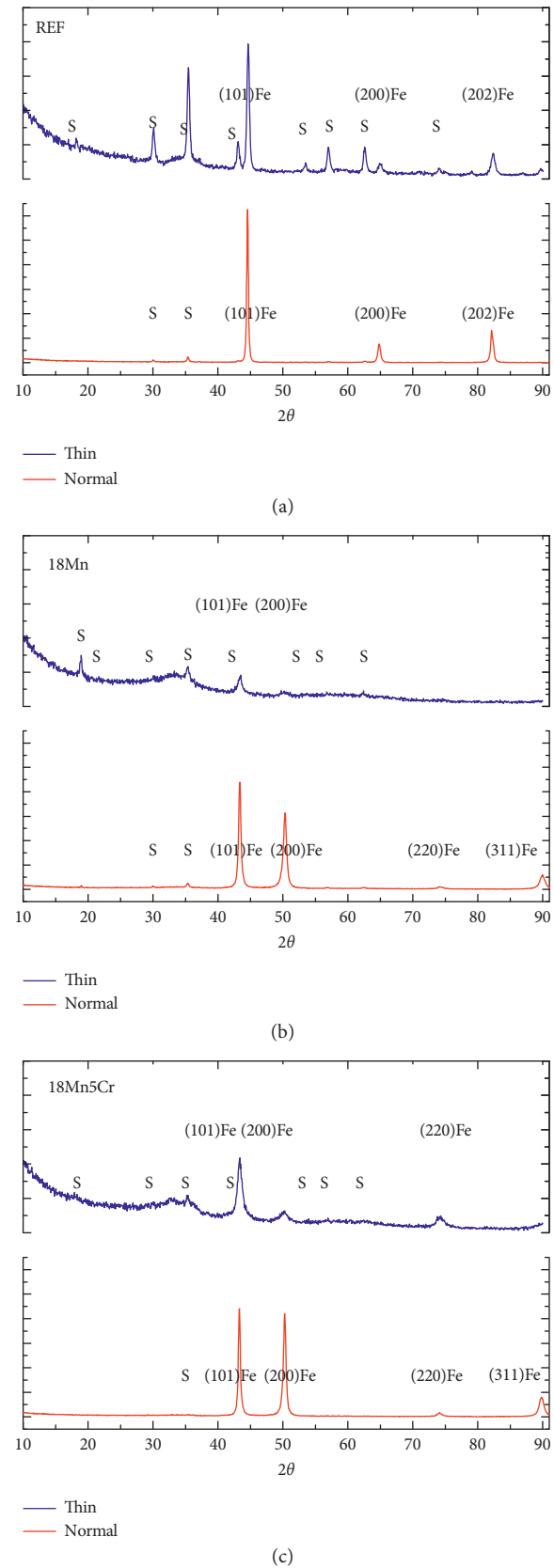


FIGURE 5: XRD patterns of the adherent rust (AR) formed on (a) REF, (b) 18Mn, and (c) 18Mn5Cr for 56 days in 3.5% NaCl solution at 60°C, where S represents magnetite (or maghemite).

TABLE 6: Summary on the integral intensity ratio of Fe L<sub>3</sub> edge peak to Fe L<sub>2</sub> edge peak depending on various positions among rust formed on REF, 18Mn, and 18Mn5Cr for 56 days in 3.5% NaCl solution at 60°C.

Alloy	Distance from metal/rust interface ( $\mu\text{m}$ )	Points in Figures 6–8	$I(\text{Fe L}_3)/I(\text{Fe L}_2)$
REF	0.133	e1 in Figure 6(a)	6.01
	0.333	e2 in Figure 6(a)	5.50
	0.320	e3 in Figure 6(a)	6.26
	0.400	e4 in Figure 6(a)	6.82
	0.827	e5 in Figure 6(a)	5.97
	0.880	e6 in Figure 6(a)	7.06
	1.100	e7 in Figure 6(a)	6.37
18Mn	0.165	e1 in Figure 7(a)	5.65
	0.235	e2 in Figure 7(a)	5.46
	0.424	e3 in Figure 7(a)	5.57
18Mn5Cr	0.036	e1 in Figure 8(a)	4.65
	0.100	e2 in Figure 8(a)	5.46
	0.229	e3 in Figure 8(a)	5.36

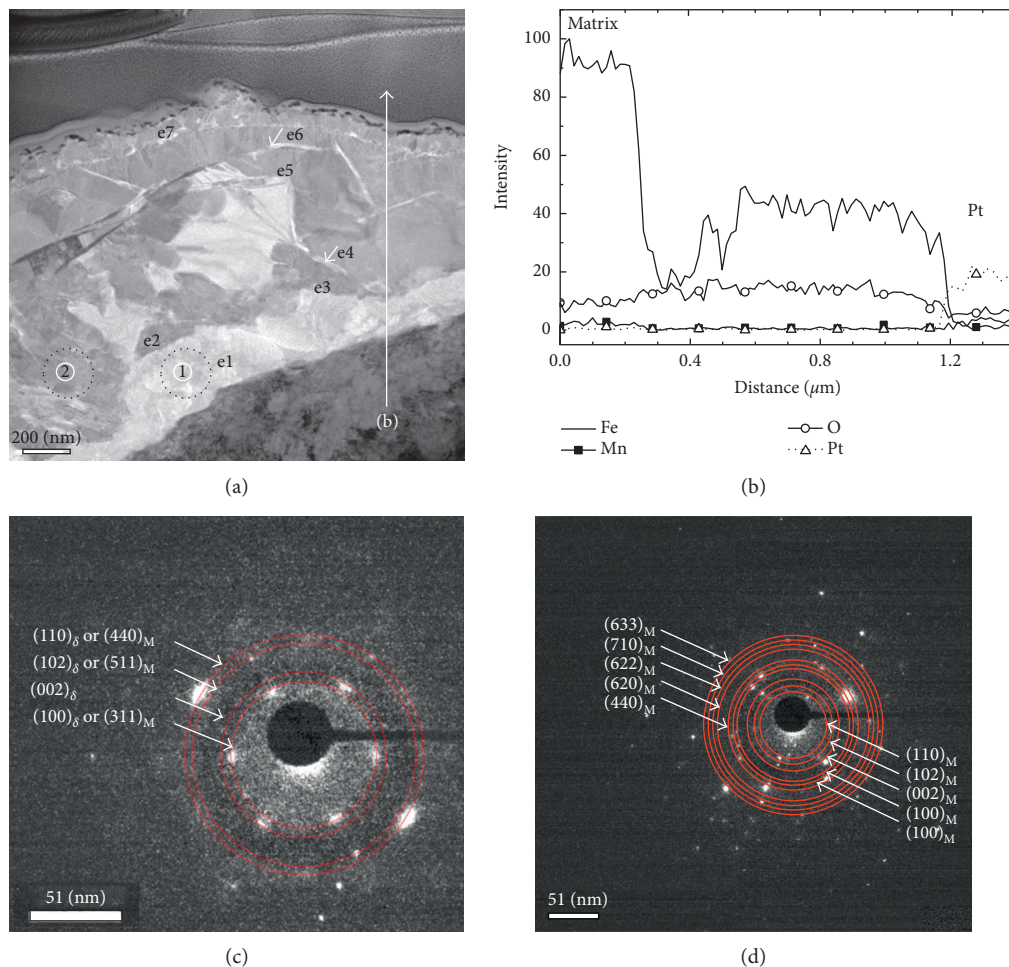


FIGURE 6: Cross-sectional TEM image (a), EDS line profile (b), and SAEDs (c-d) of regions 1 and 2 in rust formed during 56-day immersion of REF in 3.5% NaCl solution at 60°C, where the subscripts  $\delta$  and M indicate ferroxhyte and magnetite, respectively.

identification of the ARs as magnetite from SAED analysis as shown in Figure 7(d). Furthermore, more TEM spots with an interplanar spacing of  $\{hkl\}$  ( $d_{hkl}$ ) in Figure 7(d) than in Figure 6(c) or 6d indicate that the AR grain sizes on the

18Mn is smaller than those on the REF when the aperture sizes marked as the dot circles as shown are compared in Figures 6(a) and 7(a). From the abovementioned results, manganese as an alloying element aided the uniform

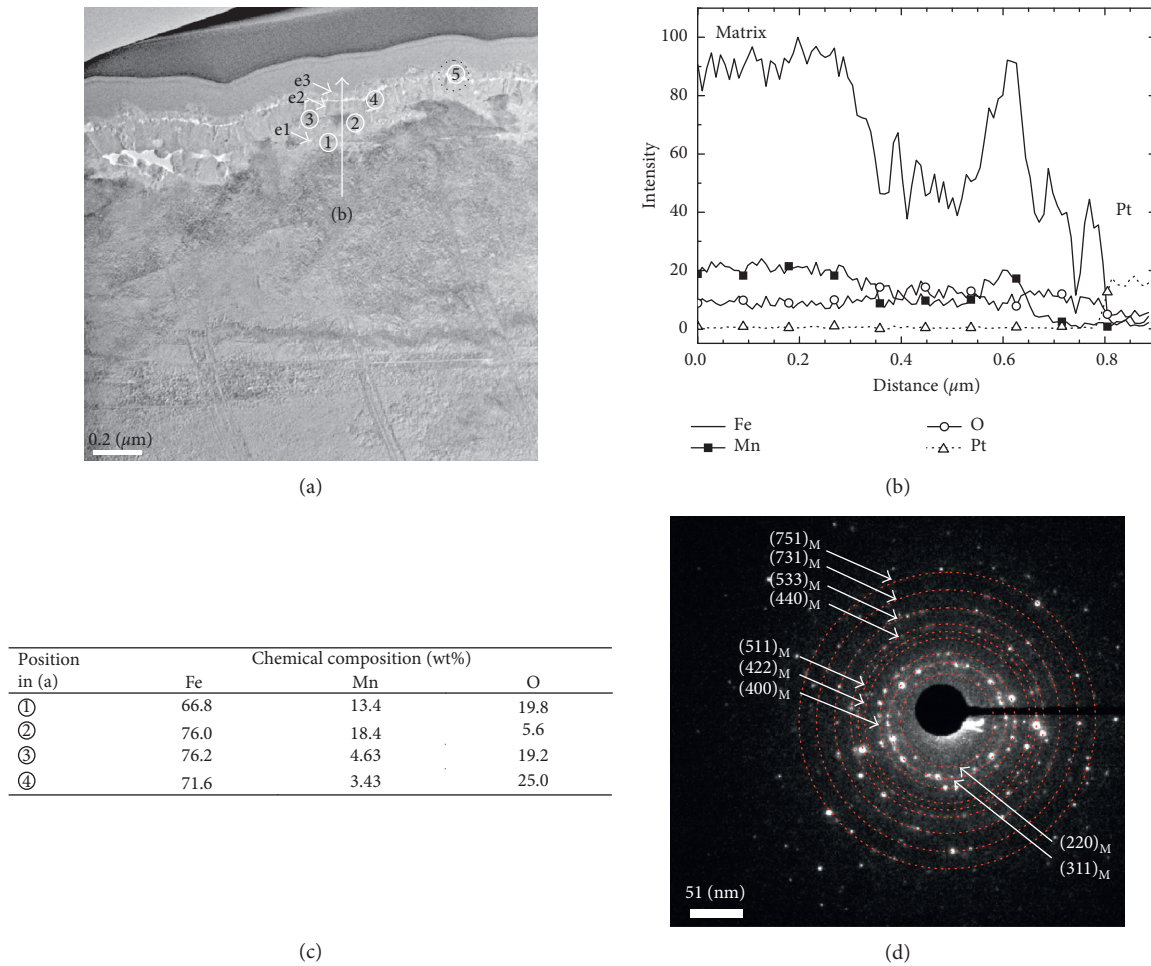


FIGURE 7: Cross-sectional TEM image (a), EDS line profile (b), EDS quantitative analysis of selected points 1, 2, 3, and 4 (c), and SAED (d) of region 5 in rust formed during 56-day immersion of 18Mn in 3.5% NaCl solution at 60°C, where subscript M indicates magnetite.

formation of rust and the refinement of the grain sizes of ARs, allowing oxygen to penetrate into ARs, retarding the formation of ferric ion, and ultimately increasing the corrosion resistance of the 18Mn.

Figure 8(a) shows a TEM image of the ARs from the 18Mn5Cr. Similar to Figure 7(a), the image was almost constant contrast, whereas the EDS intensities in Figure 8(b) were almost constant, unlike in Figure 7(b), except the decreased intensity of iron from a distance longer than 0.2 μm away from the alloy/AR interface. As shown in Figure 8(c), those outcomes caused the enrichment of manganese and chromium. Despite the enrichment of chromium and manganese, however, the ratio shown in Table 6 and Figure 9 is almost as constant as that of AR formed on the 18Mn, indicating that the oxidation state of iron in the AR from the 18Cr5Mn is the same as that of the AR from the 18Mn. Figures 8(d) and 8(e) demonstrate that the ARs from the 18Cr5Mn were mainly magnetite and have the finest grain based on the comparison of aperture sizes in Figures 6(a), 7(a), and 8(a). Here, chromium and manganese enrichments near the AR/NAR interface may be explained with the substitution of ferric ion and ferrous ion by chromium(III) and manganese(II) in magnetite, respectively.

As both chromium and manganese retard the formation of magnetite [34] and aid the formation of oxyhydroxide in the NARs, iron ions may have diffused out and promoted the enrichment. Therefore, chromium aids the uniform rust formation and the refinement of the grain size in ARs and the formation of enriched (Cr, Mn) oxyhydroxide in the NARs, hindering effective oxygen penetration into ARs and increasing the corrosion resistance of 18Mn5Cr.

#### 4. Discussion

Since the corrosion resistance of steels was controlled by the penetration of oxygen into rust, the following modification of rust properties by chromium and manganese improved the corrosion resistance as sketched in Figure 10. Compared to the rust on the REF, both chromium and manganese accelerate the formation of goethite in NARs and fine-grained magnetite in ARs, though the chromium is more effective than manganese as shown in Figures 10(b) and 10(c). The higher effectiveness of chromium on corrosion resistance of steels is because both the formation rate and refinement of goethite are enhanced in NARs [4, 36, 50] as well as AR grain sizes are more refined [36]. The higher

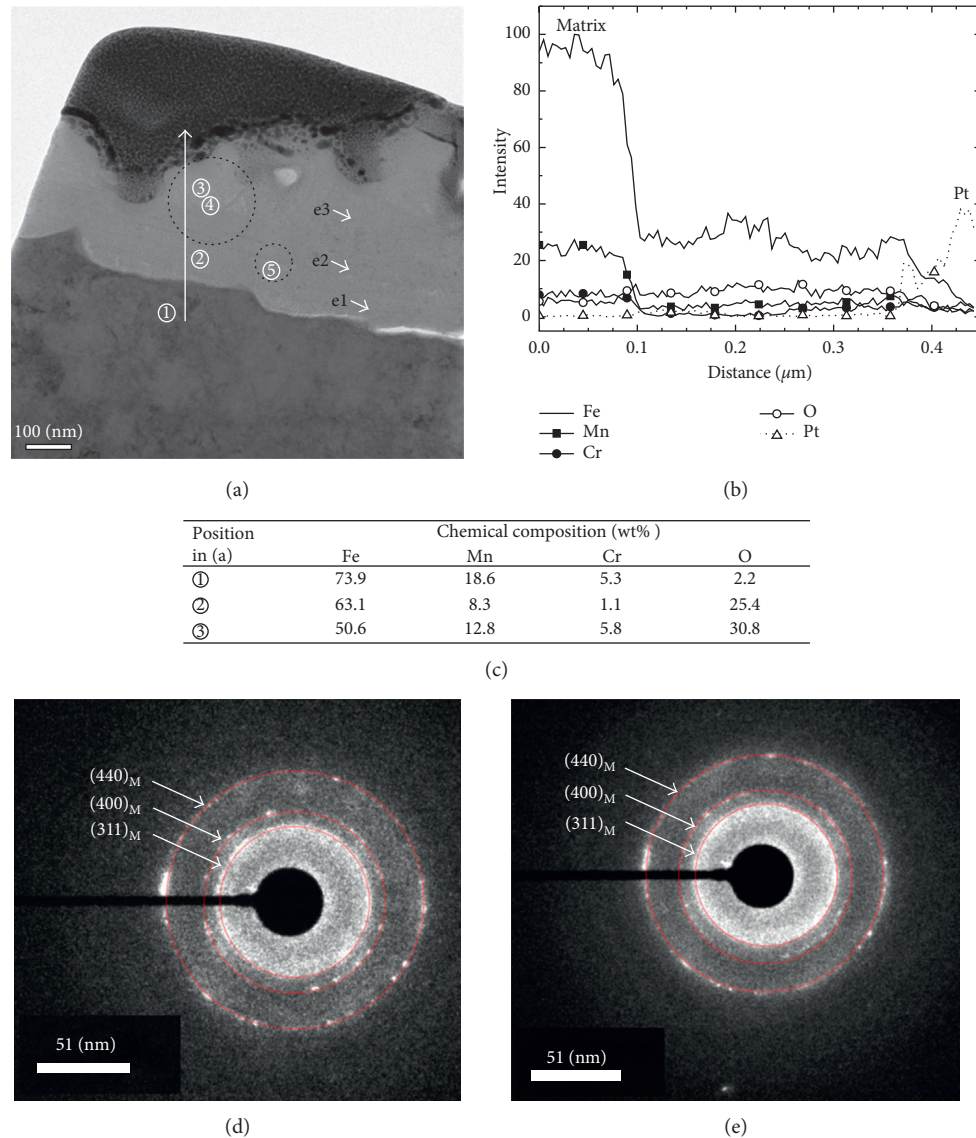


FIGURE 8: Cross-sectional TEM image (a), EDS line profile (b), EDS quantitative analysis of selected points 1, 2, and 3 (c), and SAEDs (d-e) of regions 4 and 5 in rust formed during 56-day immersion of 18Mn5Cr in 3.5% NaCl solution at 60°C, where subscript M indicates magnetite.

effectiveness of chromium on the formation of goethite has been explained with both facilitated incorporation of chromium into goethite as chromium is more soluble than manganese [51, 52] and faster precipitation of chromium (III) ion to  $\text{Cr}(\text{OH})_3$  than ferrous ion during the oxidation of the ferrous solutions [50]. The fast pathway where oxygen is transported across NARs is provided by pores or their surface area. The porosity of rust is affected by phase transformation of rust, interparticle spacing, type of iron oxide and substituting ions into the oxide, grain size, and crystal structure [24]. However, a higher porosity does not always result in a higher transport rate due to mobility and the size of the pore [24]. For example, more refined grain provides a low transport rate of oxygen despite its high surface area. Accordingly, the study on mobility as well as the size of the pore remains for future work. Therefore, the lower transport rate of oxygen across rust on the alloy steels

(18Mn, 18Mn5Cr) was explained with the more refined grain size of goethite in the NARs without further mentioning porosity.

Unlike previous studies [15, 16, 18], which state that magnetite is related to a decrease in corrosion resistance of steel, the ARs formed on the alloy steels with higher corrosion resistances contained fine magnetite as a main component. The discrepancy is due to the difference in the location of rust from the alloy/rust interface. Magnetite is formed from the following reactions: slow oxidation of ferrous hydroxide by way of GR, incorporation of ferrous ion into oxyhydroxide [7], or dissolution-precipitation process—the early precipitated oxyhydroxide reacts with the dissolved ferrous hydroxide to produce magnetite [29, 53]. On the alloy steels, magnetite exists as a main oxide in the inner layer of ARs because of the difficulty in transporting oxygen through both NARs and ARs. However,

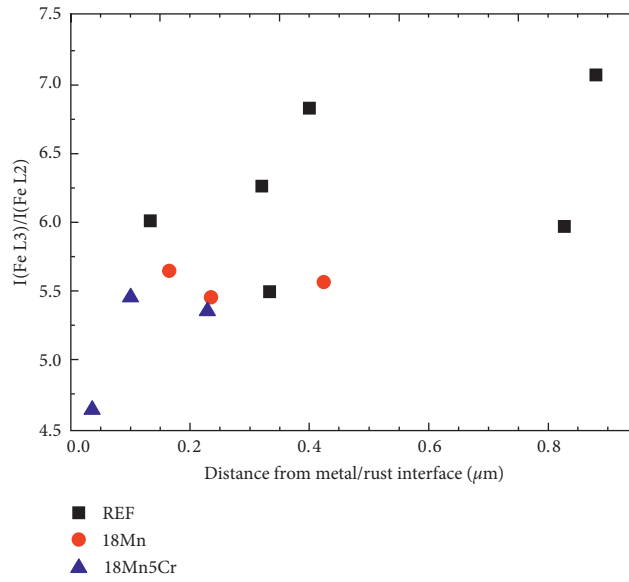


FIGURE 9: Integral intensity ratio of Fe L3 edge peak to Fe L2 edge peak depending on the distance from the metallic surface of REF, 18Mn, and 18Mn5Cr presented in Table 6.

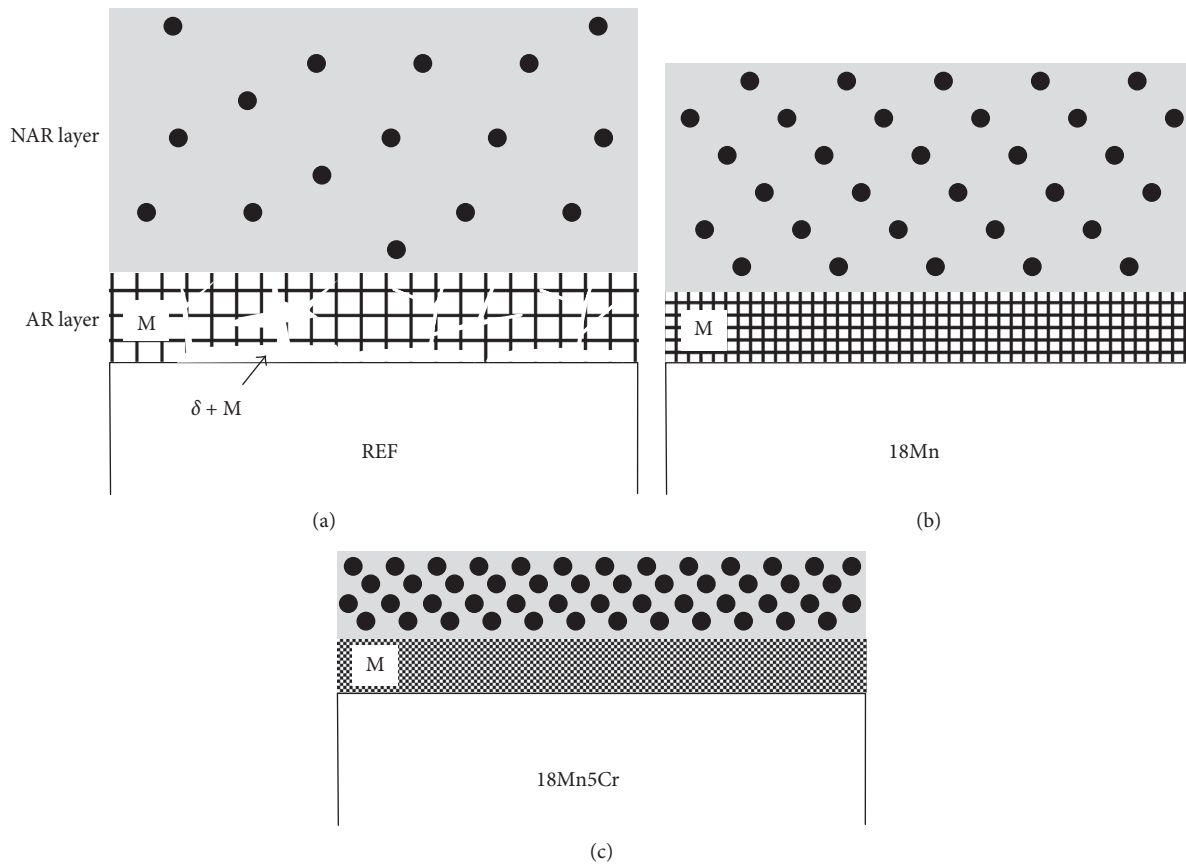


FIGURE 10: Schematic diagrams of rust layers formed on REF (a), 18Mn (b), and 18Mn5Cr (c) in 3.5% NaCl solution for 56 days at 60°C, where solid circle, M, and  $\delta$  indicate goethite, magnetite, and feroxyhyte, respectively.

the formation of the less-protective rust layer like the NAR and the AR on the REF provides a fast pathway for oxygen penetration and aids oxyhydroxide formation [28], decreasing the concentration of magnetite. Hence, the higher concentration of magnetite in the AR indicates the higher resistance of the alloy on which the AR is formed unlike the expectation according to (1).

## 5. Conclusions

From the evaluation of corrosion resistance of REF, 18Mn, and 18Mn5Cr in 60°C 3.5% NaCl solution and the analysis of the AR and NAR by XRD, Raman spectroscopy, TEM-EDS, TEM-SADP, and TEM-EELS, the corrosion process and the effects of chromium and manganese on the process are described in detail in the following:

- (1) In 60°C NaCl solution, the corrosion processes of all the alloys were controlled by the oxygen transport through the rust layer. The weight loss behavior conformed to a typical parabolic law; the oxidation state of iron in rust was higher along the fast pathway but it was not proportional to the longer distance from the alloy/AR interface.
- (2) Both chromium and manganese as alloying elements not only increased the amounts of goethite in NARs but also refined the AR grain size. In addition, the alloying elements decreased the concentration ratio of ferric ion to ferrous ion in ARs indicating the difficulty in oxygen penetration.
- (3) The higher corrosion resistance of 18Mn5Cr resulted from the effectiveness of chromium in refinements of AR grains and increased amounts of goethite in NARs.

In addition, the Tafel extrapolation method does not provide reliable data for the instantaneous corrosion rate of steels with various alloying elements and immersion periods because the electrochemical reduction rate of rust depends on its constituents as well as corrosion potentials which are affected by the alloying element.

## Conflicts of Interest

The author declares that there are no conflicts of interest regarding the publication of this paper.

## Acknowledgments

The authors gratefully acknowledge the financial supports from POSCO.

## References

- [1] H. N. Han, C.-S. Oh, G. Kim, and O. Kwon, "Design method for TRIP-aided multiphase steel based on a microstructure-based modelling for transformation-induced plasticity and mechanically induced martensitic transformation," *Materials*

- Science and Engineering: A*, vol. 499, no. 1-2, pp. 462–468, 2009.
- [2] O. Soderberg, "Corrosion behaviour of Fe–Mn–Si based shape memory steels trained by cold rolling," *Materials Science and Engineering: A*, vol. 273–275, pp. 543–548, 1999.
- [3] M. B. Kannan, R. K. S. Raman, and S. Khoddam, "Comparative studies on the corrosion properties of a Fe–Mn–Al–Si steel and an interstitial-free steel," *Corrosion Science*, vol. 50, no. 10, pp. 2879–2884, 2008.
- [4] Y. Hyun and H. Kim, "Effects of alloying elements (Cr, Mn) on corrosion properties of carbon steel in synthetic seawater," *Korean Journal of Metals and Materials*, vol. 54, pp. 68–78, 2016.
- [5] Y. Hyun and H. Kim, "Effects of alloying elements on the corrosion properties of high strength steel in a sour environment," *Korean Journal of Metals and Materials*, vol. 54, no. 12, pp. 885–892, 2016.
- [6] Y. S. Zhang and X. M. Zhu, "Electrochemical polarization and passive film analysis of austenitic Fe–Mn–Al steels in aqueous solutions," *Corrosion Science*, vol. 41, no. 9, pp. 1817–1833, 1998.
- [7] X. M. Zhu and Y. S. Zhang, "Investigation of the electrochemical corrosion behavior and passive film for Fe–Mn, Fe–Mn–Al, and Fe–Mn–Al–Cr alloys in aqueous solutions," *Corrosion Science*, vol. 54, no. 1, pp. 3–12, 1998.
- [8] P. H. Refait, M. Abdelmoula, and J. M. R. Genin, "Mechanisms of formation and structure of green rust one in aqueous corrosion of iron in the presence of chloride ions," *Corrosion Science*, vol. 40, no. 9, pp. 1547–1560, 1998.
- [9] G. Mcadam and D. J. Young, "Mechanisms of the simultaneous sulfidation and oxidation of Fe–Mn alloys," *Corrosion Science*, vol. 38, no. 2, pp. 247–266, 1996.
- [10] K. Asami and M. Kikuchi, "Characterization of rust layers on weathering steels air-exposed for a long period," *Materials Transactions*, vol. 43, no. 11, pp. 2812–2825, 2002.
- [11] J. Rawers, "Oxidation characteristics of Fe–18Cr–18Mn-stainless steel alloys," *Oxidation of Metals*, vol. 74, no. 3-4, pp. 167–178, 2010.
- [12] D. Neff, P. Dillmann, L. Bellot-Gurlet, and G. Beranger, "Corrosion of iron archaeological artefacts in soil: characterisation of the corrosion system," *Corrosion Science*, vol. 47, no. 2, pp. 515–535, 2005.
- [13] R. E. Melchers, "Effect of small compositional changes on marine immersion corrosion of low alloy steels," *Corrosion Science*, vol. 46, no. 7, pp. 1669–1691, 2004.
- [14] R. E. Melchers, "Long-term corrosion of cast irons and steel in marine and atmospheric environments," *Corrosion Science*, vol. 68, pp. 186–194, 2013.
- [15] S. Hara, T. Kamimura, H. Miyuki, and M. Yamashita, "Taxonomy for protective ability of rust layer using its composition formed on weathering steel bridge," *Corrosion Science*, vol. 49, no. 3, pp. 1131–1142, 2007.
- [16] T. Kamimura, S. Hara, H. Miyuki, M. Yamashita, and H. Uchida, "Composition and protective ability of rust layer formed on weathering steel exposed to various environments," *Corrosion Science*, vol. 48, no. 9, pp. 2799–2812, 2006.
- [17] A. L. Morales, D. Cartagena, J. L. Rendon, and A. Valencia, "The relation between corrosion rate and corrosion products from low carbon steel," *Physica Status Solidi (B)*, vol. 220, no. 1, pp. 351–356, 2000.
- [18] F. R. Perez, C. A. Barrero, A. R. Hight Walker, K. E. Garcia, and K. Nomura, "Effects of chloride concentration, immersion time and steel composition on the spinel phase formation," *Materials Chemistry and Physics*, vol. 117, no. 1, pp. 214–223, 2009.

- [19] M. Yamashita, H. Miyuki, Y. Matsuda, H. Nagano, and T. Misawa, "The long term growth of the protective rust layer formed on weathering steel by atmospheric corrosion during a quarter of a century," *Corrosion Science*, vol. 36, pp. 283–299, 1994.
- [20] P. H. Bauer, J. M. Genin, and D. Rezel, "Mössbauer effect evidence of chlorine environments in ferric oxyhydroxides from iron corrosion in chlorinated aqueous solution," *Hyperfine Interactions*, vol. 28, no. 1-4, pp. 757–760, 1986.
- [21] R. A. Robie, B. S. Hemingway, and J. R. Fischer, *Thermodynamic properties of minerals and related substances at 298.15 K and 1 bar (105 pascals) pressure and high temperatures*, Washington, DC, USA, 1978.
- [22] R. M. Cornell and U. Schwertmann, *The Iron Oxides*, p. 181, VCH Publishers, New York, NY, USA, 1996.
- [23] S. J. Oh, D. C. Cook, and H. E. Townsend, "Atmospheric corrosion of different steels in marine, rural and industrial environments," *Corrosion Science*, vol. 41, no. 9, pp. 1687–1702, 1999.
- [24] R. M. Cornell and U. Schwertmann, *The Iron Oxides*, pp. 98–110, VCH Publishers, New York, NY, USA, 2006.
- [25] U. R. Evans and C. A. J. Taylor, "Mechanism of atmospheric rusting," *Corrosion Science*, vol. 12, no. 3, pp. 227–246, 1972.
- [26] J. T. Keiser, C. W. Brown, and R. H. Heidersbach, "The electrochemical reduction of rust films on weathering steel surfaces," *Journal of the Electrochemical Society*, vol. 129, no. 12, pp. 2686–2689.
- [27] J. P. Jolivet, E. Tronc, and C. R. Chaneac, "Iron oxides: from molecular clusters to solid. A nice example of chemical versatility," *Comptes Rendus Geoscience*, vol. 338, no. 1-7, pp. 488–497, 2006.
- [28] T. Misawa, T. Kyuno, W. Suetaka, and S. Shimodaira, "The mechanism of atmospheric rusting and the effect of Cu and P on the rust formation of low alloy steels," *Corrosion Science*, vol. 11, no. 1, pp. 35–48, 1971.
- [29] T. Ishikawa, Y. Kondo, A. Yasukawa, and K. Kandori, "Formation of magnetite in the presence of ferric oxyhydroxides," *Corrosion Science*, vol. 40, no. 7, pp. 1239–1251, 1998.
- [30] Y. Tamaura, K. Ito, and T. Katsura, "Transformation of  $\gamma$ -FeO(OH) to  $\text{Fe}_3\text{O}_4$  by adsorption of iron(II) ion on  $\gamma$ -FeO(OH)," *Journal of the Chemical Society, Dalton Transactions*, no. 2, pp. 189–194, 1983.
- [31] R. M. Cornell, "The influence of some divalent cations on the transformation of ferrihydrite to more crystalline products," *Clay Minerals*, vol. 23, no. 3, pp. 329–332, 1988.
- [32] R. M. Cornell and R. Giovanoli, "The influence of copper on the transformation of ferrihydrite ( $5\text{Fe}_2\text{O}_3 \rightarrow 9\text{H}_2\text{O}$ ) into crystalline products in alkaline media," *Polyhedron*, vol. 7, no. 5, pp. 385–391, 1988.
- [33] C. A. Barrero, A. L. Morales, J. Restrepo et al., "Synthesis of magnetite in presence of  $\text{Cu}^{2+}$  or  $\text{Cr}^{3+}$ ," *Hyperfine Interactions*, vol. 134, no. 1, pp. 141–152, 2001.
- [34] T. Ishikawa, M. Kumagai, A. Yasukawa, K. Kandori, T. Nakagama, and F. Yuse, "Influences of metal ions on the formation of  $\gamma$ -FeOOH and magnetite rusts," *Corrosion Science*, vol. 44, no. 5, pp. 1073–1086, 2002.
- [35] C. A. Barrero, A. L. Morales, J. Mazo-Zuluaga et al., "Synthesis and Mossbauer characterization of Cu and Cr doped magnetites," *Revista de Metalurgia (Madrid)*, vol. 39, pp. 62–67, 2003.
- [36] A. L. Morales, C. A. Barrero, F. Jaramillo, C. Arroyave, and J. M. Greneche, "Properties of goethite grown under the presence of  $\text{Cr}^{3+}$ ,  $\text{Cu}^{2+}$  and  $\text{Mn}^{2+}$  ions," *Hyperfine Interactions*, vol. 148/149, no. 1–4, pp. 135–144, 2003.
- [37] D. W. Kim and H. Kim, "Effects of alloying elements on corrosion resistance of low alloyed steels in a seawater ballast tank environment," *Korean Journal of Metals and Materials*, vol. 48, no. 6, pp. 523–532, 2010.
- [38] ASTM G 1, *Standard Practice for Preparing, Cleaning, and Evaluating Corrosion Test Specimens*, ASTM International, West Conshohocken, PA, USA, 2003.
- [39] D. A. Jones, *Principle and Prevention of Corrosion*, Prentice-Hall, New Jersey, NY, USA, 2nd edition, 1996.
- [40] C. Suryanarayana and M. G. Norton, *X-ray Diffraction—A Practical Approach*, Premium Publishing Co., New York, NY, USA, 1998.
- [41] P. A. van Aken, B. Liebscher, and V. J. Styrsa, "Quantitative determination of iron oxidation states in minerals using Fe L 2,3-edge electron energy-loss near-edge structure spectroscopy," *Physics and Chemistry of Minerals*, vol. 25, no. 5, pp. 323–327, 1998.
- [42] A. Raman, A. Razvan, B. Kuban, K. A. Clement, and W. E. Graves, "Characteristics of the rust from weathering steels in Louisiana bridge spans," *Corrosion*, vol. 42, pp. 447–455, 1986.
- [43] Y. Zou, J. Wang, and Y. Y. Zheng, "Electrochemical techniques for determining corrosion rate of rusted steel in seawater," *Corrosion Science*, vol. 53, no. 1, pp. 208–216, 2011.
- [44] M. Yamashita, H. Miyuki, H. Nagano, and T. Misawa, "Stabilizing process of rust layer formed on weathering steels by atmospheric corrosion for a long period," *Zairyo-to-Kankyo*, vol. 43, no. 1, pp. 26–32, 1994.
- [45] M. Yamashita, H. Nagano, T. Misawa, and H. E. Townsend, "Structure of protective rust layers formed on weathering steels by long-term exposure in the industrial atmospheres of Japan and North America," *ISIJ International*, vol. 38, no. 3, pp. 285–290, 1998.
- [46] M. Yamashita and T. Misawa, "Recent progress in the study of protective rust-layer formation on weathering steel," in *Proceedings of NACE 53rd Annual Conference (Corrosion 98)*, San Diego, CA, USA, March 1998.
- [47] S. J. Oh, D. C. Cook, and T. E. Townsend, "Characterization of iron oxides commonly formed as corrosion products on steel," *Hyperfine Interactions*, vol. 112, pp. 59–65, 1998.
- [48] F. Ospitali, D. C. Smith, and M. Lorblanchet, "Preliminary investigations by Raman microscopy of prehistoric pigments in the wall-painted cave at Roucadour, Quercy, France," *Journal of Raman Spectroscopy*, vol. 37, no. 10, pp. 1063–1071, 2006.
- [49] L. Hao, S. Zhang, J. Dong, and W. Ke, "Evolution of atmospheric corrosion of MnCuP weathering steel in a simulated coastal-industrial atmosphere," *Corrosion Science*, vol. 59, pp. 270–276, 2012.
- [50] M. Y. amashita, H. Uchida, and D. C. Cook, "Effect of  $\text{Cr}^{3+}$  and  $\text{SO}_4^{2-}$  on the structure of rust layer formed on steels by atmospheric corrosion," in *Outdoor Atmospheric Corrosion*, H. Townsend, Ed., p. 149, West Conshohocken, PA, USA, ASTM International, 2002.
- [51] D. C. Cook, S. J. Oh, R. Balasubramanian, and M. Yamashita, "The role of goethite in the formation of the protective corrosion layer on steels," *Hyperfine Interactions*, vol. 122, pp. 59–70, 1999.
- [52] A. Manceau, M. L. Schlegel, M. Musso et al., "Crystal chemistry of trace elements in natural and synthetic goethite," *Geochimica et Cosmochimica Acta*, vol. 64, no. 21, pp. 3643–3661, 2000.
- [53] Y. Tamaura and P. V. Buduan, "Studies on the oxidation of iron (II) ion during the formation of  $\text{Fe}_3\text{O}_4$  and  $\alpha$ -FeO(OH) by air oxidation of  $\text{Fe}[\text{OH}]_2$  suspensions," *Journal of the Chemical Society, Dalton Transactions*, no. 9, pp. 1807–1811, 1981.

## Research Article

# Transition of Dislocation Structures in Severe Plastic Deformation and Its Effect on Dissolution in Dislocation Etchant

Muhammad Rifai <sup>1</sup>, Ebad Bagherpour <sup>2</sup>, Genki Yamamoto,<sup>3</sup> Motohiro Yuasa,<sup>1</sup> and Hiroyuki Miyamoto <sup>1</sup>

<sup>1</sup>Department of Mechanical Engineering, Doshisha University, Kyoto, Japan

<sup>2</sup>Department of Materials Science and Engineering, School of Engineering, Shiraz University, Shiraz, Iran

<sup>3</sup>Graduate School of Science and Engineering, Doshisha University, Kyoto, Japan

Correspondence should be addressed to Muhammad Rifai; [rmuhamma@mail.doshisha.ac.jp](mailto:rmuhamma@mail.doshisha.ac.jp)

Received 27 September 2017; Revised 11 December 2017; Accepted 18 December 2017; Published 30 January 2018

Academic Editor: Alicia E. Ares

Copyright © 2018 Muhammad Rifai et al. This is an open access article distributed under the Creative Commons Attribution License, which permits unrestricted use, distribution, and reproduction in any medium, provided the original work is properly cited.

Transition of dislocation structures in ultrafine-grained copper processed by simple shear extrusion (SSE) and its effects on dissolution were manifested by simple immersion tests using a modified Livingston dislocation etchant, which attacks dislocations and grain boundaries selectively. The SSE process increased the internal strain evaluated by X-ray line broadening analysis until eight passes but decreased it with further extrusion until twelve passes. The weight loss in the immersion tests reflected the variation in the internal strain: namely, it increased until eight passes and then decreased with further extrusion to twelve passes. Taking our previous report on microstructural observation into account, it is suggested that variation in the internal strain is caused by both the variation in dislocation density and structural change of grain boundaries from equilibrium to nonequilibrium states or vice versa. Decreased dislocation density and structural change back to equilibrium state of grain boundaries in very high strain range by possibly dynamic recovery as pointed out by Dalla Torre were validated by X-ray and dissolution in the modified Livingston etchant in addition to the direct observation by TEM reported in our former report.

## 1. Introduction

Grain refinement to grain sizes below  $1\ \mu\text{m}$  by severe plastic deformation (SPD) is now well known for improving strength of bulk metallic materials for structural application [1]. Simple shear extrusion (SSE) technique is one of the SPD methods wherein deformation proceeds by pressing the material through a die with a specifically created direct extrusion path [2]. SSE as well as other SPD techniques represented by equal-channel angular pressing (ECAP) and accumulative roll bonding (ARB) produces ultrafine grain (UFG) materials with residual dislocation inside grains, which may cause unique physical and mechanical properties [3]. Dislocation density increases to the order of  $10^{15}\ \text{m}^{-2}$  with increasing number of passes in SPD, forming finally the so-called deformation-induced grain boundaries with some dislocations remained inside grains. However, we reported

in the previous study that the softening occurred with further passes after UFG formation in pure copper processed by SSE, and this softening was considered as a result of a decrease in dislocation density, which was revealed by scanning transmission electron microscope (STEM). This decrease in dislocation density after UFG formation may be caused by the dynamic recovery [3–5]. As a classic approach, a dislocation etchant has been used to locate discrete dislocations and its density in low plastic strain [6]. However, it was reported that the dissolution rate in a modified solution becomes sensitive to dislocation density in very high range and grain boundaries state with residual dislocations after SPD, and the dissolution rate was changed by the flush annealing in spite that grain size is not changed [4, 7]. This study was carried out in order to evaluate dislocation density in very high strain range using a modified Livingston etchant which is very sensitive to dislocations and to examine the dissolution behavior of UFG copper.

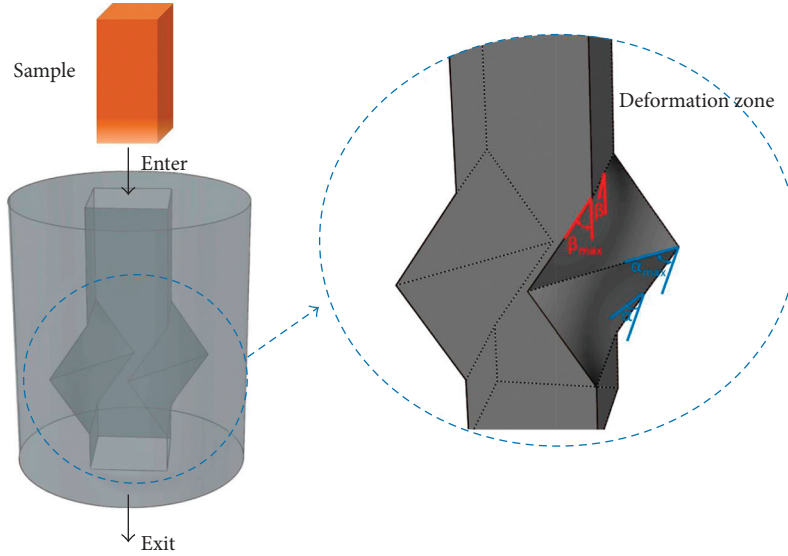


FIGURE 1: Schematic presentation of the SSE channel.

## 2. Experimental Procedure

**2.1. Simple Shear Extrusion (SSE).** A schematic representation of the SSE channel is shown in Figure 1 [3]. Through the deformation channel, the shear strain is gradually applied to the material while its cross-sectional area remains constant [2]. The direction of the shear is reversed at the middle of the channel where the specimen distorts with a maximum distortion angle of  $\alpha_{\max}$ . Another parameter of SSE processing is the inclination angle ( $\beta$ ), which exerts a profound effect on the deformation zone, strain rate, and the load of the process [2, 3, 8, 9]. The SSE can be conducted with a lower cost of production and easier installation than many other SPD methods owing to the straight movement of the billets through the channel.

A bisection die with the maximum distortion angle ( $\alpha_{\max}$ ) and the maximum inclination angle ( $\beta_{\max}$ ) of  $45^\circ$  and  $22.2^\circ$ , respectively, was designed and constructed, which applies an equivalent strain of 1.155 per pass, as shown in Figure 1 [3]. The deformation channel's cross section is a square with the side of 10 mm. The copper billets of commercial purity with a dimension of  $10 \text{ mm} \times 10 \text{ mm} \times 50 \text{ mm}$  were machined, annealed for 2 h at 923 K in argon atmosphere and then furnace cooled to room temperature as an initial material. A screw press with a ram speed of 0.2 mm/s was used for SSE processing, namely, route C where the sample is rotated in the same view by  $180^\circ$  between each pass was used for repeating SSE. The initial materials were subjected to two, four, eight, and twelve passes of SSE (see [3] for further details of SSE).

**2.2. Microstructural Characterization.** The microstructure of samples after two, four, eight and twelve passes of SSE was observed using a transmission electron microscope (JEM-2100F, JEOL) with an acceleration voltage of 200 kV. All the TEM specimens were prepared from extrusion direction (ED) section of the samples. The surface of the specimens

was mechanically grounded to the thickness of  $100 \mu\text{m}$  using a SiC abrasive paper. Then, the TEM specimens were thinned by a twin-jet polisher Tenupol 5 (Struers Co., Ltd.) at an applied voltage of 10 V in a mixture of 250 ml ethanol, 500 ml phosphoric acid, 50 ml propanol, and 5 g urea at 273 K until perforation. After that, the specimens were finally polished by an ion beam using the Gatan 691 precision ion polishing system.

**2.3. X-Ray Diffraction.** The measurement of X-ray diffraction (XRD) on the SSE-processed sample was conducted by the SmartLab, Rigaku. The integral breadth was determined after appropriate fitting of the scattered XRD pattern. The broadening in XRD data line consists of contributions due to coherent domain size,  $D$ , and microstrain,  $\epsilon$  [10]. The following equation was used to separate the contributions from each other for calculating the dislocation density  $\rho$  [10]:

$$\left(\frac{\beta \cos\theta}{\lambda}\right)^2 = \left(\frac{1}{D}\right)^2 + \left(\frac{4\epsilon \sin\theta}{\lambda}\right)^2, \quad (1)$$

where  $\beta$  is the value of the integral breadth (in radians),  $\theta$  is Bragg's diffraction angle, and  $\lambda$  is the wavelength of the X-ray beam ( $\text{\AA}$ ).

Several XRD peaks of high intensity ( $2\theta = 30\text{--}130^\circ$ ) were taken, and the plot of  $(\beta \cos\theta/\lambda)^2$  versus  $(\sin\theta/\lambda)^2$  was constructed [10]. The plots  $D$  and  $\epsilon$  were calculated using intercept =  $1/D^2$  and slope =  $16\epsilon^2$ . Then, the dislocation density can be calculated from  $D$  and  $\epsilon$ , with  $\eta = \text{integer number}$ , as [10] follows:

$$\rho_D = \frac{3\eta}{D^2} \text{ with } \eta = 1, \quad (2)$$

$$\rho_\epsilon = \frac{2k\epsilon^2}{b^2} \text{ with } k = 10, b = \text{Burgers vector}. \quad (3)$$

Finally, the dislocation density ( $\rho$ ) can be estimated by X-ray line broadening and obtained from dislocation

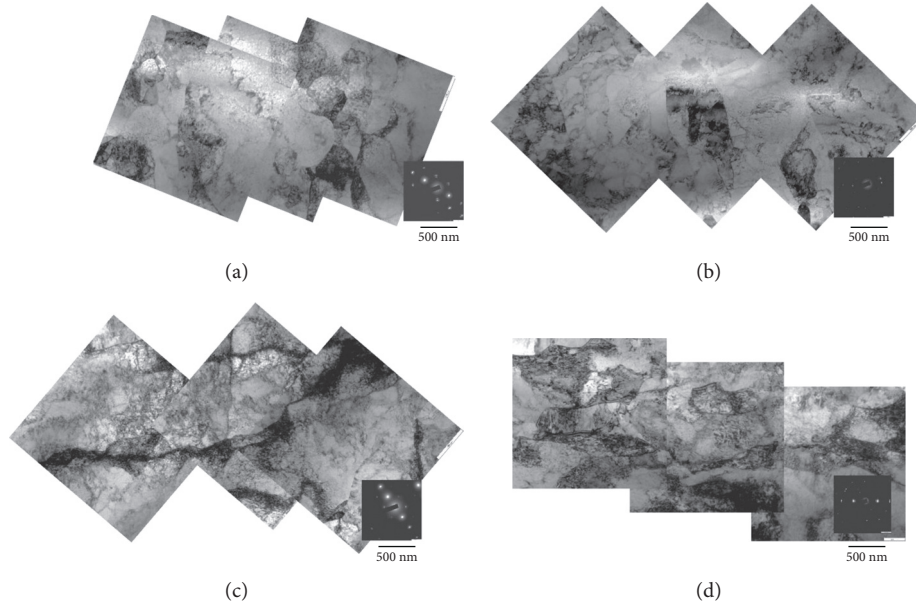


FIGURE 2: TEM micrographs of the SSE-processed sample: (a) two, (b) four, (c) eight, and (d) twelve passes.

densities that are related to  $D \cdot (\rho_D)$  and  $\varepsilon \cdot (\rho_\varepsilon)$  as follows [10]:

$$\rho = (\rho_D \cdot \rho_\varepsilon)^{1/2}. \quad (4)$$

**2.4. Immersion Testing.** The immersion tests were performed using the modified Livingston etchant (HCl: 30 ml; CH<sub>3</sub>COOH: 10 ml; H<sub>2</sub>O: 410 ml; pH = 0.41), which is known to attack dislocations and grain boundaries exclusively, leaving the other area intact [7]. The surface except the ED plane was coated with a nail lacquer to avoid a contact with the etchant solution. The immersion tests were conducted at stable room temperature condition for 1, 2, 4, 8, and 16 h. The morphology after 16 h immersion tests was observed by an optical microscope.

### 3. Results and Discussion

**3.1. Microstructural Observation.** Figure 2 shows the TEM images of the ED plane in the deformed specimens of two, four, eight, and twelve passes. After two passes, the microstructure showed a mixture of nondeformed and deformed grains with some dislocations. Up to eight SSE passes, the dislocation density increased and cell structures were observed. With increasing number of passes, the microstructure became more uniform and some grains with an average grain size of 1  $\mu\text{m}$  formed. When the strain was increased through twelve SSE passes, grain size is overall constant with an average of 0.9  $\mu\text{m}$ . Most interestingly, the dislocation density visible inside grains appeared to be lower than that after eight passes. The decrease in dislocation density in very high strain range after several passes in SPD was reported by Dalla Torre et al. [11], who ascribed it to the dynamic recovery during SPD.

Figure 3(a) shows the  $\{111\}$  peaks obtained from XRD analysis of the specimens. A significant line broadening can be observed with increasing SSE passes, which indicates a high density of dislocations and resultant long-range elastic stresses [12, 13]. The dislocation density calculated from (4) is shown in Figure 3(b) with other data estimated by direct observation by TEM [3]. The dislocation density increases gradually for two to eight passes and decreases after eight passes until twelve passes. So, the maximum dislocation density was achieved around eight passes. Though this trend is similar to the results obtained by STEM observation [3], there is a large discrepancy between two results. One possible reason for the discrepancy is that the direct observation by STEM counted only visible dislocations inside grains, whereas line broadening of XRD reflects the strain field by grain boundaries as well as discrete dislocations inside grains. Particularly, grain boundaries at nonequilibrium state are regarded as having extrinsic grain boundary dislocations and may exert a long-range stress field [14]. Therefore, decrease in dislocation density after eight passes is associated with decrease in extrinsic grain boundary dislocations, in other words, structural change from nonequilibrium to equilibrium state.

**3.2. Dissolution Behavior.** Figure 4 shows the weight loss of the as-annealed and SSE-processed specimens in the immersion tests in the modified Livingston etchant. The weight loss increased with increasing number of SSE passes until eight passes and decreased after twelve SSE passes. This trend was obtained for all immersion times. This result suggests that the dissolution of copper was promoted by SSE process until eight passes, but suppressed after higher passes until twelve passes.

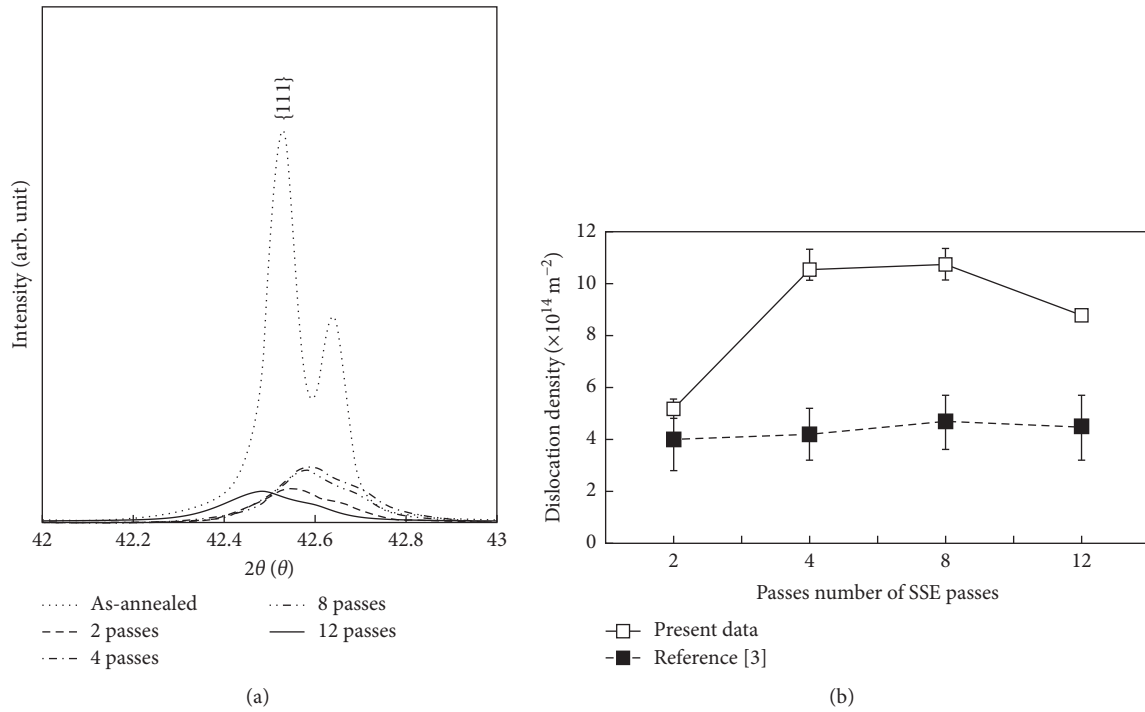


FIGURE 3: (a) {111} peaks of XRD patterns; (b) Dislocation density of SSE-processed sample by XRD.

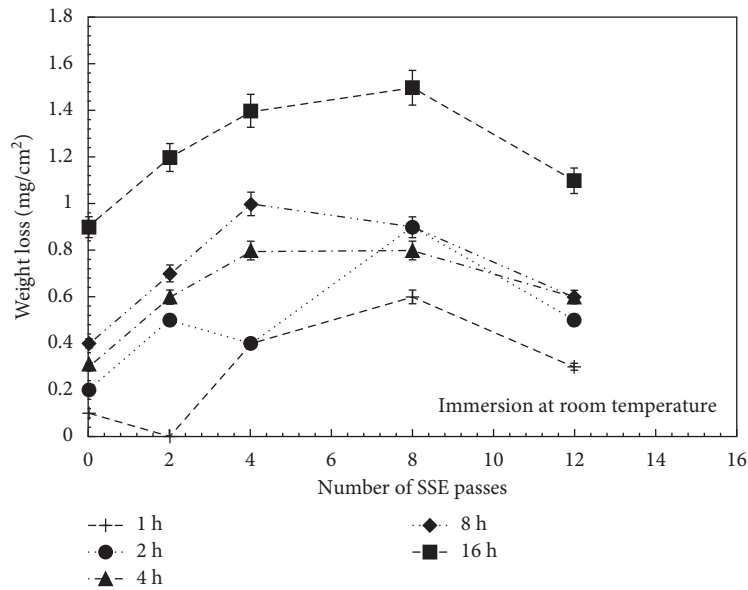


FIGURE 4: The weight loss of SSE-processed samples measured by the immersion tests in the modified Livingston etchant for 1, 2, 4, 8, and 16 hours.

The surface morphologies after immersion for 16 h in the Livingston etchant are shown in Figure 5. As shown in Figure 5(a), the grain boundaries groove in the as-annealed (CG) copper can be clearly observed (indicated by the red arrow), indicating that the grain boundaries were attacked predominantly while the grain interior is immune in the Livingston etchant. This is because the grain boundaries have higher energy than the grains and, therefore, work as an anode, while the grain

interior works as a cathode. With increasing SSE passes and higher dislocation density, the grain boundary grooves are not visible, and the surface became smoother, as shown in Figures 5(b)–5(e). When dislocation density becomes higher than  $10^{12} \text{ m}^{-2}$ , interspace between dislocations is lower than  $1 \mu\text{m}$  in average, with stress field by dislocations being overlapped. Thus, dislocation pits are not isolated rendering dissolution from selective to more uniform manner.

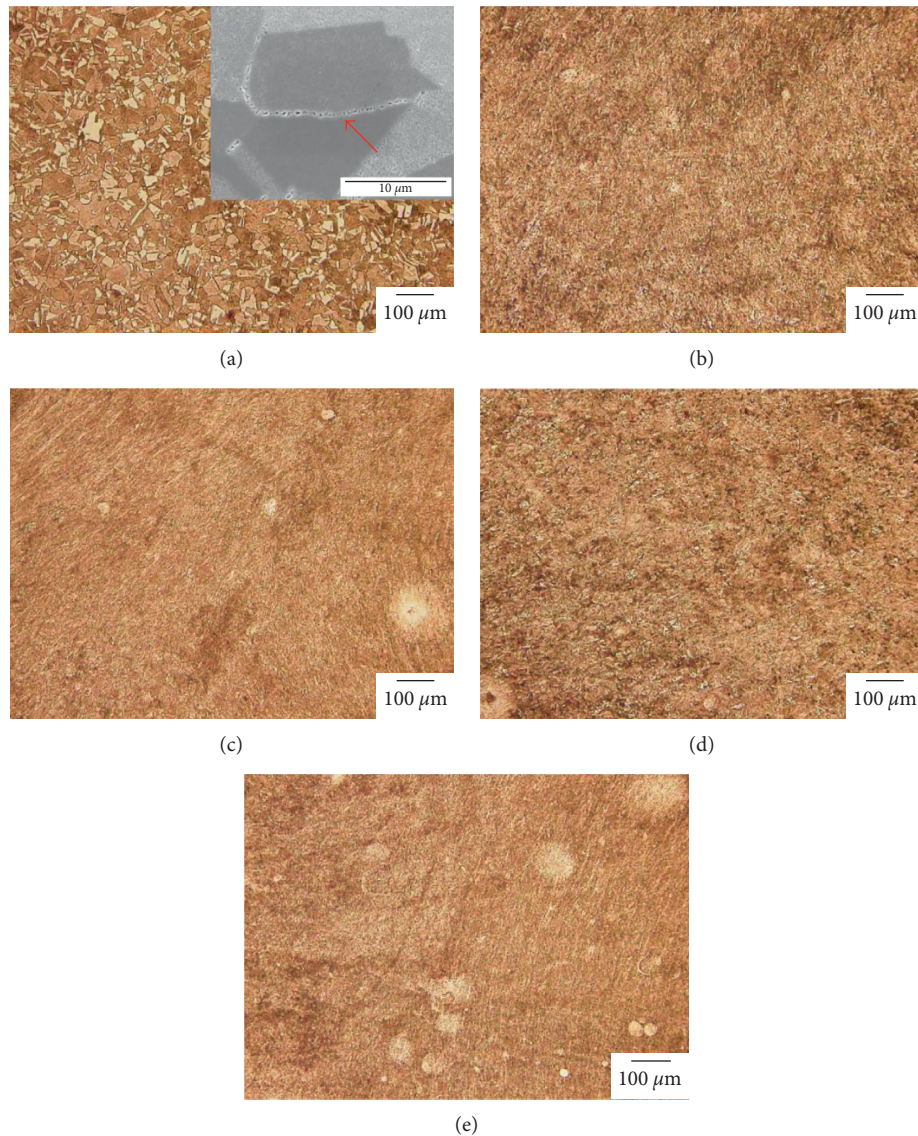


FIGURE 5: Dissolution surface morphology of samples: (a) as-annealed and (b) two, (c) four, (d) eight, and (e) twelve SSE passes.

The most important result in this study is that weight loss by dissolution reflects the line broadening by XRD, namely, weight loss decreases with higher strain after UFG formation. The decrease in the dislocation density after severe plastic deformation was also reported along with softening caused by the dislocation annihilation [15–21]; for example, after four passes of equal-channel angular pressing (ECAP) of pure copper, a decrease in the dislocation density was reported by Della Torre et al. [11]. According to their result, it is suggested that the decrease of stress field is also related to the operation of recovery mechanism, causing an increase in the dislocation-free grains [11]. The high extrinsic dislocation density at nonequilibrium grain boundaries may affect the dissolution rate because of lower activation energy for dissolution [4]. The dislocation annihilation inside grains as well as transition from nonequilibrium to equilibrium state therefore may cause the decreasing dissolution behavior after UFG formation in pure copper in the modified Livingston etchant.

#### 4. Conclusions

The effect of SSE passes on the dissolution was investigated by the modified Livingston etchant which is very sensitive to dislocations. Consequently, the following major conclusions can be drawn:

- (1) The internal strain field evaluated by X-ray line broadening measurements increased gradually until eight SSE passes and decreased until twelve SSE passes.
- (2) The weight loss obtained by the immersion tests in Livingston dislocation etchant increased with the increasing number of SSE passes until eight passes which formed UFG and then decreased after twelve SSE passes. It reflected the variation in the internal strain obtained by XRD.
- (3) The decrease in the dissolution rate may be related with the dynamic recovery, which decreases the

dislocation density inside grains and causes structural change of grain boundaries from non-equilibrium to equilibrium state.

## Conflicts of Interest

The authors declare that there are no conflicts of interest regarding the publication of this paper.

## References

- [1] R. Z. Valiev, R. K. Islamgaliev, and I. V. Alexandrov, "Bulk nanostructured materials from severe plastic deformation," *Progress in Materials Science*, vol. 45, no. 2, pp. 103–189, 2000.
- [2] N. Pardis and R. Ebrahimi, "Deformation behavior in simple shear extrusion (SSE) as a new severe plastic deformation technique," *Materials Science and Engineering: A*, vol. 527, no. 1-2, pp. 355–360, 2009.
- [3] E. Bagherpour, F. Qods, R. Ebrahimi, and H. Miyamoto, "Nanostructured pure copper fabricated by simple shear extrusion (SSE): a correlation between microstructure and tensile properties," *Materials Science and Engineering: A*, vol. 679, pp. 465–475, 2017.
- [4] H. Miyamoto, K. Harada, T. Mimaki, A. Vinogradov, and S. Hashimoto, "Corrosion of ultra-fine grained copper fabricated by equal-channel angular pressing," *Corrosion Science*, vol. 50, no. 5, pp. 1215–1220, 2008.
- [5] J. Xu, J. Li, D. Shan, and B. Guo, "Microstructural evolution and micro/meso-deformation behavior in pure copper processed by equal-channel angular pressing," *Materials Science and Engineering: A*, vol. 664, pp. 114–125, 2016.
- [6] F. W. Young Jr., "Etch pits at dislocations in copper," *Journal of Applied Physics*, vol. 32, no. 2, pp. 192–201, 1961.
- [7] A. Vinogradov, T. Mimaki, S. Hashimoto, and R. Valiev, "On the corrosion behaviour of ultra-fine grain copper," *Scripta Materialia*, vol. 41, no. 3, pp. 319–326, 1999.
- [8] E. Bagherpour, R. Ebrahimi, and F. Qods, "An analytical approach for simple shear extrusion process with a linear die profile," *Materials and Design*, vol. 83, pp. 368–376, 2015.
- [9] E. Bagherpour, F. Qods, and R. Ebrahimi, "Effect of geometric parameters on deformation behavior of simple shear extrusion," *IOP Conference Series: Materials Science and Engineering*, vol. 63, p. 012046, 2014.
- [10] K. Kapoor, D. Lahiri, S. V. R. Rao, T. Sanyal, and B. P. Kashyap, "X-ray diffraction line profile analysis for defect study in Zr-2.5% Nb material," *Bulletin of Materials Science*, vol. 27, no. 1, pp. 59–67, 2004.
- [11] F. H. Dalla Torre, R. Lapovok, J. Sandlin, P. F. Thomson, C. H. J. Davies, and E. V. Pereloma, "Microstructures and properties of copper processed by equal channel angular extrusion for 1–16 passes," *Acta Materialia*, vol. 52, no. 16, pp. 4819–4832, 2004.
- [12] V. Y. Gertsman, R. Birringer, R. Z. Valiev, and H. Gleiter, "On the structure and strength of ultrafine-grained copper produced by severe plastic deformation," *Scripta Metallurgica et Materialia*, vol. 30, no. 2, pp. 229–234, 1994.
- [13] R. K. Islamgaliev, F. Chmelik, and R. Kuzel, "Thermal stability of submicron grained copper and nickel," *Materials Science and Engineering: A*, vol. 237, no. 1, pp. 43–51, 1997.
- [14] A. A. Nazarov, "On the role of non-equilibrium grain-boundary structure in the yield and flow stress of polycrystals," *Philosophical Magazine A*, vol. 69, no. 2, pp. 327–340, 1994.
- [15] K. T. Aust, U. Erb, and G. Palumbo, "Interface control for resistance to intergranular cracking," *Materials Science and Engineering: A*, vol. 176, no. 1-2, pp. 329–334, 1994.
- [16] M. Yamashita, T. Mimaki, S. Hashimoto, and S. Miura, "Stress corrosion cracking of [110] and [100] tilt boundaries of  $\alpha$ -Cu-Al alloy," *Philosophical Magazine A*, vol. 63, no. 4, pp. 707–726, 1991.
- [17] W. Luo, Y. Xu, Q. Wang, P. Shi, and M. Yan, "Effect of grain size on corrosion of nanocrystalline copper in NaOH solution," *Corrosion Science*, vol. 52, no. 10, pp. 3509–3513, 2010.
- [18] C. P. Gräf, U. Heim, and G. Schwitzgebel, "Potentiometrical investigations of nanocrystalline copper," *Solid State Ionics*, vol. 131, no. 1-2, pp. 165–174, 2000.
- [19] M. Goerdeler and G. Gottstein, "A microstructural work hardening model based on three internal state variables," *Materials Science and Engineering: A*, vol. 309-310, pp. 377–381, 2001.
- [20] F. Roters, D. Raabe, and G. Gottstein, "Work hardening in heterogeneous alloys—a microstructural approach based on three internal state variables," *Acta Materialia*, vol. 48, no. 17, pp. 4181–4189, 2000.
- [21] F. H. Dalla Torre, A. A. Gazder, E. V. Pereloma, and C. H. Davies, "Recent progress on the study of the microstructure and mechanical properties of ECAE copper," *Journal of Materials Science*, vol. 42, no. 5, pp. 1622–1637, 2007.

## Research Article

# Effect of Partial Cladding Pattern of Aluminum 7075 T651 on Corrosion and Mechanical Properties

E. Rendell,<sup>1</sup> A. Hsiao,<sup>1,2</sup> and J. Shirokoff<sup>3</sup>

<sup>1</sup>Mechanical Engineering Department, Faculty of Engineering and Applied Science, Memorial University of Newfoundland, St. John's, NL, Canada A1B 3X5

<sup>2</sup>University of Prince Edward Island, Charlottetown, PEI, Canada C1A 4P3

<sup>3</sup>Process Engineering Department, Faculty of Engineering and Applied Science, Memorial University of Newfoundland, St. John's, NL, Canada A1B 3X5

Correspondence should be addressed to J. Shirokoff; shirokoff@mun.ca

Received 7 June 2017; Revised 15 July 2017; Accepted 26 July 2017; Published 27 August 2017

Academic Editor: Alicia E. Ares

Copyright © 2017 E. Rendell et al. This is an open access article distributed under the Creative Commons Attribution License, which permits unrestricted use, distribution, and reproduction in any medium, provided the original work is properly cited.

The corrosion resistance of aluminum 7075 T651 in full clad (Alclad), partial clad, and bare (unclad) forms was compared after 300 hours of corrosion exposure in an acidic salt spray cabinet test at 36°C. After corrosion exposure, severe to moderate exfoliation corrosion was observed on the unprotected medium sized test panel, light general corrosion was observed on the partially clad panel, and patches of corrosion not penetrating the clad layer were observed on the fully clad panel. After corrosion tests, the tensile strength of partially clad, fully clad, and unprotected panels decreased by 3.4%, 4.0%, and 5.3%, respectively.

## 1. Introduction

One of the primary drivers for materials selection in the aerospace industry is to maximize the economic efficiency of aircraft [1]. Commercial aircraft of the past utilized the high specific strength of the high strength aluminum alloys of the 2000 and 7000 series almost exclusively for the construction of structural components [2]. These materials were selected in an effort to minimize aircraft weight resulting in maximized aircraft payloads and reduce fuel consumption. High strength aluminum alloys are susceptible to localized corrosion such as pitting, exfoliation, and stress corrosion cracking. Presently, corrosion resistance of materials is also of great concern because of the cost of corrosion inspections and the high cost of unscheduled maintenance and aircraft downtime associated with replacing corroded aircraft components [3]. Corrosion as well as the ability to construct larger structural components that are more easily joined has resulted in a shift in preferred construction materials from high strength aluminum alloys to composites for new aircraft [1]. In spite of this, aluminum alloys will remain an important structural material for aircraft components, especially in

compression where composites are less suitable. This shift in materials selection has caused the need for aluminum alloy innovation to maximize specific strength while maintaining acceptable corrosion resistance for aluminum to remain a competitive material choice [2]. The susceptibility of high strength aluminum alloys to corrosion requires them to be protected from corrosive environment using an anodic coating for components with complex geometries or by using Alclad products with an aerospace coating system on sheet and plate components. Alclad products are produced by the metallurgical bonding of a high strength aluminum alloy core sandwiched between two layers of a more electronegative aluminum alloy. The outer aluminum cladding layers corrode preferentially when exposed to a corrosive environment and prevent corrosion to the core by cathodic protection. The Alclad layers can comprise up to 4% of the total sheet or plate thickness [4] and are assumed to carry no load, reducing the overall material specific strength by increasing the weight without contributing to the strength.

Petroyiannis et al. have suggested in previous works that a continuous cladding layer may be excessive and that the application of a partial cladding pattern may provide

equivalent corrosion protection for aluminum 2024 T3 alloys [5, 6]. They have found that a partial cladding layer covering only 7% of the core aluminum substrate provides equivalent corrosion protection to the mechanical properties of Al 2024 T3 when compared to Alclad products after a 300-hour immersion exposure in a neutral 3.5% NaCl solution. However, they have also concluded that this accelerated corrosion test is likely too mild to accurately represent the corrosion environment experienced by in service aircraft [6].

In this work, an appropriate partial cladding geometry for Al 7075 T651 is estimated by exposing an aluminum panel with a single clad spot to an acidic salt fog accelerated corrosion environment. The area of the panel protected from corrosion by the clad spot is then estimated and used to determine dimensions for a two-dimensional array of clad spots applied to a medium scale test panel. For comparison, medium scale test panels in both the as-received Alclad state and having the entire cladding layer removed have also been produced. These three test panels were exposed to the acidic salt fog accelerated corrosion environment and the resulting corrosion was compared through visually rating and by producing characteristic cross sections. Tensile specimens were then machined from the three corroded panels as well as tensile specimens having undergone the same machining processes as the three panels unexposed to the corrosion environment. All of the tensile specimens were then tested and compared.

## 2. Experimental

**2.1. Corrosion Environment.** The corrosion environment selected for all of the experiments presented in this work was a 300-hour continuous acidic salt fog cabinet test in accordance with ASTM G85 Annex A1 [7]. The tests were conducted in a 120-liter benchtop Ascott S120ip salt spray chamber maintained at 36°C. The solution used to produce the acidic salt fog was composed of deionized water prepared with a Purite DC9 deionizing cylinder. The pH was then adjusted to a value between 3.1 and 3.3 by the addition of 99.7+% ACS reagent grade acetic acid purchased from Alfa Aesar. A solution salt concentration of 4–6 weight percent sodium chloride was produced by the addition of “Corro-Salt” purchased from Ascott. “Corro-Salt” meets the strict salt purity requirements detailed in ASTM B117 [8], namely, total impurities less than 0.3%, total halide (excluding chloride) composition of less than 0.1%, and a copper content of less than 0.3 ppm. The fog fallout rate was set between 1.0 and 2.0 mL per hour per 80 cm<sup>2</sup> horizontal area.

**2.2. Single Central Clad Spot Panel.** Initially a single clad spot test panel was produced from 6.35 mm thick Alclad Al 7075 T651 plate having a total area exposed to the corrosion environment of 10 × 10 cm<sup>2</sup> with a square 1 cm<sup>2</sup> clad spot located in the panel center. The panel surface geometry was produced by mechanically milling approximately 0.19 mm over the panel surface removing the Alclad layer except at the clad spot. The cut edges and back surface of the test panel were protected from the corrosion environment with corrosion resistant polyvinyl chloride tape with the seams

sealed with super glue gel. After corrosion exposure, the panel was cleaned in accordance with ASTM G1 [9]. The panel was cleaned with water and stiff brush to remove deposited salt and some of the bulk corrosion products. This was followed by a four-minute immersion in nitric acid at room temperature to remove the remainder of the corrosion products. The exfoliation damage to the panel was characterized by applying a 2.5 × 2.5 mm grid to the surface and estimating the percentage of the panel surface affected by corrosion in each grid section. This data was then used to produce a surface plot showing the distribution of corrosion damage relative to the protective clad spot. To characterize the penetration of the corrosion damage, the machining method for determining pit depth described in ASTM G46 [10] was adapted to better describe exfoliation penetration. Approximately 0.02 mm and 0.17 mm were milled from the corroded panel surface and surface plots were produced characterizing the extent of exfoliation corrosion penetrating to these depths. The surface plots of the initial single clad spot test panel were used to estimate the area of the test panel effectively protected by the clad spot and used to determine appropriate dimensions for a partial cladding pattern to be applied to a medium scale test panel.

**2.3. Medium Scale Test Panels.** A series of medium scale test panels were produced again from 6.35 mm thick Alclad Al 7075 T651 plate to investigate if a partial cladding pattern provides equivalent corrosion resistance when compared to Alclad in the selected corrosion environment. The medium scale test panels had a surface exposed to the corrosion environment of approximately 30 × 25 cm. The back surface and cut edges of the panels were protected for the corrosion environment using the same method described above for the initial single clad spot panel. Three medium scale test panels were produced to compare the relative corrosion resistance of fully clad aluminum plate, aluminum plate with a partial cladding pattern, and aluminum plate with no cladding. The fully clad test panel remains in the as-received Alclad form. The partially clad test panel was produced by mechanically milling the Alclad layer over the majority of the panel surface producing 1 × 1 cm clad spots. The clad spots were arranged in a two-dimensional array spaced 2 cm apart. During the machining process of the partially clad test panel, it was desired that only the Alclad layer be removed by milling approximately 0.19 mm from the panel surface to produce the clad spots. Due to difficulties in the machining process, such as the panel not being perfectly flat and issues with affixing the aluminum panel to the CNC milling machine, an average thickness of 0.69 mm was removed from the panel thickness to produce the clad spots. This resulted in the clad spots being comprised of both the cladding layer and a significant thickness of the high strength aluminum 7075 core. The presence of the layer of Al 7075 within the clad spots is not expected to significantly affect the corrosion behavior of the partially clad panel but may influence the mechanical testing results. The test panel with no cladding was produced by removing the entire Alclad layer through mechanical milling.

The experimental approach is highlighted in Figure 1 indicating schematic cross sections of the three medium sized

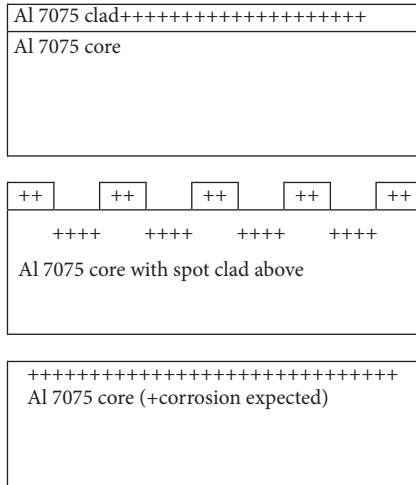


FIGURE 1: Schematic cross sections of the three medium sized test panels indicating the location (+) of corrosion products expected after corrosion testing. All test panels have visual exposed areas of 30 × 25 cm to salt spray. Alclad means full clad, while spot clad (partial clad) and unclad were machined to remove part or all of the clad layer.

test panels with a plus symbol (+) to indicate the expected development of corrosion products starting at the surface. All test panels have visual exposed surface areas of 30 × 25 cm to salt spray corresponding to Figure 1. Alclad means full clad, while spot clad (partial clad) and unclad were machined to remove part or all of the clad layer.

After exposure to the corrosion environment, the medium scale test panels were cleaned in the same method as the initial single clad spot test panel described above. The corrosion damage resulting from exposure to the acidic salt fog environment on the medium scale panels was qualitatively compared through visual observations and through cutting representative cross sections from each of the test panels. The cross sections were cut from various locations on the medium scale test panels with an Isomet 11-1180 low speed saw and then mounted and polished in SamplKwick fast dry acrylic. The cross sections were viewed at 100x magnification with a Nikon Eclipse 50i optical microscope and images were captured with an Infinity 1 microscopy camera.

Rectangular tensile specimens were cut from each of the corroded medium scale test panels in accordance with ASTM B557 [11]. For comparison, tensile specimens were prepared from uncorroded Al 7075 T651 that has undergone the same milling processes as the medium scale test panels, two tensile specimens for each of the panel surface geometries. All of the tensile samples were tested in accordance with ASTM B557 with an Instron 5585H load frame using wedge type grips. The crosshead speed of all the tensile tests was 5 mm/minute and the strain during the elastic section of the tests was measured using an Instron 2630-106 clip on extensometer with a gauge length of 25 mm.

Materials characterization by scanning electron microscopy-energy dispersive spectroscopy (SEM-EDS) was



FIGURE 2: Optical microscopy of a cleaned central clad spot panel, 1 square cm clad spot.

performed using a JEOL-JSM-6000 operating at 15 kV in order to verify the Alclad 7075 cladding, core, and corrosion product elemental analysis (i.e., red corrosion product containing 7.71 mass% Cu). The SEM-EDS results verified the alloying elements of the Alclad layers (cladding, core) as specified by the North American supplier of Alclad in their Al 7075 technical specification, expected reactions, and corrosion products. The Al-alloy clad layer reacts to form  $Al_2O_3$  with Al dissolution; and Al-alloy core reacts to form Al-Cu corrosion product via the elemental Cu level increase from 1.50 to 7.71 mass% to be discussed further in the results and discussion sections. The  $Al_2O_3$  was confirmed by X-ray diffraction using a Rigaku Ultima IV operating with Cu K-alpha radiation at 40 kV and 44 mA. Image analysis was also employed using a PAX system in order to estimate the percentage of surface area that corroded.

### 3. Results

**3.1. Single Central Clad Spot Panel.** After exposure to the acidic salt fog corrosion environment and cleaning, it can be seen in Figure 2 that there are two regions of interest on the central clad spot panel. A roughly circular region adjacent to the clad spot has been protected from the corrosion environment due to the clad spot acting as a sacrificial anode. The remainder of the panel shows corrosion that could be described as moderate exfoliation [12] or as poorly defined pitting with a large degree of horizontal propagation and delamination [9].

The optical image analysis system application of a grid on the corroded surface was used for an estimation of the percentage of the area of each grid section showing signs of corrosion on the three panels (central clad spot, 0.02 mm and 0.17 mm milled). From these surface plots, the area of the central clad spot test panel effectively protected by the clad spot was estimated as a 3 × 3 cm square. This dimension was used to produce the medium sized test panel with a clad spot pattern. It was estimated that a two-dimensional array of

1 cm<sup>2</sup> clad spots spaced 2 cm apart is sufficient to protect the panel surface from corrosion after a 300-hour exposure in the acidic salt fog environment.

### 3.2. Medium Scale Test Panels

**3.2.1. Initial Visual Observations of the Medium Scale Test Panels.** Upon visual inspection of the Alclad medium scale test panel, shallow irregularly shaped corrosion patches are fairly evenly distributed over the panel surface. Smaller, pit-like corrosion is also evident in the cladding layer. It appears that pitting has initiated in the cladding layer and progressed until reaching the aluminum core where the pits widened laterally, combining to form larger corrosion spots. From these observations it appears that the Alclad layer has successfully protected the high strength aluminum core by corroding preferentially in the acidic salt spray environment.

After corrosion exposure, exfoliation corrosion was observed over the entire surface of the panel with the cladding removed. Using the exfoliation corrosion rating system described in ASTM G34, the observed corrosion could be described between pitting and moderate exfoliation. Distinct pit-blisters were observed but with more lifting of the aluminum along the pit edges than is described in the standard. The blistering and lifting of slivers of uncorroded aluminum at the pit edges more closely resembled moderate exfoliation but there is less layering than described in the standard. Overall the observed corrosion can best be described as pit-blisters that have exposed grain boundaries allowing intergranular corrosion in the form of exfoliation to occur in tandem. Where multiple pit-blisters interacted to lift continuous sheets of uncorroded aluminum, the corrosion began to resemble moderate exfoliation. An unexpected observation is the “red colored” corrosion products presumably due to copper since the elemental Cu level increase from 1.50 to 7.71 mass% as measured by energy dispersive spectroscopy over the majority of the panel surface.

The corrosion observed over the partially clad medium scale test panel after acidic salt spray exposure was not uniform. Five distinct regions of corrosion behavior were observed: (1) The surface of the clad spots experienced general corrosion, where the Alclad layer was depleted as a sacrificial anode, protecting the overall panel surface. (2) The majority of the panel surface was successfully protected by the partial cladding pattern. This is evident where the surface retained the shiny appearance and milling marks from the machining process. (3) General corrosion with red color resembled what was observed on the unprotected test panel. (4) Light general corrosion located between the red colored region and the shiny noncorroded region. (5) Finally, there are small patches of corrosion distributed throughout the noncorroded region of the panel. These patches are generally located adjacent and below the clad spots. These patches of corrosion can possibly be explained by the acidic salt solution stagnating in the raised edges of the clad spots or within milling marks and leading to crevice corrosion.

**3.2.2. Representative Cross Sections of the Medium Scale Test Panels.** Many cross sections cut from the medium scale test

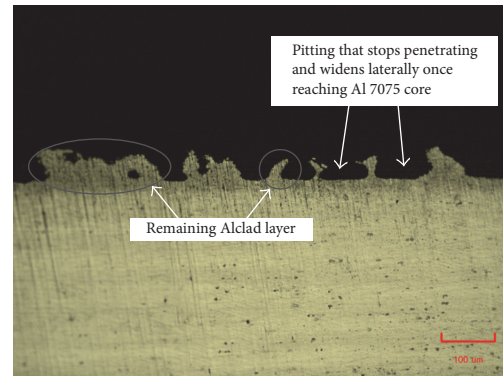


FIGURE 3: Clad panel and region after corrosion, 100x magnification and 100-micron bar.

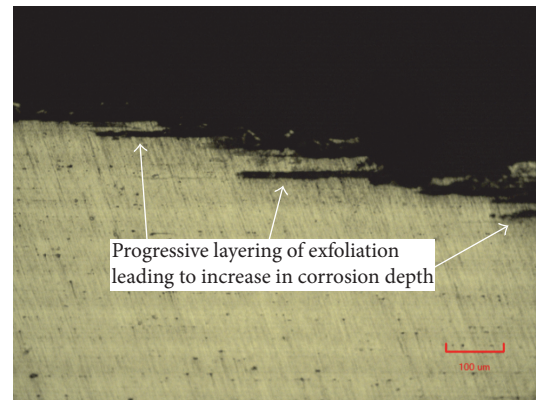


FIGURE 4: Unclad panel deep exfoliation damage, 100x magnification and 10-micron bar.

panels largely confirm the initial visual observations made of the corroded panels. Figure 3 shows one of the large corrosion patches distributed over the Alclad test panel surface. Dense pitting penetrating the Alclad layer until reaching the high strength aluminum core and widening laterally, combining to form larger shallow pits, is evident. Alclad that was representative of the majority of the test panel exhibited a smooth surface and intact cladding layer, indicating that these regions were unaffected by the corrosion environment.

Figures 4 and 5 are cross sections representing the corrosion observed on the bare test panel. Figure 4 shows successive layers of exfoliation resulting in increasing corrosion penetration depth after corrosion product expansion. As slivers of uncorroded aluminum are lifted from the substrate, additional grain boundaries are exposed to the corrosion environment and a new layer of exfoliation corrosion is initiated. Figure 5 shows one of the few examples of a well-defined pit in the unclad test panel. The absence of many examples of pitting can be explained by the large number of grain boundaries exposed by the pit. The pit initiates intergranular corrosion that progresses into exfoliation and obliterates evidence of the pit [13, 14].

TABLE 1: Mechanical properties summary.

Property/material	Mechanical property and change ( $\Delta$ ) due to corrosion					
	No cladding		Spot cladding		Full clad	
	Corrosion	No corrosion	Corrosion	No corrosion	Corrosion	No corrosion
Tensile strength (MPa)	550 $\Delta$ -5.3%	581	561 $\Delta$ -3.4%	581	551 $\Delta$ -4.0%	574
Yield strength (MPa)	520 $\Delta$ 2.2%	509	528 $\Delta$ 3.9%	508	520 $\Delta$ 3.4%	503
Young's modulus (GPa)	66.5 $\Delta$ -7.4%	71.8	70.5 $\Delta$ 1.0%	69.8	69.1 $\Delta$ 3.6%	66.7
Elongation (%)	13.7 $\Delta$ -18.4%	16.2	13.5 $\Delta$ -8.7%	14.8	17.3 $\Delta$ -4.2%	18.1

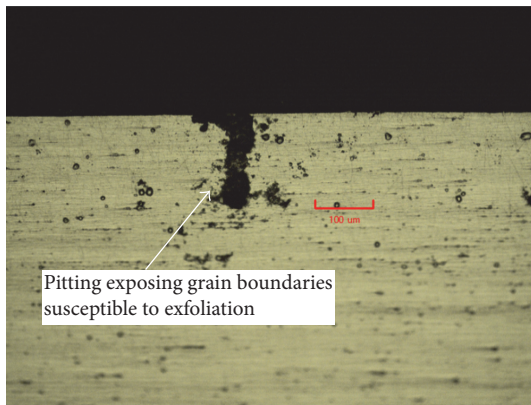


FIGURE 5: Unclad panel and evidence of pitting, 100x magnification and 100-micron bar.

3.3. *Mechanical Properties.* Table 1 shows the mechanical properties summary of the tensile specimens cut from the corroded medium scale test panels and the tensile specimens that have undergone the same mechanical processes but have not been exposed to the corrosion environment. When comparing the corroded and the uncorroded tensile specimens, there is a decrease in tensile strength in each case. The partially clad test panel exhibits the smallest decrease in tensile strength with a percent decrease of 3.4%. This was followed by the fully clad test panel with a tensile strength percentage decrease of 4.0%. Finally, the cladding removed panel showed a percentage decrease in tensile strength of 5.3%.

In all cases, the yield strength of the tensile specimens increased after corrosion exposure. The spot clad, fully clad, and cladding removed test specimens showed a percent increase in yield strength of 3.9%, 3.4%, and 2.2%, respectively. This trend is interesting, as it is expected that the yield strength would decrease with corrosion exposure.

Young's modulus of the spot clad and fully clad test panels increased after corrosion exposure while there was a decrease for the bare test panel. The percent increase in Young's modulus for the spot clad and fully clad test panels was 1.0% and 3.6%, respectively. The percentage decrease in Young's modulus for the unprotected panel was 7.4%.

In all cases, there was a decrease in percent elongation after corrosion exposure. The percent decrease in percent elongation for the cladding removed, spot clad, and fully clad test specimens was 18.4%, 8.7%, and 4.2%, respectively.

#### 4. Discussion

The single central clad spot panel was used to evaluate the region of corrosion surrounding the surface containing a  $1 \times 1$  cm spot clad. Optical image analysis tools can provide an estimate of corroded surface area and from this approach the spot clad spacing of 2 cm was determined to be sufficient for adequate corrosion protection. For more quantitative analysis additional work would be required and it should therefore be considered by characterization methodologies such as scanning electron microscopy with energy dispersive spectroscopy capable of X-ray mapping chemical elements and also comparison of one spot to perhaps an array of four spots. From the visual observations and representative cross sections of the medium scale test panels, it is apparent that the cladding layer of the Alclad test panel successfully protected the high strength aluminum core from the corrosion environment. Conversely, the absence of the cladding layer was detrimental to the corrosion resistance of the bare test panel. Uniform exfoliation corrosion was observed over the entire panel surface after corrosion exposure. The corrosion to the high strength aluminum core observed on the partially clad test panel remained mild when compared to the bare panel but was somewhat more severe than the Alclad panel.

From the visual observations and representative cross sections of the medium scale test panels, it is apparent that the cladding layer of the Alclad test panel successfully protected the high strength aluminum core from the corrosion environment. Conversely, the absence of the cladding layer was detrimental to the corrosion resistance of the bare test panel. Uniform exfoliation corrosion was observed over the entire panel surface after corrosion exposure. The corrosion to the high strength aluminum core observed on the partially clad test panel remained mild when compared to the bare panel but was somewhat more severe than the Alclad panel.

An unexpected result was the red coloring of corrosion products on the bare test panel. It is believed that the red colored corrosion products are the result of alloyed copper

dissolving into the corrosive electrolyte and plating back onto the aluminum alloy substrate.

During the corrosion of aluminum alloys containing copper as a major alloying element, in the presence of chloride ions, copper containing intermetallic particles found in Al 7075 T651 such as  $MgCu_2$  or  $Al_2CuMg$  can be subjected to dealloying where magnesium and aluminum are selectively dissolved, leaving behind a microporous region consisting primarily of elemental copper. These high surface area regions of copper can then act as a local cathode and cause pitting and trenching to the alloy adjacent to the copper. It is then possible for the copper region to detach from the aluminum alloy, dissolve into the corrosive electrolyte, and electrically be plated back onto the alloy surface [15, 16]. The presence of the plated copper could then cause galvanic corrosion, accelerating the overall corrosion rate of the bare test panel.

The red corrosion products believed to be copper were also present on the partially clad test panel. The location of the red corrosion products on the top edge of the panel surface where there are not yet any clad spots may suggest that the ability of the clad spots to protect the aluminum substrate from corrosion exposure may be influenced by the downward flow of the corrosive electrolyte as the acidic salt fog is deposited on the surface. If the red coloring is plated copper, as is believed, the area of light general corrosion on the partially clad panel may be explained by galvanic corrosion caused by the copper accelerating the corrosion rate in this area.

From the results of the tensile testing of the medium scale test panels, the tensile strength and percent elongation show the most conclusive results. The results for the yield strength and Young's modulus remain fairly ambiguous, possibly because the aluminum plate selected for the experiment was rather thick (6.35 mm) and it is possible that the corrosion damage on all three test panels was superficial when compared to the plate thickness.

From the tensile strength results, the partially clad test panel had the smallest reduction in tensile strength after corrosion exposure with a percent decrease of 3.4% while the Alclad and bare panels had percent decreases of 4.0% and 5.3%, respectively. This suggests that the partial cladding pattern successfully protected the test panel from the corrosion environment when compared to the Alclad and bare panels. The fact that the tensile strength of the bare test panel was not more severely affected by the corrosion environment may suggest that the selected corrosion environment was too mild for the corrosion damage to significantly affect the tensile strength for 6.35 mm aluminum plate.

The results for the degradation in percent elongation of the test panels in this experiment suggest that the ductility of the aluminum was significantly affected by both the machining processes conducted on the aluminum plate and the corrosion environment exposure. The percent decrease in percent elongation for the bare, spot clad, and fully clad test specimens after corrosion exposure was 18.4%, 8.7%, and 4.2%, respectively. In this instance, the Alclad test panel outperformed the partially clad test panel but the partially clad panel performed much better than the bare panel. The percent elongation of the uncorroded spot clad, bare, and

Alclad test panels was 14.8%, 16.2%, and 18.1%, respectively. These values differ significantly and imply that the machining processes subjected to each of the test panels had an effect on ductility. It is possible that the milling of the surface of the bare panel had a work hardening effect that reduced overall panel ductility. For the partially clad test panel, it is believed that the presence of the clad spots comprising not only the soft Alclad layer but also a thickness of the high strength aluminum core reduced overall ductility by reinforcing the sections of the test specimens with clad spots. As a result, the majority of the deformation of the tensile specimens occurred only in locations without the clad spot and the specimens fractured with an overall lower percent elongation.

When correlating mechanical properties results to corrosion test data and microstructure the issue of uncertainties deserves some discussion. Since these mechanical properties results are presented after several times of testing it is important to include the following caveat (i.e., the results fall within the uncertainties of experimentation that includes sample homogeneity, aging, microstructure, machining, anisotropy, residual stress, equipment calibration, grip forces, and work hardening); otherwise conclusions can be misinterpreted, misused, and misleading.

Therefore additional research study inclusive of detailed uncertainties analysis is recommended in order to verify the general trends in results that only approximate spot clad and fully clad mechanical properties. In general, the overall performance of full clad (Alclad) to corrosion should favor the clad versions (full clad = Alclad, partial clad) over unclad because aircraft alloys in service are normally held to a high level of standard in terms of performance, risk, and safety.

## 5. Conclusions

- (1) The spot clad spacing of 2 cm was determined to be sufficient for adequate corrosion protection.
- (2) After corrosion tests, the tensile strength of the partially clad, fully clad (Alclad), and unprotected test panels decreased by 3.4%, 4.0%, and 5.3%, respectively.

## Conflicts of Interest

The authors declare that they have no conflicts of interest.

## Authors' Contributions

The authors involved are the graduate student Evan Rendell who performed the original research and master's thesis under supervision of Dr. Amy Hsiao and Dr. John Shirokoff the latter of whom created the paper from the thesis and performed some additional research and writing to clarify and validate specific results.

## Acknowledgments

The research in this paper is supported by an industrial regional benefit program of the Government of Newfoundland at Memorial University of Newfoundland.

## References

- [1] E. A. Starke Jr. and J. T. Staley, "Application of modern aluminum alloys to aircraft," *Progress in Aerospace Sciences*, vol. 32, no. 2-3, pp. 131–172, 1996.
- [2] A. Merati, "Materials replacement for aging aircraft," in *Corrosion Fatigue and Environmentally Assisted Cracking in Aging Military Vehicles*, NATO Science and Technology Organization, 2011.
- [3] W. Tsai, "The economics of maintenance," in *The Standard Handbook for Aeronautical and Astronautical Engineers*, McGraw-Hill, New York, NY, USA, 2003.
- [4] ALCOA Mill Products Inc., Alloy 7075 sheet and plate, 2001.
- [5] P. V. Petroyiannis, S. G. Pantelakis, and G. N. Haidemenopoulos, "Protective role of local Al cladding against corrosion damage and hydrogen embrittlement of 2024 aluminum alloy specimens," *Theoretical and Applied Fracture Mechanics*, vol. 44, no. 1, pp. 70–81, 2005.
- [6] S. G. Pantelakis, A. N. Chamos, and D. Setsika, "Tolerable corrosion damage on aircraft aluminum structures: Local cladding patterns," *Theoretical and Applied Fracture Mechanics*, vol. 58, no. 1, pp. 55–64, 2012.
- [7] "Standard Practice for Modified Salt Spray (Fog) Testing," *ASTM*, no. G85-11, 2011.
- [8] "Standard Practice for Operating Salt Spray (Fog) Apparatus," *ASTM* B117-11, 2011.
- [9] "Standard Practice for Preparing, Cleaning and Evaluating Corrosion Test Specimens," *ASTM* G1-03(2011), 2011.
- [10] "Standard Guide for Examination and Evaluation of Pitting Corrosion," *ASTM*, no. G46-94(2013), 2013.
- [11] "Standard Test Methods for Tension Testing Wrought and Cast Aluminum-and Magnesium-Alloy Products," *ASTM* B557-14, 2014.
- [12] "Standard Test Method for Exfoliation Corrosion Susceptibility 2XXX and 7XXX Series Aluminum Alloys (EXCO Test)," *ASTM* G34-01(2013), 2013.
- [13] X. Zhao, *Exfoliation corrosion kinetics of high strength aluminum alloys [Ph.D. thesis]*, The Ohio State University, 2006.
- [14] D. W. Hoepfner and C. A. Arriscorreta, "Exfoliation corrosion and pitting corrosion and their role in fatigue predictive modeling: State-of-the-art review," *International Journal of Aerospace Engineering*, Article ID 191879, 2012.
- [15] M. B. Vukmirovic, N. Dimitrov, and K. Sieradski, "Dealloying and corrosion of Al alloy 2024-T3," *Journal of the Electrochemical Society*, vol. 149, no. 9, pp. B428–B439, 2002.
- [16] H. M. Obispo, L. E. Murr, R. M. Arrowood, and E. A. Trillo, "Copper deposition during the corrosion of aluminum alloy 2024 in sodium chloride solutions," *Journal of Materials Science*, vol. 35, no. 14, pp. 3479–3495, 2000.